Spatiotemporal transcriptomic atlas of mouse organogenesis using DNA nanoball patterned arrays

Ao Chen[1,2,25], Sha Liao[1,25], Mengnan Cheng[1,3,25], Kailong Ma[1,25], Liang Wu[1,3,4,25], Yiwei Lai[1,5,6,25], Xiaojie Qiu[7,8,25], Jin Yang[9], Wenjiao Li[1], Jiangshan Xu[1,3], Shijie Hao[1,3], Xin Wang[1], Huifang Lu[1], Xi Chen[1], Xing Liu[1], Xin Huang[1,3], Feng Lin[1], Zhao Li[1], Yan Hong[1], Defeng Fu[1], Yujia Jiang[1,10], Jian Peng[1], Shuai Liu[1], Mengzhe Shen[1], Chuanyu Liu[1,11], Quanshui Li[1], Yue Yuan[1,3], Huiwen Zheng[1,10], Zhifeng Wang[1,4], Zhaohui Wang[1], Xin Huang[1], Haitao Xiang[1,3], Lei Han[1], Baoming Qin[5,6], Pengcheng Guo[5,6], Pura Muñoz-Cánoves[12,13], Jean Paul Thiery[14], Qingfeng Wu[16], Fuxiang Zhao[1], Mei Li[1], Haoyan Kuang[1], Junhou Hui[1], Ou Wang[1], Haorong Lu[15], Bo Wang[15], Shiping Liu[1,4], Ming Ni[9], Wenwei Zhang[1,17], Feng Mu[9], Ye Yin[1,18], Huanming Yang[1,19], Michael Lisby[2], Richard J. Cornall[20], Jan Mulder[21,22], Mathias Uhlen[21,22], Miguel A. Esteban[1,5,6,23,*], Yuxiang Li[1,*], Longqi Liu[1,9,*], Xun Xu[1,24,26,*], Jian Wang[1,19,*]

[1]BGI-Shenzhen, Shenzhen 518103, China.

[2]Department of Biology, University of Copenhagen, Copenhagen DK-2200, Denmark.

[3]College of Life Sciences, University of Chinese Academy of Sciences, Beijing 100049, China.

[4]Shenzhen Key Laboratory of Single-Cell Omics, BGI-Shenzhen, Shenzhen 518120, China.

[5]Laboratory of Integrative Biology, Guangzhou Institutes of Biomedicine and Health, Chinese Academy of Sciences, Guangzhou 510530, China.

[6]CAS Key Laboratory of Regenerative Biology and Guangdong Provincial Key Laboratory of Stem Cells and Regenerative Medicine, Guangzhou Institutes of Biomedicine and Health, Guangzhou 510530, China.

[7]Whitehead Institute for Biomedical Research Cambridge, MA 02142, USA.

[8]Howard Hughes Medical Institute, Massachusetts Institute of Technology, Cambridge, MA 02139, USA.

[9]MGI, BGI-Shenzhen, Shenzhen 518083, China.

[10]BGI College & Henan Institute of Medical and Pharmaceutical Sciences, Zhengzhou University, Zhengzhou 450000, China.
[11]Shenzhen Bay Laboratory, Shenzhen 518000, China.
[12]Department of Experimental and Health Sciences, Pompeu Fabra University (UPF), ICREA and CIBERNED, Barcelona E-08003, Spain.
[13]Spanish National Center on Cardiovascular Research (CNIC), Madrid E-28029, Spain.
[14]Bioland Laboratory (Guangzhou Regenerative Medicine and Health Guangdong Laboratory), Guangzhou 510005, China.
[15]China National GeneBank, BGI-Shenzhen, Shenzhen 518120, China.
[16]State Key Laboratory of Molecular Development Biology, Institute of Genetics and Developmental Biology, Chinese Academy of Sciences, Beijing 100101, China.
[17]Shenzhen Key Laboratory of Neurogenomics, BGI-Shenzhen, Shenzhen 518103, China.
[18]BGI Genomics, BGI-Shenzhen, Shenzhen 518083, China.
[19]James D. Watson Institute of Genome Sciences, Hangzhou 310058, China.
[20]Medical Research Council Human Immunology Unit, Nuffield Department of Medicine, University of Oxford, Oxford OX3 7BN, United Kingdom.
[21]Department of Protein Science, Science for Life Laboratory, KTH-Royal Institute of Technology, Stockholm 17121, Sweden.
[22]Department of Neuroscience, Karolinska Institute, Stockholm 17177, Sweden.
[23]Institute of Stem Cells and Regeneration, Chinese Academy of Sciences, Beijing 100101, China.
[24]Guangdong Provincial Key Laboratory of Genome Read and Write, Shenzhen 518120, China.
[25]These authors contributed equally to this work.
[26]Lead contact.
*Correspondence: wangjian@genomics.cn (J.W.), xuxun@genomics.cn (X.X.), liulongqi@genomics.cn (L.L.), liyuxiang@genomics.cn (Y.L.), miguelesteban@genomics.cn (M.A.E.).

SUMMARY

Spatially resolved transcriptomic technologies are promising tools to study cell fate decisions in a physical microenvironment, which is fundamental for enhancing our knowledge of mammalian development. However, the imbalance between resolution, transcript capture and field of view of current methodologies precludes their systematic application to analyze relatively large and three-dimensional mid- and late-gestation mammalian embryos. Here, we combined DNA nanoball (DNB) patterned arrays and tissue RNA capture to create SpaTial Enhanced REsolution Omics-sequencing (Stereo-seq). This approach allows transcriptomic profiling of large histological sections with high resolution and sensitivity. We have applied Stereo-seq to study the kinetics and directionality of transcriptional variation in a time course of mouse organogenesis. We used this information to gain insight into the molecular basis of regional specification, neuronal migration and differentiation in the developing brain. Furthermore, we mapped the expression of a panel of developmental disease-related loci on our global transcriptomic maps to define the spatiotemporal windows of tissue vulnerability. Our panoramic atlas constitutes an essential resource to investigate longstanding questions concerning normal and abnormal mammalian development.

INTRODUCTION

Understanding how a single totipotent cell, the zygote, develops into a complex organism such as a mammal in a precisely controlled manner, over time and space, is one of the most fascinating questions in science ever since Aristotle. Mouse is an excellent model mammal to study developmental processes and establish parallels with larger species thanks to the inbred genetic background, susceptibility to genetic manipulation and relatively short gestation period (~21 days). Recent intense efforts on cell atlas using high-throughput single-cell RNA-sequencing (scRNA-seq) technologies have provided an increasingly detailed view of mouse developmental gene expression dynamics (Cao et al., 2019; He et al., 2020). However, except for the early embryonic time points where fewer cells are present (Peng et al., 2019; Xue et al., 2013), topographical transcriptomic information is still mostly lacking. This deficiency complicates the interpretations, in particular the correlation between signaling cues and cell fate decisions. In this regard, embryonic decisions are often regulated by gene expression thresholds rather than binary mechanisms. The outstanding need for precise coordination of complex signals and the myriad embryonic cell types in development is exemplified by genetic disorders like situs inversus, where alterations in the response to nodal flow cause inversion of the internal anatomy (Okada et al., 2005). Systematic spatially resolved analysis of gene expression is thus strictly necessary to dissect the intricacies of mammalian development.

Several remarkable methodologies have been recently developed that allow spatially resolved transcriptomic profiling of tissue sections. They can be divided in three main classes based on their detection method: physical segmentation using microdissection coupled to sequencing (Nichterwitz et al., 2016; Peng et al., 2019), pre-designed probes for either single-molecule hybridization (Eng et al., 2019; Zhuang, 2021) or amplification and *in situ* decoding (Alon et al., 2021; Lee et al., 2014; Wang et al., 2018), and barcoded probes (Cho et al., 2021a; Rodriques et al., 2019; Srivatsan et al., 2021; Stahl et al., 2016; Vickovic et al., 2019; Yao et al., 2020). These techniques all have specific advantages and disadvantages in resolution and applicability but share a major caveat in the limited field of view. Although

small parts of developing mouse tissues (Di Bella et al., 2021; Stickels et al., 2021) or even whole mouse embryos (Peng et al., 2019; Srivatsan et al., 2021; Yao et al., 2020) have been analyzed using these approaches, no available technology can profile samples of the size of whole mouse embryos in mid- or late-stage gestation with high definition. This poses a tremendous challenge for systematically studying the differentiation continuum that happens across different areas of the same tissue and for comparing different tissues simultaneously. Here, we report the development of a new DNB-based technology, Stereo-seq, that combines high resolution and sensitivity with large field of view to generate the first panoramic transcriptomic atlas of mouse organogenesis.

RESULTS

DNB patterned arrays enable large field-of-view spatially resolved transcriptomics with high definition

DNB sequencing is based on rolling circle amplification of DNA fragments (Drmanac et al., 2010), whose products are effectively docked into defined positions of a lithographically etched chip for *in situ* sequencing through automated high-throughput microscopic imaging. We envisaged that these features could lay the foundation for a spatially resolved transcriptomic technology with high-resolution and large field of view, which we developed as following. Standard DNB chips have spots with approximately 220 nm diameter and a center-to-center distance of 500 or 715 nm (**Figure 1A, step 1**). This provides up to 400 spots for tissue RNA capture per 100 μm^2 (average size of a mammalian cell). DNB templates containing random barcodes are deposited on the patterned array, incubated with primers, and sequenced to obtain the data matrix containing the coordinate identity (CID) of every DNB (**Figure 1A, step 2**). The use of random barcode-labeled DNB allows a large spatial barcode pool size (4^{25}). Next, unique molecular identifiers (UMI) and polyT sequence-containing oligonucleotides are ligated onto each spot through hybridization with an oligonucleotide sequence containing the CID (**Figure 1A, step 3**). Frozen tissue sections (10 μm thickness) are loaded onto

170 the chip surface, followed by fixation, permeabilization to capture the tissue
171 polyA-tailed RNA and finally reverse transcription plus amplification (**Figure**
172 **1A, step 4**). Amplified barcoded cDNA is collected, used as template for
173 library preparation and sequenced together with the CID (**Figure 1A, step 5**).
174 Computational analysis of sequencing data generated this way allows high-
175 resolution spatially resolved transcriptomics **(Figure 1A, step 6**). We named
176 this approach Stereo-seq (SpaTial Enhanced REsolution Omics-sequencing).
177 Importantly, Stereo-seq has a larger number of spots per 100 μm^2, with
178 smaller spot size and center-to-center distance, than other available methods
179 (**Figure 1B**). This makes it particularly suitable for detecting transcriptomic
180 gradients with high resolution and sensitivity. So far, we have used Stereo-seq
181 chips of up to an effective area of 13.2 cm x 13.2 cm for different tissue sizes,
182 subdivided into 50 mm^2, 100 mm^2 and 200 mm^2 smaller chips for profiling
183 sections from the mouse olfactory bulb (~10.5 mm^2), a whole mouse brain
184 (~52.8 mm^2) and whole mouse embryos (~7.1 to ~97.6 mm^2), respectively
185 (**Figure S1A**). These capture areas are substantially larger than those
186 achieved by other available technologies (**Figure 1B**), and we anticipate the
187 application of unsliced chips to much larger tissues such as whole human
188 brain sections (**Figure S1A**).

189 To benchmark our technology, we first profiled the mouse olfactory bulb
190 because it is a widely used model tissue for spatially resolved transcriptomic
191 approaches (Lebrigand et al., 2020b; Rodriques et al., 2019; Vickovic et al.,
192 2019). Stereo-seq captured numbers ranging on average 69 UMI per 2 μm
193 (diameter) bin (bin 3, 3 × 3 DNB), 1,450 UMI per 10 μm (diameter) bin (bin 14,
194 14 × 14 DNB, equivalent to ~1 medium size cell) and 133,776 UMI per 100 μm
195 (diameter) bin (bin 140, 140 × 140 DNB) (**Figure 1C and S1B**). This is
196 superior to other available technologies including Seq-Scope (848 UMI on
197 average per 10 μm diameter bin) (Cho et al., 2021a) when compared at the
198 same bin resolution.

199 Conventional cell taxonomy analysis with single-cell RNA-seq (scRNA-
200 seq) uses algorithms such as Leiden clustering to group cells based on
201 transcriptome similarity (Traag et al., 2019). Applying this method to spatially
202 resolved data, however, is problematic due to the lack of consideration of
203 spatial coordinates. Thus, we developed a spatially-constrained clustering

204 algorithm especially suited for high-resolution spatially resolved transcriptomic
205 data (**see Methods**), which clustered bins over a continuous area from which
206 tissue domains are annotated. This approach showed high level of
207 consistency between biological replicates corresponding to two adjacent
208 sections of the mouse olfactory bulb (R^2 = 0.963) (**Figure 1D, S1C, and S1D)**.
209 The distribution of specific markers (*Cdhr1*, *Pcp4*, *Slc17a7*, *Sox11* and *Th*)
210 captured by Stereo-seq exhibited remarkable similarity to *in situ* hybridization
211 (ISH) data (Lein et al., 2007), and showed clearer patterns than HDST or
212 Slide-seqV2 (**Figure 1E, S1C, and S1E**).
213 To further demonstrate the robustness of Stereo-seq and prove its
214 scalability, we profiled an entire adult mouse coronal brain section.
215 Unsupervised spatially-constrained clustering of the Stereo-seq data identified
216 different anatomical structures including the cortex and subcortical regions
217 such as hippocampus, thalamus and striatum (**Figure 1F**). This is so far the
218 largest brain spatial atlas profiled by a genome-wide sequencing based
219 spatial technology. Differentially expressed gene (DEG) and gene ontology
220 (GO) enrichment analyses confirmed the unique identity of the observed
221 structures (**Figure S2A and S2B**). When focusing on specific elements such
222 as the hippocampus (*Ncdn*$^+$ and *Neurod6*$^+$), thalamus (*Prkcd*$^+$), hypothalamus
223 (*Sparc*$^+$) and striatum (*Penk*$^+$), among others, we observed specific spatial
224 distribution of known markers (**Figure S2C**). Notably, we used a specific dye
225 for nucleic acids before *in situ* permeabilization to assess the resolution of the
226 data after sequencing. When zooming into a specific region corresponding to
227 the cortex, we observed substantial colocalization of the dye and the
228 aggregated transcripts detected by Stereo-seq (**Figure 1G**). This confirmed
229 that Stereo-seq captures transcripts at cellular resolution.
230 We concluded that Stereo-seq can be used to spatially characterize the
231 transcriptomic pattern of complex tissues in an unbiased multiplexed manner
232 with high definition and unprecedented field of view.
233

234 **Spatially resolved transcriptomic atlas of mouse organogenesis using**
235 **Stereo-seq**

236 We postulated that the unique features of Stereo-seq would allow us to create
237 panoramic transcriptomic maps of middle- and late-gestation mouse embryos

238 for which full body sections cannot be profiled using other available
239 technologies. This would also showcase the strength of Stereo-seq in
240 measuring spatiotemporal transcriptional dynamics at full scale. To this aim,
241 we created the beginning of Mouse Organogenesis Spatiotemporal
242 Transcriptomic Atlas (MOSTA), an expandable and interactive database for
243 spatial transcriptomic studies of mouse organogenesis. As proof of principle,
244 we profiled 14 sagittal sections (two sections per embryo) from C57BL/6
245 mouse embryos at E9.5 (~7.1 mm^2), E10.5 (~10.9 mm^2), E11.5 (~19.7 mm^2),
246 E12.5 (~30.2 mm^2), E13.5 (~55.2 mm^2), E15.5 (~93.2 mm^2) and E16.5 (~97.6
247 mm^2). These stages cover most of the key events in mouse organogenesis
248 (Cao et al., 2019).

249 To gain an unbiassed global view of MOSTA, we segmented our individual
250 embryo datasets into 50 × 50 DNB bins (bin 50 resolution, 36 μm diameter). In
251 total, we retrieved transcriptomic information for 616,125 bins. The average
252 number of captured genes per bin in each embryo ranged from 1,088 at E12.5
253 to 3,153 at E11.5, and of UMI from 3,473 at E13.5 to 10,939 at E11.5 (**Figure**
254 **S3A)**. Unsupervised spatially-constrained clustering showed the expected
255 major organs and systems (e.g., nervous system, heart, liver, lung, kidney,
256 adrenal gland, gastrointestinal tract, genitourinary tract, skin, bone and
257 muscle) at each respective time point, whose external boundaries closely
258 resembled the anatomical structures (**Figure 2A, S3B, and S3C**). DEG
259 analysis showed the expected correspondence with emerging tissue-specific
260 cell identities at individual stages (**Figure S4**). This was further confirmed by
261 plotting specific marker genes on the spatial maps across all embryonic time
262 points (**Figure 2B and S5**). Since Stereo-seq captures very high density of
263 signals, we also performed spatial re-clustering of bins for selected tissues,
264 which produced detailed structures containing different subregions (**Figure**
265 **2C**). For example, re-clustering of the E10.5 heart identified the atrium (*Myh6*$^+$)
266 and ventricle (*Myh7*$^+$/*Myl2*$^+$); of the E15.5 limb the cartilage primordium
267 (*Col2a1*$^+$), dermis (*Dcn*$^+$) and epidermis (*Krt15*$^+$); of the E16.5 spinal cord the
268 marginal (*Scng*$^+$), mantle (*Snrpn*$^+$/*Plxna2*$^-$) and ventricular zones
269 (*Snrpn*$^+$/*Plxna2*$^+$); and of the E16.5 adrenal gland the medulla (*Dbh*$^+$), cortex
270 (*Fdx1*$^+$) and capsule (*Col1a2*$^+$). Notably, reanalysis of E10 mouse embryo
271 DBiT-seq data (Liu et al., 2020) showed significantly fewer 50 μm-diameter

spots (902) than 36 μm diameter (bin 50)-bins (7,386) were calculated using Stereo-seq in an individual E10.5 section. Consequently, unsupervised clustering or mapping of specific genes failed to identify discernable anatomical structures with DBiT-seq (**Figure S6A and S6B**). This discrepancy is related to the large inter-channel space (50 μm) of DBiT-seq.

To study cell function enrichments within specific areas contained in the individual tissue clusters generated with Stereo-seq, we applied Hotspot (DeTomaso and Yosef, 2021), an algorithm that measures non-random variation to recognize informative gene programs. The latter is important because amalgamation of signals from different cell types and states in complex tissues such as the embryo can otherwise complicate the interpretations. We identified 28 gene modules for E9.5, 28 for E10.5, 33 for E11.5, 30 for E12.5, 24 for E13.5, 23 for E15.5 and 28 for E16.5 (**Figure 2D, 2E, and S7-S13; Table S1**). GO enrichment analysis demonstrated that most of these spatial gene modules correspond to features related to region-specific biological processes such as muscle development (module G1), neurogenesis (module G2), skin development (module G4), digestive system (module G13) and ossification (module G14) at E16.5 (**Figure 2D, 2E, and S13A; Table S1**). Then, we used a set of manually annotated cell types from a recent scRNA-seq atlas of E9.5-E13.5 mouse embryos (Cao et al., 2019) to assign putative cell identities to our spatial modules, observing good correlation. For example, genes specific to hepatocytes and erythroid lineage, megakaryocytes or neutrophils showed strong co-enrichment in the same module starting from E11.5 but were not earlier, consistent with the fact that the definitive hematopoiesis only occurs in the liver from E11.5 onwards (Lewis et al., 2021) (**Figure S9C**). Likewise, radial glial cells are the source of neuroblasts (Merkle et al., 2004) and both cell types co-localized in brain regions since E11.5. In addition, jaw and tooth progenitor cells co-localized with osteoblasts and connective tissue progenitor cells also after E11.5. The complete set of cell assignments for all tested time points can be found in **Figure S7-S13**.

Therefore, MOSTA generated by Stereo-seq constitutes a unique resource to investigate the molecular basis of tissue patterning and the emergence of cell identities during mouse organogenesis. Our publicly

306 available interactive data portal can be accessed at
307 https://db.cngb.org/stomics/mosta/.
308
309 **Spatiotemporal dynamics of gene regulation in mouse organogenesis**
310 Cell identity maintenance and cell state dynamics are governed by intrinsic
311 and inducible gene regulatory networks (Aibar et al., 2017). These networks
312 are often studied in the form of modules of co-expressed genes that are co-
313 regulated by common sets of transcription factors, or regulons (Aibar et al.,
314 2017). Although this data can be extracted from scRNA-seq datasets applying
315 algorithms such as SCENIC (Aibar et al., 2017), the lack of spatial information
316 muddles the establishment of reliable associations. We used SCENIC to
317 calculate the frequencies of predicted transcription factor binding events in
318 each of the individual time points of MOSTA. This identified many regulons
319 presenting regional specificity at each stage. To achieve a global overview of
320 these transcriptional programs and how they are interconnected, we applied
321 again Hotspot, which categorized them into a series of regulon modules
322 **(Table S2)**. Many of these modules contained sets of transcription factors
323 known to be involved in the formation of specific tissues and/or specific
324 developmental processes **(Figure 3A and S14-S19)**. For example, at E9.5 we
325 identified 23 modules containing a total of 410 regulons corresponding to
326 different tissues (**Figure 3A**). Among these, GATA4 was enriched in the heart
327 (module R1), GATA1 in the blood (module R2), SOX2 in the brain (module
328 R4), DLX6 in the branchial arch (module R10) FOXA2 in the notochord
329 (module R11) and HNF4A in the liver (module R18) (**Figure 3B**).
330 We focused on the brain for more detailed investigation because the
331 relatively large dimensions, unparalleled complexity and prolonged
332 developmental time makes particularly challenging the study of regulons with
333 single-cell sequencing approaches. First, we performed unsupervised
334 clustering of E9.5 brain regulons. This showed four major neuroepithelial
335 clusters (*Pax6*$^{+}$ and/or *Sox2*$^{+}$) corresponding to the telencephalon,
336 diencephalon, midbrain, and hindbrain, with a smaller neuroblast-like cluster
337 (*Nhlh1/2*$^{+}$) distributed in the diencephalon and more obviously in the hindbrain
338 (**Figure 3C and S20A**). Several transcription factors with known functions in
339 brain development showed differential activity among these regions (**Figure**

340 **3D-3F and S20B-S20D**). For example, the telencephalon was enriched in
341 EMX1/2, which regulate proliferation and specification of radial glial cells
342 (Bishop et al., 2003). The diencephalon was enriched in transcription factors
343 involved in thalamus specification (e.g., TCF7L2, BARHL2 and DBX1) (Lipiec
344 et al., 2020; Vue et al., 2007). EN1/2 were enriched in the anterior and
345 posterior midbrain and are known to regulate dopaminergic neuron
346 specification (Alves dos Santos and Smidt, 2011). Mid- and hindbrain shared
347 some regulons including BARHL1, which is known to be specifically enriched
348 in the adult cerebellum (part of the hindbrain) (Li et al., 2004), and LMX3.
349 Likewise, the early neuroblast regulon was enriched in transcription factors
350 characteristic of this cell type (e.g., SOX4, NEUROD1 and LHX1) (Liu et al.,
351 2000) (**Figure 3D and S20B**).

352 We next systematically examined the regulons that direct regional brain
353 specification across different time points. We focused on E9.5 and E12.5-
354 E16.5 because of the enhanced capture of related structures. We identified
355 regulon clusters controlling the formation and expansion of the diencephalon,
356 pallium, subpallium, midbrain, and hindbrain (**Figure 3G**). In the diencephalon,
357 the neuroepithelial regulons (e.g., DBX1 and BARHL2) identified at E9.5
358 became progressively inactivated after E12.5, whereas TCF7L2, BARHL2 and
359 DBX1 increase until E16.5 (**Figure 3H**). Another group of regulons comprising
360 factors associated with thalamus maturation (e.g., RORA and TFAP2B)
361 (Vitalis et al., 2018) appeared at E15.5 and remained high at E16.5. Several
362 regulons were shared between all stages (e.g., LEF1 and SHOX2) but their
363 activity increased towards E16.5, suggesting that fine-tuning their levels
364 orchestrates the transition from specification to maturation. Regulons in the
365 pallium (originated from the telencephalon) at later stages were divided into
366 the ventricular zone (VZ) and mantle zone (MZ) (**Figure 3G**). E9.5
367 telencephalon regulons progressively declined after this time point (**Figure**
368 **3H**). Many of the VZ-specific regulons showed transcription factors related to
369 early neurogenesis (e.g., EOMES, LHX2 and E2F family members) (Greig et
370 al., 2013) and remained high from E12.5 onwards (**Figure 3H**). In contrast,
371 those involved in MZ formation were related to neuronal maturation (e.g.,
372 CUX2 and BCL6), appeared at E13.5 and increased until E15.5 or E16.5.
373 Subpallium regulons showed strong enrichment of DLX homeobox

374 transcription factors (DLX1/2/5/6) from E13.5 to E16.5 (**Figure S20E and**
375 **S20F**), consistent with their role in GABAergic interneuron production (Sultan
376 et al., 2013). Midbrain and hindbrain largely showed similar sets of regulons
377 associated with neuron progenitor at early stage (e.g., E2F1, E2F5 and SP3),
378 but presented different set of transcription factors related to neuronal
379 maturation at later stages in each region (e.g., LEF1 and DMBX1 in the
380 midbrain, and HOXA5 and HOXB5 in the hindbrain) (**Figure S20E and S20F**).
381 We next investigated the spatial expression of diffusible extracellular cues
382 (morphogens) at the so-called secondary organizer centers of the developing
383 brain. These morphogens are responsible for inducing changes in gene
384 regulatory programs that cause regionalization in the brain (Tannahill et al.,
385 2005). We studied the earlier stages (E9.5 and E12.5) because the biggest
386 morphogenetic events of the brain happen during that period. Analysis of
387 gene modules identified with Hotspot showed good correspondence with the
388 known location of key secondary organizer centers including the floor plate
389 (FP), roof plate (RP), anterior neural ridge (ANR), zona limitans intrathalamica
390 (ZLI) and isthmus organizer (ISO) **(Figure S21A and S21B)**. Spatial
391 correlation analysis of ligands in these gene modules revealed distinct
392 clusters in each stage **(Figure S21C and S21D)**. These morphogen clusters
393 included ligands from the Sonic hedgehog (SHH), Wnt, bone morphogenetic
394 proteins (BMP), fibroblast growth factors (FGF) and R-spondin (RSPO)
395 families (Tannahill et al., 2005). We used this information to generate a spatial
396 morphogen map of the developing brain **(Figure 3I and S21E)**. Examples of
397 morphogens involved in dorsoventral patterning included *Wnt1*, *Wnt3a*, *Wnt9a*
398 and *Rspo1/2/3* at the RP, whereas *Shh* was mainly enriched at the FP and to
399 a less extent at the ZLI. Morphogens involved in anteroposterior patterning
400 included FGF family members such as *Fgf8* and *Fgf15* at the ANR, ZLI and
401 ISO. We noticed that regulons at these secondary organizers were quite
402 different and variable during development. For example, EN1/2 were enriched
403 at the ISO in both E9.5 and E12.5 embryos, while the ZLI was enriched in
404 DMBX1 and PAX6 at E9.5 or PRDM16 and MAFF at E12.5. In addition,
405 FOXA1/2/3 were enriched at the FP and OTX2 in the RP (**Figure S22**). These
406 results highlight the utility of Stereo-seq to study coordinated transcriptional
407 responses to signaling cues at large scale.

408 Regulons for other tissues also showed a gradual spatiotemporal
409 transition. For example, in the skeleton we identified regulons consisting of
410 the early condensation regulators SOX5 and SOX9 (Kozhemyakina et al.,
411 2015), which promote the transition from mesenchymal progenitors in the
412 sclerotome (E9.5-E11.5) to the early (cartilage primordium, E12.5 and E13.5)
413 and late (chondrocyte, E15.5 and E16.5) chondrogenic linage (**Figure S23A-**
414 **S23C**). Likewise, we detected key regulators of chondrocyte to osteoblast
415 maturation such as SP7 and XBP1 (Kozhemyakina et al., 2015), which
416 correlated with a switch in the pattern of extracellular matrix production from
417 *Col9a3* to *Col22a1*.
418 In summary, MOSTA can be used to infer the gene regulatory networks
419 behind patterning events driving organogenesis. Systematic analysis of other
420 regulons, morphogens and tissues can be performed using our interactive
421 portal.
422
423 **Regulation of cell diversification in the telencephalon**
424 The precise regulation of neuronal cell fate is critical for the development of
425 brain architecture, of which the neocortex is particularly interesting because of
426 the diversity of neuronal subtypes and the sophisticated migration trajectories
427 (Greig et al., 2013). We first focused on the late stage telencephalon (E15.5),
428 when the pallium and subpallium become apparent. Unsupervised spatially-
429 constrained clustering at bin 20 resolution (20 × 20 DNB, 14 μm diameter)
430 identified clusters corresponding to known anatomical regions **(Figure 4A)**.
431 These clusters displayed specific markers **(Figure S24A and S24B)**. Briefly,
432 we could clearly distinguish distinct pallium clusters including the dorsal
433 pallium (DPall), medial pallium (MPall, also known as hippocampal allocortex)
434 and ventral pallium (VPall). The DPall included clusters corresponding to the
435 VZ, subventricular zone (SVZ), intermediate zone (IZ), cortical plate (CP) and
436 marginal zone (MarZ). All subpallium regions expressed markers related to
437 the generation and maturation of cortical interneurons (e.g., *Dlx5* and *Gad2*;
438 **Figure S24A and S24B**) (Greig et al., 2013), and also markers corresponding
439 to known anatomical areas including the central subpallium (CSPall) and
440 paraseptal subpallium (PaSe) (https://developingmouse.brain-

441 map.org/static/atlas). Through enrichment of known genes, we further located
442 the striatum and lateral ganglionic eminence (LGE) (*Bcl11b, Foxp1/2, Isl1* and
443 *Ebf1*), medial ganglionic eminence (MGE) and preoptic area (POA) (*Nkx2.1,*
444 *Lhx6* and *Lhx8*) **(Figure 4A and S24C)**. Of note, the spatial clustering showed
445 two clusters along the rostral to caudal direction at the CP **(Figure 4A)**. DEG
446 analysis revealed graded distribution of genes related to axonogenesis and
447 neuron projection development along this axis **(Figure S25A and S25B)**,
448 reflecting different kinetics of projection neuron specification from partially
449 fate-restricted postmitotic progenitors (Greig et al., 2013). Interestingly, we
450 also observed a gradient of expression for morphogens such as *Nrg3* along
451 the rostral to caudal direction (Muller et al., 2018; Nowakowski et al., 2017)
452 **(Figure S25C and S25D; Table S3A)**.
453 We then applied SPOTlight (Elosua-Bayes et al., 2021) to map the cell
454 types into the spatial maps using a recently published neocortex single-cell
455 dataset (Di Bella et al., 2021). This detected a variety of neuronal and non-
456 neuronal cell types **(Figure 4B and S26A)**. The VZ and SZV largely showed
457 radial glial cells and intermediate progenitor cells, which decline at the IZ
458 being replaced by immature neurons. For cortical projection neurons, we
459 observed corticothalamic projection neuron (CThPN) in the inner CP in the
460 vicinity of immature neurons, and subcerebral projection neurons (SCPN)
461 mainly in the outer CP and more sparsely in the IZ. Consistent with our
462 findings above, we observed higher level of upper layer cortical projection
463 neurons (UL.CPN) in the rostral cluster of the CP, while deeper layer cortical
464 projection neurons (DL.CPN) had similar distribution.
465 To detect the directionality of gene expression changes in the developing
466 telencephalon, we applied Dynamo (**see Methods**), an analytical framework
467 that measures transcriptional dynamics to predict the emergence of cell fates
468 via vector field reconstruction (Qiu et al., 2021). In this regard, over 10% of
469 the Stereo-seq captured transcripts contained intronic reads **(Figure S26B)**,
470 comparable to the proportion captured by scRNA-seq (La Manno et al., 2018).
471 Spatial RNA velocity analysis revealed two strong directional flows of
472 transcriptional changes, one from VZ and SVZ towards the CP, and the other
473 from the subpallium to the cortical layers above it. The former direction is
474 consistent with the path of neuronal specification from progenitor cells

475 migrating radially towards the MZ, while the latter is consistent with the
476 tangential migration of interneurons from the MGE into the neocortex at
477 specific layers including the SVZ and IZ (Lodato and Arlotta, 2015) **(Figure**
478 **4C)**. This agrees with the observed spatial probability score of cortical
479 interneurons, projection neurons and neuron progenitors **(Figure 4B)**. To
480 study the regulators that guide interneuron and cortical neuron migration, we
481 performed pseudotime analysis along the migration paths **(Figure 4D and 4E;**
482 **see Methods)**. Interestingly, this showed both known regulators and unknown
483 potential regulators of neuronal migration. For example, the ephrin receptor
484 tyrosine kinases *Epha3, Epha4* and *Epha5*, were identified in the tangential
485 path of interneurons (Bevins et al., 2011) **(Figure S26C)**. Like wise, for radial
486 migration, we identified *Sox2* and *Pax6* associated with early neurogenesis,
487 and *Satb2* with projection neuron maturation (Alcamo et al., 2008; Gomez-
488 Lopez et al., 2011). Other identified regulators are listed in **Table S3** and
489 could be important for further study.

490 We next investigated the dynamic changes in projection neurons and
491 interneurons across developmental stages in neocortex regions from E11.5 to
492 E16.5 embryos. Unsupervised spatially-constrained clustering revealed
493 clusters corresponding to specific layers in each group **(Figure S27A)**. Single-
494 cell projection into these spatial maps revealed striking cell type diversification
495 during these stages. We observed that interneurons appear in the CP at
496 E13.5 and expand at E15.5 and E16.5. In contrast, CPN appeared early
497 (E12.5) and expanded and concentrated later at the IZ at E15.5 and E16.5.
498 SCPN appeared at E12.5 and resided at the upper CP layer at later stages,
499 while CThPN appeared later and resided at the inner CP layer **(Figure 4F,**
500 **S27B, and S27C)**. Cell cycle analysis further confirmed the dynamics from
501 early progenitor to later postmitotic transition at the CP **(Figure S27D)**.

502 Our results thus support the existence of spatiotemporal hierarchies
503 governing cell-type diversification in the developing telencephalon
504 (Nowakowski et al., 2017). Further scrutiny of this dataset using MOSTA
505 database will be invaluable for defining associations with potential functional
506 significance in the brain or other tissues.

507

508 **Deciphering developmental disease susceptibility using MOSTA**

509 Developmental diseases have been classically regarded as those producing
510 gross neonatal manifestations. Yet, many genetic conditions only manifested
511 after birth have a developmental, often unnoticed, component because their
512 target genes are also expressed during development (Boycott and Ardigo,
513 2018). For example, although Huntington's disease is a late-manifesting
514 neurological disorder affecting mostly the striatum, it is also associated with
515 abnormalities in cortex development (Barnat et al., 2020). Nowadays, scRNA-
516 seq datasets are becoming widely used to predict the origin and mechanisms
517 of genetic diseases including developmental diseases (Watanabe et al., 2019).
518 Yet, the cell capture bias and lack of contextual microenvironment affects the
519 conclusions.

520 Given its unique characteristics, MOSTA could be particularly useful to
521 dissect the developmental origins of mammalian genetic diseases, especially
522 for understanding what tissue regions are originally affected and when,
523 potentially shedding light into both big and subtle phenotypes. A major
524 advantage compared to data generated with other spatially resolved
525 technologies is the ability to look at multiple areas of the same tissue and
526 multiple tissues simultaneously across different embryonic stages. To
527 showcase this, we first took the 1,987 disease list (including 1,940 genes)
528 from the Deciphering Developmental Disorders (DDD) database (Firth et al.,
529 2011), filtered them to select the top 729 genes based on the expression
530 threshold in our own dataset **(Table S4)**, and projected both the filtered and
531 unfiltered genes onto our spatial transcriptomic maps for all developmental
532 time points. This showed enrichment in different tissues including the brain,
533 heart, liver, blood, bone, muscle and others **(Figure 5A and S28)**. Some of
534 these disease-related genes were expressed in most or all embryonic stages,
535 whereas others had a restricted window. Similarly, although many genes were
536 mainly enriched in one tissue (in some cases confined to a specific region) or
537 system, others were shared between several. For example, *Wnt5a*, which is
538 related to Robinow syndrome, located in the craniofacial region, genital ridge,
539 and brain (FP and neocortex) since early stages, consistent with the disease
540 phenotypes (Menezes et al., 2010) **(Figure 5B)**. *NKX2-1*, mutated in brain-
541 lung-thyroid syndrome (Shetty et al., 2014), was mainly enriched in brain
542 (hippocampus and subpallium) and lung. *Lmod3*, which is associated with

543 nemaline myopathy (Berkenstadt et al., 2018), was enriched in the skeletal
544 muscle.

545 Autism encompasses a complex and multifactorial (genetic and
546 environmental) group of neuropsychiatric diseases with recognized
547 developmental roots but poorly understood mechanisms (Lord et al., 2020).
548 Clarifying the diversity of tissues affected by autism besides the brain is
549 important for designing patient-specific management therapies, as it is often
550 associated with non-behavioral manifestations. We projected a battery of 161
551 autism-related genes (Liberzon et al., 2015) onto our spatial embryo maps,
552 observing grouping in different tissues **(Figure 5C; Table S4)**. Approximately
553 1/3 of the genes were enriched in the central nervous system (CNS), mostly
554 the brain, with predominance or not for certain regions. Some autism-related
555 genes were expressed along the whole developmental timeline, whereas
556 others were more restricted **(Figure 5C)**. For example, *Otx2* was enriched in
557 the midbrain, subthalamus and pallium at different stages, whereas *Tbr1* was
558 located mainly in the MZ of the pallium. Interestingly, a large group of autism
559 related genes were enriched in non-neural tissues (e.g., heart, liver, muscle,
560 bone and lung). For example, *Dmpk* was widely expressed in muscle but not
561 in the brain, suggesting that abnormalities of the former tissue indirectly cause
562 the autism phenotype **(Figure 5D)**.

563 These results demonstrate the utility of MOSTA for defining the
564 spatiotemporal windows of genetic disease vulnerability during development,
565 and for establishing expected and unexpected causal relationships. Manual
566 inclusion of other disease datasets can be used for case-specific explorations.
567
568

569 **DISCUSSION**

570

571 Topographic transcriptomic information is necessary to dissect the molecular
572 events driving mammalian development. Stereo-seq is a spatially resolved
573 transcriptomic technology with high resolution, sensitivity and large field of
574 view. These methodological parameters are all fundamental for reliably
575 profiling the transcriptomic heterogeneity of complex tissues and organisms
576 such as mammalian embryos. Whole mouse embryo-scale spatially resolved

transcriptomes have been reported recently (Liu et al., 2020; Srivatsan et al., 2021) but they contained low density of detected signals and were restricted to only one stage of organogenesis. The sparsity of gene detection in those studies makes it difficult to analyze gene expression gradients across the developing tissues and, thus, it is hard to recapitulate fine anatomical structures. We have used Stereo-seq to create the first version of MOSTA (https://db.cngb.org/stomics/mosta/), an expandable panoramic high-definition transcriptomic resource of mouse organogenesis. MOSTA provides detailed topographic information about the stepwise formation of tissues and the emergence of tissue-specific cell identities across different stages of mouse organogenesis. Examples of the latter include the identification of incipient areas of neuroblast specification in E9.5 brain subregions and of gradients of neuronal specification in the neocortex. One caveat of MOSTA is that some tissues such as the thyroid are underrepresented due to the sectioning procedure, whereas others will benefit from additional sections to fully capture the intricacy of developmental processes. It will also be important to include whole neonatal and adult mice for additional comparisons. In the future, we will add these samples and expand the number of sections with the goal of ultimately achieving 3D-transcriptomic reconstructions. Facilitating this goal, the precise spatial coordinates retrieved by Stereo-seq allow optimal integration of different slides, which might not be achieved with accuracy by techniques using randomly distributed beads. Moreover, being based on standard DNB technology it is relatively easy to enhance the sample throughput using Stereo-seq and systematically profile hundreds of tissue slices in a relatively short time.

To demonstrate the utility of MOSTA for inferring the molecular logic behind developmental processes, we have for the first time systematically dissected the spatially resolved gene regulatory networks driving organogenesis. This has identified tissue- and area-specific regulons across different embryonic stages and focusing on the brain we have also shown the correspondence with signaling cues responsible for inducing their diversification. In addition to understanding development, knowledge of these regulons and morphogens might be useful to devise or improve ways to reprogram somatic cells into other lineages *in vivo* or *in vitro* and for fine-

611 tuning differentiation protocols using pluripotent stem cells (Wang et al., 2021).
612 We have also projected the expression of developmental disease loci
613 (including among others monogenic diseases involving transcription factors or
614 morphogens and complex traits like autism) onto our spatial maps,
615 highlighting unexpected associations such as the localization of autism-
616 related genes in the muscle or the liver. Although mice and humans differ in
617 multiple aspects of normal physiology or disease and caution should be taken
618 with the interpretations, this approach has a tremendous potential to uncover
619 novel disease mechanisms. Systematic independent explorations using our
620 interactive portal will provide users worldwide with a unique chance to unlock
621 the black boxes of mouse embryogenesis and developmental diseases. In this
622 regard, expansion with datasets from genetically engineered mice that mimic
623 developmental diseases or bear alteration of developmental pathways will be
624 useful to test or refine any generated models of normal and abnormal
625 development generated with MOSTA.

626 Importantly, larger Stereo-seq chips could enable the profiling of embryos
627 from other mammalian species including primates. Forthcoming optimizations
628 of Stereo-seq will also increase gene and transcript capture, facilitating the
629 assignment of individual cell identities. Similarly, oligonucleotide-labeled
630 antibodies (Stoeckius et al., 2017) could be incorporated into the DNB for
631 simultaneous protein detection of surface markers, which would be useful for
632 identifying specific cell types (e.g., infiltrating immune cells). Likewise, we
633 anticipate that Stereo-seq will have other applications beyond RNA-
634 sequencing such as spatially resolved epigenomics (e.g., chromatin
635 accessibility and DNA methylation profiling). Accordingly, besides
636 development, Stereo-seq and its future technical variations will be highly
637 transformative for multiple research fields across kingdoms of life. Given its
638 characteristics and applicability Stereo-seq also has the potential to move into
639 the routine clinical practice as an extraordinary diagnostic tool complementary
640 to medical imaging and histopathology data.
641

642 **REFERENCES**

643

644 Aibar, S., Gonzalez-Blas, C.B., Moerman, T., Huynh-Thu, V.A., Imrichova, H., Hulselmans, G.,
645 Rambow, F., Marine, J.C., Geurts, P., Aerts, J.*, et al.* (2017). SCENIC: single-cell regulatory
646 network inference and clustering. Nat Methods *14*, 1083-1086. 10.1038/nmeth.4463.
647 Alcamo, E.A., Chirivella, L., Dautzenberg, M., Dobreva, G., Farinas, I., Grosschedl, R., and
648 McConnell, S.K. (2008). Satb2 regulates callosal projection neuron identity in the developing
649 cerebral cortex. Neuron *57*, 364-377. 10.1016/j.neuron.2007.12.012.
650 Alon, S., Goodwin, D.R., Sinha, A., Wassie, A.T., Chen, F., Daugharthy, E.R., Bando, Y., Kajita,
651 A., Xue, A.G., Marrett, K.*, et al.* (2021). Expansion sequencing: Spatially precise in situ
652 transcriptomics in intact biological systems. Science *371*. 10.1126/science.aax2656.
653 Alves dos Santos, M.T., and Smidt, M.P. (2011). En1 and Wnt signaling in midbrain
654 dopaminergic neuronal development. Neural Dev *6*, 23. 10.1186/1749-8104-6-23.
655 Barnat, M., Capizzi, M., Aparicio, E., Boluda, S., Wennagel, D., Kacher, R., Kassem, R.,
656 Lenoir, S., Agasse, F., Braz, B.Y.*, et al.* (2020). Huntington's disease alters human
657 neurodevelopment. Science *369*, 787-793. 10.1126/science.aax3338.
658 Berkenstadt, M., Pode-Shakked, B., Barel, O., Barash, H., Achiron, R., Gilboa, Y., Kidron, D.,
659 and Raas-Rothschild, A. (2018). LMOD3-Associated Nemaline Myopathy: Prenatal
660 Ultrasonographic, Pathologic, and Molecular Findings. J Ultrasound Med *37*, 1827-1833.
661 10.1002/jum.14520.
662 Bevins, N., Lemke, G., and Reber, M. (2011). Genetic dissection of EphA receptor signaling
663 dynamics during retinotopic mapping. J Neurosci *31*, 10302-10310.
664 10.1523/JNEUROSCI.1652-11.2011.
665 Bishop, K.M., Garel, S., Nakagawa, Y., Rubenstein, J.L., and O'Leary, D.D. (2003). Emx1 and
666 Emx2 cooperate to regulate cortical size, lamination, neuronal differentiation, development of
667 cortical efferents, and thalamocortical pathfinding. J Comp Neurol *457*, 345-360.
668 10.1002/cne.10549.
669 Boycott, K.M., and Ardigo, D. (2018). Addressing challenges in the diagnosis and treatment of
670 rare genetic diseases. Nat Rev Drug Discov *17*, 151-152. 10.1038/nrd.2017.246.
671 Cao, J., Spielmann, M., Qiu, X., Huang, X., Ibrahim, D.M., Hill, A.J., Zhang, F., Mundlos, S.,
672 Christiansen, L., Steemers, F.J.*, et al.* (2019). The single-cell transcriptional landscape of
673 mammalian organogenesis. Nature *566*, 496-502. 10.1038/s41586-019-0969-x.
674 Cho, C.S., Xi, J., Si, Y., Park, S.R., Hsu, J.E., Kim, M., Jun, G., Kang, H.M., and Lee, J.H.
675 (2021a). Microscopic examination of spatial transcriptome using Seq-Scope. Cell.
676 10.1016/j.cell.2021.05.010.
677 Cho, C.S., Xi, J., Si, Y., Park, S.R., Hsu, J.E., Kim, M., Jun, G., Kang, H.M., and Lee, J.H.
678 (2021b). Microscopic examination of spatial transcriptome using Seq-Scope. Cell *184*, 3559-
679 3572 e3522. 10.1016/j.cell.2021.05.010.
680 DeTomaso, D., and Yosef, N. (2021). Hotspot identifies informative gene modules across
681 modalities of single-cell genomics. Cell Syst *12*, 446-456 e449. 10.1016/j.cels.2021.04.005.

682 Di Bella, D.J., Habibi, E., Stickels, R.R., Scalia, G., Brown, J., Yadollahpour, P., Yang, S.M.,
683 Abbate, C., Biancalani, T., Macosko, E.Z.*, et al.* (2021). Molecular logic of cellular
684 diversification in the mouse cerebral cortex. Nature. 10.1038/s41586-021-03670-5.
685 Dobin, A., Davis, C.A., Schlesinger, F., Drenkow, J., Zaleski, C., Jha, S., Batut, P., Chaisson,
686 M., and Gingeras, T.R. (2013). STAR: ultrafast universal RNA-seq aligner. Bioinformatics *29*,
687 15-21. 10.1093/bioinformatics/bts635.
688 Drmanac, R., Sparks, A.B., Callow, M.J., Halpern, A.L., Burns, N.L., Kermani, B.G., Carnevali,
689 P., Nazarenko, I., Nilsen, G.B., Yeung, G.*, et al.* (2010). Human genome sequencing using
690 unchained base reads on self-assembling DNA nanoarrays. Science *327*, 78-81.
691 10.1126/science.1181498.
692 Elosua-Bayes, M., Nieto, P., Mereu, E., Gut, I., and Heyn, H. (2021). SPOTlight: seeded NMF
693 regression to deconvolute spatial transcriptomics spots with single-cell transcriptomes.
694 Nucleic Acids Res *49*, e50. 10.1093/nar/gkab043.
695 Eng, C.L., Lawson, M., Zhu, Q., Dries, R., Koulena, N., Takei, Y., Yun, J., Cronin, C., Karp, C.,
696 Yuan, G.C.*, et al.* (2019). Transcriptome-scale super-resolved imaging in tissues by RNA
697 seqFISH. Nature *568*, 235-239. 10.1038/s41586-019-1049-y.
698 Firth, H.V., Wright, C.F., and Study, D.D.D. (2011). The Deciphering Developmental Disorders
699 (DDD) study. Dev Med Child Neurol *53*, 702-703. 10.1111/j.1469-8749.2011.04032.x.
700 Gomez-Lopez, S., Wiskow, O., Favaro, R., Nicolis, S.K., Price, D.J., Pollard, S.M., and Smith,
701 A. (2011). Sox2 and Pax6 maintain the proliferative and developmental potential of gliogenic
702 neural stem cells In vitro. Glia *59*, 1588-1599. 10.1002/glia.21201.
703 Greig, L.C., Woodworth, M.B., Galazo, M.J., Padmanabhan, H., and Macklis, J.D. (2013).
704 Molecular logic of neocortical projection neuron specification, development and diversity. Nat
705 Rev Neurosci *14*, 755-769. 10.1038/nrn3586.
706 He, P., Williams, B.A., Trout, D., Marinov, G.K., Amrhein, H., Berghella, L., Goh, S.T., Plajzer-
707 Frick, I., Afzal, V., Pennacchio, L.A.*, et al.* (2020). The changing mouse embryo transcriptome
708 at whole tissue and single-cell resolution. Nature *583*, 760-+. 10.1038/s41586-020-2536-x.
709 Kozhemyakina, E., Lassar, A.B., and Zelzer, E. (2015). A pathway to bone: signaling
710 molecules and transcription factors involved in chondrocyte development and maturation.
711 Development *142*, 817-831. 10.1242/dev.105536.
712 La Manno, G., Soldatov, R., Zeisel, A., Braun, E., Hochgerner, H., Petukhov, V., Lidschreiber,
713 K., Kastriti, M.E., Lonnerberg, P., Furlan, A.*, et al.* (2018). RNA velocity of single cells. Nature
714 *560*, 494-498. 10.1038/s41586-018-0414-6.
715 Lebrigand, K., Bergenstråhle, J., Thrane, K., Mollbrink, A., Barbry, P., Waldmann, R., and
716 Lundeberg, J. (2020a). The spatial landscape of gene expression isoforms in tissue sections.
717 bioRxiv, 2020.2008.2024.252296. 10.1101/2020.08.24.252296.
718 Lebrigand, K., Bergenstråhle, J., Thrane, K., Mollbrink, A., Barbry, P., Waldmann, R., and
719 Lundeberg, J. (2020b). The spatial landscape of gene expression isoforms in tissue sections.
720 2020.2008.2024.252296. 10.1101/2020.08.24.252296 %J bioRxiv.
721 Lee, J.H., Daugharthy, E.R., Scheiman, J., Kalhor, R., Yang, J.L., Ferrante, T.C., Terry, R.,

722 Jeanty, S.S., Li, C., Amamoto, R.*, et al.* (2014). Highly multiplexed subcellular RNA
723 sequencing in situ. Science *343*, 1360-1363. 10.1126/science.1250212.
724 Lein, E.S., Hawrylycz, M.J., Ao, N., Ayres, M., Bensinger, A., Bernard, A., Boe, A.F., Boguski,
725 M.S., Brockway, K.S., Byrnes, E.J.*, et al.* (2007). Genome-wide atlas of gene expression in
726 the adult mouse brain. Nature *445*, 168-176. 10.1038/nature05453.
727 Lewis, K., Yoshimoto, M., and Takebe, T. (2021). Fetal liver hematopoiesis: from development
728 to delivery. Stem Cell Res Ther *12*, 139. 10.1186/s13287-021-02189-w.
729 Li, S., Qiu, F., Xu, A., Price, S.M., and Xiang, M. (2004). Barhl1 regulates migration and
730 survival of cerebellar granule cells by controlling expression of the neurotrophin-3 gene. J
731 Neurosci *24*, 3104-3114. 10.1523/JNEUROSCI.4444-03.2004.
732 Liberzon, A., Birger, C., Thorvaldsdottir, H., Ghandi, M., Mesirov, J.P., and Tamayo, P. (2015).
733 The Molecular Signatures Database (MSigDB) hallmark gene set collection. Cell Syst *1*, 417-
734 425. 10.1016/j.cels.2015.12.004.
735 Lipiec, M.A., Bem, J., Kozinski, K., Chakraborty, C., Urban-Ciecko, J., Zajkowski, T.,
736 Dabrowski, M., Szewczyk, L.M., Toval, A., Ferran, J.L.*, et al.* (2020). TCF7L2 regulates
737 postmitotic differentiation programmes and excitability patterns in the thalamus. Development
738 *147*. 10.1242/dev.190181.
739 Liu, M., Pereira, F.A., Price, S.D., Chu, M.J., Shope, C., Himes, D., Eatock, R.A., Brownell,
740 W.E., Lysakowski, A., and Tsai, M.J. (2000). Essential role of BETA2/NeuroD1 in development
741 of the vestibular and auditory systems. Genes Dev *14*, 2839-2854. 10.1101/gad.840500.
742 Liu, Y., Yang, M., Deng, Y., Su, G., Enninful, A., Guo, C.C., Tebaldi, T., Zhang, D., Kim, D., Bai,
743 Z.*, et al.* (2020). High-Spatial-Resolution Multi-Omics Sequencing via Deterministic Barcoding
744 in Tissue. Cell *183*, 1665-1681 e1618. 10.1016/j.cell.2020.10.026.
745 Lodato, S., and Arlotta, P. (2015). Generating neuronal diversity in the mammalian cerebral
746 cortex. Annu Rev Cell Dev Biol *31*, 699-720. 10.1146/annurev-cellbio-100814-125353.
747 Lord, C., Brugha, T.S., Charman, T., Cusack, J., Dumas, G., Frazier, T., Jones, E.J.H., Jones,
748 R.M., Pickles, A., State, M.W.*, et al.* (2020). Autism spectrum disorder. Nat Rev Dis Primers *6*,
749 5. 10.1038/s41572-019-0138-4.
750 Menezes, R., Letra, A., Kim, A.H., Kuchler, E.C., Day, A., Tannure, P.N., Gomes da Motta, L.,
751 Paiva, K.B., Granjeiro, J.M., and Vieira, A.R. (2010). Studies with Wnt genes and
752 nonsyndromic cleft lip and palate. Birth Defects Res A Clin Mol Teratol *88*, 995-1000.
753 10.1002/bdra.20720.
754 Merkle, F.T., Tramontin, A.D., Garcia-Verdugo, J.M., and Alvarez-Buylla, A. (2004). Radial glia
755 give rise to adult neural stem cells in the subventricular zone. Proc Natl Acad Sci U S A *101*,
756 17528-17532. 10.1073/pnas.0407893101.
757 Muller, T., Braud, S., Juttner, R., Voigt, B.C., Paulick, K., Sheean, M.E., Klisch, C.,
758 Gueneykaya, D., Rathjen, F.G., Geiger, J.R.*, et al.* (2018). Neuregulin 3 promotes excitatory
759 synapse formation on hippocampal interneurons. EMBO J *37*. 10.15252/embj.201798858.
760 Nichterwitz, S., Chen, G., Aguila Benitez, J., Yilmaz, M., Storvall, H., Cao, M., Sandberg, R.,
761 Deng, Q., and Hedlund, E. (2016). Laser capture microscopy coupled with Smart-seq2 for

762 precise spatial transcriptomic profiling. Nat Commun *7*, 12139. 10.1038/ncomms12139.
763 Nowakowski, T.J., Bhaduri, A., Pollen, A.A., Alvarado, B., Mostajo-Radji, M.A., Di Lullo, E.,
764 Haeussler, M., Sandoval-Espinosa, C., Liu, S.J., Velmeshev, D.*, et al.* (2017). Spatiotemporal
765 gene expression trajectories reveal developmental hierarchies of the human cortex. Science
766 *358*, 1318-1323. 10.1126/science.aap8809.
767 Okada, Y., Takeda, S., Tanaka, Y., Belmonte, J.I., and Hirokawa, N. (2005). Mechanism of
768 nodal flow: a conserved symmetry breaking event in left-right axis determination. Cell *121*,
769 633-644. 10.1016/j.cell.2005.04.008.
770 Peng, G., Suo, S., Cui, G., Yu, F., Wang, R., Chen, J., Chen, S., Liu, Z., Chen, G., Qian, Y.*, et*
771 *al.* (2019). Molecular architecture of lineage allocation and tissue organization in early mouse
772 embryo. Nature *572*, 528-532. 10.1038/s41586-019-1469-8.
773 Qiu, X., Mao, Q., Tang, Y., Wang, L., Chawla, R., Pliner, H.A., and Trapnell, C. (2017).
774 Reversed graph embedding resolves complex single-cell trajectories. Nat Methods *14*, 979-
775 982. 10.1038/nmeth.4402.
776 Qiu, X., Zhang, Y., Hosseinzadeh, S., Yang, D., Pogson, A.N., Wang, L., Shurtleff, M., Yuan,
777 R., Xu, S., Ma, Y.*, et al.* (2021). Mapping Transcriptomic Vector Fields of Single Cells. 696724.
778 10.1101/696724 %J bioRxiv.
779 Rodriques, S.G., Stickels, R.R., Goeva, A., Martin, C.A., Murray, E., Vanderburg, C.R., Welch,
780 J., Chen, L.M., Chen, F., and Macosko, E.Z. (2019). Slide-seq: A scalable technology for
781 measuring genome-wide expression at high spatial resolution. Science *363*, 1463-1467.
782 10.1126/science.aaw1219.
783 Shetty, V.B., Kiraly-Borri, C., Lamont, P., Bikker, H., and Choong, C.S. (2014). NKX2-1
784 mutations in brain-lung-thyroid syndrome: a case series of four patients. J Pediatr Endocrinol
785 Metab *27*, 373-378. 10.1515/jpem-2013-0109.
786 Srivatsan, S.R., Regier, M.C., Barkan, E., Franks, J.M., Packer, J.S., Grosjean, P., Duran, M.,
787 Saxton, S., Ladd, J.J., Spielmann, M.*, et al.* (2021). Embryo-scale, single-cell spatial
788 transcriptomics. Science *373*, 111-117. 10.1126/science.abb9536.
789 Stahl, P.L., Salmen, F., Vickovic, S., Lundmark, A., Navarro, J.F., Magnusson, J., Giacomello,
790 S., Asp, M., Westholm, J.O., Huss, M.*, et al.* (2016). Visualization and analysis of gene
791 expression in tissue sections by spatial transcriptomics. Science *353*, 78-82.
792 10.1126/science.aaf2403.
793 Stickels, R.R., Murray, E., Kumar, P., Li, J., Marshall, J.L., Di Bella, D.J., Arlotta, P., Macosko,
794 E.Z., and Chen, F. (2021). Highly sensitive spatial transcriptomics at near-cellular resolution
795 with Slide-seqV2. Nat Biotechnol *39*, 313-319. 10.1038/s41587-020-0739-1.
796 Stoeckius, M., Hafemeister, C., Stephenson, W., Houck-Loomis, B., Chattopadhyay, P.K.,
797 Swerdlow, H., Satija, R., and Smibert, P. (2017). Simultaneous epitope and transcriptome
798 measurement in single cells. Nat Methods *14*, 865-868. 10.1038/nmeth.4380.
799 Sultan, K.T., Brown, K.N., and Shi, S.H. (2013). Production and organization of neocortical
800 interneurons. Front Cell Neurosci *7*, 221. 10.3389/fncel.2013.00221.
801 Tannahill, D., Harris, L.W., and Keynes, R. (2005). Role of morphogens in brain growth. J

802 Neurobiol *64*, 367-375. 10.1002/neu.20163.
803 Traag, V.A., Waltman, L., and van Eck, N.J. (2019). From Louvain to Leiden: guaranteeing
804 well-connected communities. Sci Rep *9*, 5233. 10.1038/s41598-019-41695-z.
805 Vickovic, S., Eraslan, G., Salmen, F., Klughammer, J., Stenbeck, L., Schapiro, D., Aijo, T.,
806 Bonneau, R., Bergenstrahle, L., Navarro, J.F.*, et al.* (2019). High-definition spatial
807 transcriptomics for in situ tissue profiling. Nat Methods *16*, 987-990. 10.1038/s41592-019-
808 0548-y.
809 Vitalis, T., Dauphinot, L., Gressens, P., Potier, M.C., Mariani, J., and Gaspar, P. (2018).
810 RORalpha Coordinates Thalamic and Cortical Maturation to Instruct Barrel Cortex
811 Development. Cereb Cortex *28*, 3994-4007. 10.1093/cercor/bhx262.
812 Vue, T.Y., Aaker, J., Taniguchi, A., Kazemzadeh, C., Skidmore, J.M., Martin, D.M., Martin, J.F.,
813 Treier, M., and Nakagawa, Y. (2007). Characterization of progenitor domains in the
814 developing mouse thalamus. J Comp Neurol *505*, 73-91. 10.1002/cne.21467.
815 Wang, H., Yang, Y., Liu, J., and Qian, L. (2021). Direct cell reprogramming: approaches,
816 mechanisms and progress. Nat Rev Mol Cell Biol *22*, 410-424. 10.1038/s41580-021-00335-z.
817 Wang, X., Allen, W.E., Wright, M.A., Sylwestrak, E.L., Samusik, N., Vesuna, S., Evans, K., Liu,
818 C., Ramakrishnan, C., Liu, J.*, et al.* (2018). Three-dimensional intact-tissue sequencing of
819 single-cell transcriptional states. Science *361*. 10.1126/science.aat5691.
820 Watanabe, K., Umicevic Mirkov, M., de Leeuw, C.A., van den Heuvel, M.P., and Posthuma, D.
821 (2019). Genetic mapping of cell type specificity for complex traits. Nat Commun *10*, 3222.
822 10.1038/s41467-019-11181-1.
823 Xue, Z., Huang, K., Cai, C., Cai, L., Jiang, C.Y., Feng, Y., Liu, Z., Zeng, Q., Cheng, L., Sun,
824 Y.E.*, et al.* (2013). Genetic programs in human and mouse early embryos revealed by single-
825 cell RNA sequencing. Nature *500*, 593-597. 10.1038/nature12364.
826 Yao, Z., Liu, H., Xie, F., Fischer, S., Booeshaghi, A.S., Adkins, R.S., Aldridge, A.I., Ament, S.A.,
827 Pinto-Duarte, A., Bartlett, A.*, et al.* (2020). An integrated transcriptomic and epigenomic atlas
828 of mouse primary motor cortex cell types. bioRxiv, 2020.2002.2029.970558.
829 10.1101/2020.02.29.970558.
830 Zhuang, X. (2021). Spatially resolved single-cell genomics and transcriptomics by imaging.
831 Nat Methods *18*, 18-22. 10.1038/s41592-020-01037-8.
832
833
834 **ACKNOWLEDGMENTS**
835 We thank the MOTIC China Group CO., Ltd. for providing technical support,
836 and Rongqin Ke (Huaqiao University) and Jiazuan Ni (Shenzhen University)
837 for providing technical advice. We thank Jonathan S. Weissman (Whitehead
838 Institute) for providing helpful comments. This work was supported by the
839 Shenzhen Key Laboratory of Single-Cell Omics (ZDSYS20190902093613831)
840 and the Guangdong Provincial Key Laboratory of Genome Read and Write

(2017B030301011); Longqi Liu was supported by the National Natural Science Foundation of China (No.31900466); Miguel A. Esteban's lab at the Guangzhou Institutes of Biomedicine and Health was supported by the Strategic Priority Research Program of the Chinese Academy of Sciences (XDA16030502).

AUTHOR CONTRIBUTIONS

J.W., X.X., A.C., L.L., and Y.Li conceived the idea; J.W., X.X., A.C., L.L., Y. Li and M.A.E. supervised the work; A.C., S. Liao., L.L. and M.C. designed the experiment; S. Liao, J.Y. and W.L. generated the Stereo-seq chip with the help from X.C., X.H.[1,3] and D.F.; M.C., J.X., H.Z., H.X., L.H., P.G. and F.L. performed the majority of the experiments; K.M., L.W., X.L., X.T., H.L. and M. Li performed data preprocessing and quality evaluation; L.W., Y.Lai, X.Q., X. W. and S.H. analyzed the data; Z.L., Y.J., J.P., S.Liu, C.L., Zhi.Wang, Y.Yuan., Y.H., Q.L., Zhao.Wang, X.H.[1], F.Z., H.K., O.W., B.W. and H.L. provided technical support; G.V., C.W., , M.N., W.Z., F.M., Y.Yin, H.Y., P.M.-C., Q.W., J.M., J.P.T, M.Lisby, R.J.C and M.U. gave the relevant advice; M.A.E., J.W., X.X., L.L., Y.Lai, W.L. and A.C. wrote the manuscript.

DECLARATION OF INTERESTS

The chip, procedure and applications of Stereo-seq are covered in pending patents. Employees of BGI have stock holdings in BGI.

RESOURCE AVAILABILITY

Lead contact

Further information and requests for the resources and reagents may be directed to the corresponding author Xun Xu (xuxun@genomics.cn)

Material availability

All materials used for Stereo-seq are commercially available.

Data and code availability

875 All raw data generated by Stereo-seq have been deposited to CNGB
876 Nucleotide Sequence Archive (accession code: CNP0001543
877 (https://db.cngb.org/search/project/CNP0001543). All data were analyzed with
878 standard programs and packages. Custom code using open-source software
879 supporting the current study is available from the corresponding authors on
880 request and will be uploaded at https://github.com/BGIResearch/handleBam.
881
882
883 **METHODS**
884
885 **Tissue collection**
886 All relevant procedures involving animal experiments presented in this paper
887 are compliant with ethical regulations regarding animal research and were
888 conducted under the approval of the Animal Care and Use committee of the
889 Guangzhou Institutes of Biomedicine and Health, Chinese Academy of
890 Sciences (license number IACUC2021002). Mouse olfactory bulb and brain
891 were dissected from 12-week-old C57BL/6J female mice. E9.5, E10.5, E11.5,
892 E12.5, E13.5, E15.5 and E16.5 embryos were collected from pregnant
893 C57BL/6J female mice. After collection, tissues were snap-frozen in liquid
894 nitrogen prechilled isopentane in Tissue-Tek OCT (Sakura, 4583) and
895 transferred to a -80℃ freezer for storage before the experiment. Cryosections
896 were cut at a thickness of approximately 10 μm in a Leika CM1950 cryostat;
897 mouse olfactory bulb and mouse brain were cut coronally, mouse embryos
898 were cut sagittally.
899
900 **Stereo-seq chip preparation**
901 ***Generation of Stereo-seq chips.*** To generate the patterned array, we first
902 synthesized two oligo sequences: one containing 25 random
903 deoxynucleotides (nt)
904 (TGTGAGCCAAGGAGTTGNAACTGCTGACGTACTGAGAGGCATGGCGAC
905 CTTATCAGNNNNNNNNNNNNNNNNNNNNNNNNNNNTTGTCTTCCTAAGACC
906 G, Sangon) and the other a fixed sequence with phosphorylation
907 (/5phos/CTTGGCCTCCGACTTAAGTCGGATCGTAGCCATGTCGTTC,

908 Sangon). These two oligos were ligated by incubation with T4 ligase (NEB;
909 1U/μl T4 DNA ligase and 1× T4 DNA ligation buffer) and splint oligo
910 (TCGGAGGCCAAGCGGTCTTAGGAA, Sangon, 1 μM) at 37℃ for 2 hours.
911 The products were purified using the Ampure XP Beads (Vazyme, N411-03)
912 and then PCR amplified with the following steps: 95℃ for 5 minutes, 12 cycles
913 at 98℃ for 20 seconds, 58℃ for 20 seconds, 72℃ for 20 seconds and a final
914 incubation at 72℃ for 5 minutes. PCR products were purified using the
915 Ampure XP Beads (Vazyme, N411-03). DNBs were then generated by rolling
916 circle amplification and loaded onto the patterned chips according to the MGI
917 DNBSEQ-Tx sequencer manual. Next, to determine the distinct DNB-CID
918 sequences at each spatial location, single-end sequencing was performed
919 using a sequencing primer
920 (CTGCTGACGTACTGAGAGGCATGGCGACCTTATCAG, Sangon, 1 μM) in
921 a MGI DNBSEQ-Tx sequencer with SE25 sequencing strategy. After
922 sequencing, the capture oligo
923 (/5phos/TTGTCTTCCTAAGACNNNNNNNNNNTTTTTTTTTTTTTTTTTTTTTV,
924 Sangon, 1 μM) including 22 nt poly-T and 10 nt UMI was hybridized with the
925 DNB in 5× SSC buffer at 37℃ for 30 minutes, and then incubated with T4
926 ligase (NEB, 1 U/μl T4 DNA ligase, 1× T4 DNA ligation buffer and 0.5%
927 PEG2000) at 37℃ for 1 hour. This procedure produces capture probes
928 containing a 25 nt CID barcode, a 10 nt UMI and a 22 nt poly-T ready for poly-
929 A RNA capture. A schematic describing this procedure is included in the
930 MOSTA website (https://db.cngb.org/stomics/mosta/).
931 ***Calling of CID***. CID sequences together with their corresponding coordinates
932 for each DNB were determined using a base calling method according to
933 manufacturer's instruction of MGI DNBSEQ-Tx sequencer. After sequencing,
934 the capture chip was split into smaller size chips (5 mm × 10 mm, 10 mm × 10
935 mm, 10 mm × 20 mm) ready for use. At this stage, we filtered out all
936 duplicated CID that corresponded to non-adjacent spots.
937
938 **Stereo-seq library preparation and sequencing**
939 ***Tissue processing.*** Tissue sections were adhered to the Stereo-seq chip
940 surface and incubated at 37℃ for 3 minutes. Then, they were fixed in

941 methanol and incubated for 30 minutes at -20℃, after which they were ready
942 to be used for Stereo-seq. Where indicated, the same sections were stained
943 with nucleic acid dye (Thermo fisher, Q10212), or adjacent sections were
944 subjected to tissue histology examination using hematoxylin and eosin staining
945 according to standard procedure. Imaging for both procedures was performed
946 with a Ti-7 Nikon Eclipse microscope.

947 ***In situ reverse transcription.*** Tissue sections placed on the chip were
948 permeabilized using 0.1% pepsin (Sigma, P7000) in 0.01 M HCl buffer,
949 incubated at 37℃ for 12 minutes and then washed with 0.1× SSC buffer
950 (Thermo, AM9770) supplemented with 0.05 U/μl RNase inhibitor (NEB,
951 M0314L). RNA released from the permeabilized tissue and captured by the
952 DNB was reverse transcribed overnight at 42℃ using SuperScript II
953 (Invitrogen, 18064-014, 10 U/μl reverse transcriptase, 1 mM dNTPs, 1 M
954 betaine solution PCR reagent, 7.5 mM $MgCl_2$, 5 mM DTT, 2 U/ml RNase
955 inhibitor, 2.5 μM Stereo-TSO and 1× First-Strand buffer). After reverse
956 transcription, tissue sections were washed twice with 0.1× SSC buffer and
957 digested with Tissue Removal buffer (10 mM Tris-HCl, 25 mM EDTA, 100 mM
958 NaCl and 0.5% SDS) at 37℃ for 30 minutes. cDNA-containing chips were
959 then subjected to Exonuclease I (NEB, M0293L) treatment for 1 hour at 37℃
960 and were finally washed once with 0.1x SSC buffer.

961 ***Amplification.*** The resulting cDNA were amplified with KAPA HiFi Hotstart
962 Ready Mix (Roche, KK2602) with 0.8 μM cDNA-PCR primer. PCR reactions
963 were conducted as follows: first incubation at 95℃ for 5 minutes, 15 cycles at
964 98℃ for 20 seconds, 58℃ for 20 seconds, 72℃ for 3 minutes and a final
965 incubation at 72℃ for 5 minutes.

966 ***Library construction and sequencing.*** The concentrations of the resulting
967 PCR products were quantified by Qubit™ dsDNA Assay Kit (Thermo,
968 Q32854). A total of 20 ng of DNA were then fragmented with *in-house* Tn5
969 transposase at 55℃ for 10 minutes, after which the reactions were stopped by
970 the addition of 0.02% SDS and gently mixing at 37℃ for 5 minutes after
971 fragmentation. Fragmentation products were amplified as described below: 25
972 ml of fragmentation product, 1× KAPA HiFi Hotstart Ready Mix and 0.3 μM

973 Stereo-Library-F primer, 0.3 μM Stereo-Library-R primer in a total volume of
974 100 ml with the addition of nuclease-free H_2O. The reaction was then run as:
975 1 cycle of 95℃ 5 minutes, 13 cycles of (98℃ 20 seconds, 58℃ 20 seconds
976 and 72℃ 30 seconds) and 1 cycle of 72℃ 5 minutes. PCR products were
977 purified using the Ampure XP Beads (Vazyme, N411-03) (0.6× and 0.15×),
978 used for DNB generation and finally sequenced (35 bp for read 1, 100 bp for
979 read 2) on a MGI DNBSEQ-Tx sequencer.
980

981 **Stereo-seq raw data processing**

982 Fastq files were generated using a MGI DNBSEQ-Tx sequencer. CID and
983 UMI are contained in the read 1 (CID: 1-25bp, UMI: 26-35bp) while the read 2
984 consist of the cDNA sequences. CID sequences on the first reads were first
985 mapped to the designed coordinates of the *in situ* captured chip achieved
986 from the first round of sequencing, allowing 1 base mismatch to correct for
987 sequencing and PCR errors. Reads with UMI containing either N bases or
988 more than 2 bases with quality score lower than 10 were filtered out. CID and
989 UMI associated with each read were appended to each read header.
990 Retained reads were then aligned to the reference genome (mm10) using
991 STAR (Dobin et al., 2013) and mapped reads with MAPQ ≥10 were counted
992 and annotated to their corresponding genes using *handleBam* (available at
993 https://github.com/BGIResearch/handleBam). UMI with the same CID and the
994 same gene locus were collapsed, allowing 1 mismatch to correct for
995 sequencing and PCR errors. Finally, this information was used to generate a
996 CID-containing expression profile matrix.
997

998 **Unsupervised spatially-constrained clustering of Stereo-seq data**

999 Expression profile matrix was divided into non-overlapping bins covering an
1000 area of X × X DNB, with X ∈ (*1, 3, 14, 50, 140*) and the transcripts of the
1001 same gene aggregated within each bin. After this step, data were log-
1002 normalized in Scanpy and spatially-constrained unsupervised clustering was
1003 performed. In brief, to include spatial information during clustering, we first
1004 built a spatial k-nearest neighbor graph $G_{spatial}^{k_1}$ (k_1 is by default set to be 8
1005 as each bin has 8 nearest spatial neighbors) using Squidpy and then took the

union with the k-nearest neighbor graph $G^{k_2}_{expression}$ based on transcriptomic data (k_2 is by default set to be 30). The combined graph ($G_{combined} = G^{k_1}_{spatial} \cup G^{k_2}_{expression}$) was then used as input for leiden clustering. Further, each cluster was annotated based on the cluster specific markers identified by the rank_genes_groups function of scanpy using default parameters as well as the anatomical annotation based on eHistology Kaufman Annotations (http://www.emouseatlas.org/emap/home.html) or Allen Brain Atlas (http://mouse.brain-map.org/).

Comparison of Stereo-seq with other published methods

HDST data (Vickovic et al., 2019) were taken from GSE130682, SLIDE-seqV2 data (Stickels et al., 2021) from the Single Cell Portal of the Broad Institute, DBiT-seq data (Yao et al., 2020) from GSE137986, and Visium data (Lebrigand et al., 2020b) from GSE153859, Seq-Scope data were taken from GSE169706 (Cho et al., 2021a). For **Fig. 1c**, to ensure that proper comparisons were made, the data of Stereo-seq were binned into bin 3 (3 × 3 resolution, ~2 μm diamater), bin 14 (14 × 14 resolution, ~10 μm diamater) or bin 140 (140 × 140 resolution, ~100 μm diamater). For **Extended Data Fig. 1e**, data from HDST were binned into bin 5 (5 × 5, ~10 μm diamater).

Spatially-resolved gene regulatory networks

The analysis of regulon activity was performed by following the standard SCENIC pipeline (Aibar et al., 2017). The input to SCENIC was the bin 50 (50 x 50 resolution) expression matrix. The expression matrix was loaded into GENIE3 and the co-expressed gene network for each transcription factor was constructed. Transcription factor co-expression modules were then analyzed by RcisTarget and their potential targets further filtered by default parameters. Filtered potential targets were used to build the regulons. Regulon activity (Area Under the Curve) was analyzed by AUCell and the active regulons were determined by AUCell default threshold. The activity of regulons for each bin was then mapped to the physical space. The gene network for **Figure 3F** was constructed by selecting the target genes of corresponding transcription factors related to neuronal development, and further visualized by Cytoscape.

1039 **Identification of spatially auto-correlated gene or regulon modules**
1040 Spatially auto-correlated gene or regulon modules were identified using
1041 Hotspot (DeTomaso and Yosef, 2021). The expression matrix for the top
1042 5,000 variable genes and all regulon activity matrix of each embryo were used
1043 as input. For gene module, the data were first normalization by the total UMI
1044 number of each bin, then create knn graph of genes using the
1045 create_knn_graph function with the parametes: n_neighbors = 30 (for regulon,
1046 n_neighbors = 10), then genes or regulons with significant spatial
1047 autocorrelation (FDR < 0.05) were kept for further analysis. And the modules
1048 were identified using the create_modules with the parameters:
1049 min_gene_threshold = 20 and fdr_threshold = 0.05 (for the regulon:
1050 min_gene_threshold = 5 and fdr_threshold = 0.05).
1051
1052 **Deconvolution of cell types**
1053 We applied SPOTlight (Elosua-Bayes et al., 2021) to deconvolute and map all
1054 cell types in the murine telencephalon. Mouse embryonic cortex scRNA-seq
1055 data were retrieved from GSE153164 (Di Bella et al., 2021). We chose cell
1056 type with the highest probability out of all cell types provided by the
1057 spotlight_deconvolution function with commendatory parameters as the final
1058 cell type for each bin. The cell type specific proportions were projected to the
1059 physical space.
1060
1061 **Rostral-caudal brain gene expression dynamics**
1062 The CP of E15.5 telencephalon was manually dissected into 16 blocks along
1063 the rostral-caudal direction based on spatial coordinates. Variable genes
1064 along the rostral to caudal axis were identified using the differentialGeneTest
1065 function of monocle (Qiu et al., 2017) based on the corrdinates of the blocks.
1066 Then DEG along the rostral-caudal axis were identified with $p < 0.05$.
1067
1068 **RNA velocity analysis**
1069 Analysis was performed using Dynamo (Qiu et al., 2021) following the tutorial
1070 found at https://dynamo-release.readthedocs.io/. Unspliced and spliced RNA
1071 for each bin (20 × 20 resolution) were extracted from E15.5 telencephalon
1072 region with handleBam. The data matrix was then processed by Dynamo to

1073 normalize the expression, select feature genes and perform dimension
1074 reduction via UMAP, followed by default parameters to estimate the kinetic
1075 parameters and gene-wise RNA velocity vectors that were then projected to
1076 the physical space. Specifically, the new “Fokker-Planck” kernel implemented
1077 in Dynamo instead of the conventional correlation or cosine kernel was used
1078 for the projection of high-dimensional RNA velocity vectors to physical space.
1079 Streamlines were used to visualize the velocity vector flows on telencephalon
1080 in which only velocity flows for the relevant domains are visualized. To
1081 facilitate the understanding of gene expression dynamics over space, we first
1082 reconstructed the continuous vector field in the UMAP space, and then
1083 utilized a new method, hodge decomposition, implemented in Dynamo that
1084 takes the simplicial complexes (a sparse directional graph) constructed based
1085 on the learned vector field function to infer the vector field based pseudotime
1086 (vf pseudotime). At last, we also illustrated the kinetics of all genes with
1087 highest PCA loading as well as the DEG identified by spatially-constrained
1088 clustering along the vf pseudotime.
1089

1090 **Spatial gene enrichment analysis of human developmental disease**
1091 **associated genes**

1092 A list of 1,940 genes corresponding to monogenic diseases was retrieved
1093 from DDG2P (version 2.29). The gene set related to autism were taken from
1094 MSigDB (Liberzon et al., 2015). For monogenic disease analysis, genes with
1095 depth-normalized expression value greater than 1(729 genes) were kept for
1096 further analysis. The expression level of indicated organs at selected time
1097 point were aggregated, Z score normalized, and further visualized by heatmap.
1098
1099

1100 **FIGURE LEGENDS**

1101

1102 **Figure 1. Advanced RNA capture from complex tissues by Stereo-seq.**

1103 **A.** Stereo-seq pipeline. *Step 1*, design of the DNB patterned array chip. *Step*
1104 *2*, *in situ* sequencing to determine the spatial coordinates of uniquely
1105 barcoded oligonucleotides placed on each spot of the chip. *Step 3*,
1106 preparation of capture probes by ligating the UMI-polyT containing

1107 oligonucleotides to each spot. *Step 4*, subsequent *in situ* RNA capture
1108 from tissue placed on the chip. *Step 5*, cDNA amplification, library
1109 construction and sequencing. *Step 6*, data analysis to generate the
1110 spatially resolved transcriptome of the profiled tissue.

1111 **B.** Stereo-seq achieves a smaller spot size (upper left), higher resolution
1112 (upper right), higher number of spots per 100 μm^2 (bottom left) and larger
1113 capture area (bottom right) than other reported methods. Samples used
1114 for the comparison included mouse olfactory bulb (Stereo-seq, Visium,
1115 Slide-seqV2 and HDST), E10 mouse embryo (DBiT-seq) and mouse liver
1116 (Seq-Scope) (Cho et al., 2021b; Lebrigand et al., 2020a; Liu et al., 2020;
1117 Stickels et al., 2021; Vickovic et al., 2019). Note that since Seq-Scope
1118 uses a random array, which contains no patterned spots, the size of each
1119 pixel was estimated according to the published dataset.

1120 **C.** Boxplots showing the number of transcripts captured by Stereo-seq at the
1121 indicated resolution in comparison with reported HDST, Slide-seqV2,
1122 Visium, DBiT-seq and Seq-Scope datasets. Samples in those datasets
1123 used for comparison are as in **panel B**.

1124 **D.** Unsupervised spatially-constrained clustering of the mouse olfactory bulb
1125 section analyzed by Stereo-seq data at bin 14 resolution, bins were
1126 colored by their annotation. ONL, olfactory nerve layer. OPL, outer
1127 plexiform layer. GL, glomerular layer. GCL-D, granular cell zone deep.
1128 GCL-E, granular cell layer externa. GCL-I, granular cell layer internal. IPL,
1129 internal plexiform layer. ML, mitral layer. SEZ, subependymal zone. Scale
1130 bar, 500 μm.

1131 **E.** Left: spatial visualization of *Cdhr1* in a mouse olfactory bulb section
1132 analyzed by Stereo-seq. Right: *Cdhr1* ISH data taken from Allen Brain
1133 Atlas. Scale bars, 500 μm.

1134 **F.** Unsupervised spatially-constrained clustering of the mouse brain section
1135 analyzed by Stereo-seq at bin 50 resolution, bins were colored by their
1136 annotation. Scale bar, 500 μm.

1137 **G.** Left: projection of captured DNB signals of the same region squared in the
1138 **panel F**. Scale bar, 50 μm. Right: superimposed nucleic acid staining and
1139 captured DNB signals from the same region squared in the middle panel.
1140 Scale bar, 10 μm.

1141 **Figure 2. Spatiotemporal transcriptomic atlas of mouse organogenesis.**

1142 **A.** Unsupervised spatially-constrained clustering of mouse embryo sections
1143 across E9.5, E10.5, E11.5, E12.5, E13.5, E15.5, and E16.5, bins were
1144 colored by their annotation. The squares indicate the regions for analysis
1145 in **panel C**. Scale bar, 1 mm.

1146 **B.** Spatial visualization of expression of indicated genes for muscle,
1147 epidermis, cartilage primordium, and nervous system. Scale bar, 1 mm.

1148 **C.** Spatial visualization of indicated areas in **panel A** identified detailed
1149 anatomical structure for the heart (E10.5), limb (E15.5), spinal cord
1150 (E16.5), and adrenal gland (E16.5). The expression of marker genes for
1151 each anatomical structure is shown on the right side of each area. Scale
1152 bars, 500 μm.

1153 **D.** Heatmap showing the genes with significant spatial autocorrelation (3,240
1154 genes, FDR < 0.05) grouped into 28 gene modules on the basis of
1155 pairwise spatial correlations of E16.5 embryo. Selected genes and GO
1156 terms related to representative gene modules are highlighted on the right
1157 side.

1158 **E.** Spatial visualization of indicated gene module related to muscle, cartilage
1159 primordium, connective tissue, pancreas, epidermis, GI tract, and nervous
1160 system. Scale bar, 1 mm.

1161

1162 **Figure 3. Spatially resolved gene regulatory networks of organogenesis.**

1163 **A.** Heatmap showing the regulons with significant spatial autocorrelation
1164 (481 regulons, FDR < 0.05) grouped into 23 modules on the basis of
1165 pairwise spatial correlations of E9.5 embryo section, selected regulons
1166 and their corresponding GO terms related to representative regulon
1167 modules are highlighted on the right side.

1168 **B.** Spatial visualization of indicated modules and their representative regulon
1169 for heart, blood, brain, branchial arch, notochord, and liver. Scale bar, 500
1170 μm.

1171 **C.** Unsupervised spatially-constrained clustering of E9.5 mouse embryonic
1172 brain based on regulon activity. Tel: telencephalon; Die: diencephalon; Mb:
1173 midbrain; Hb: hindbrain. Scale bar, 500 μm.

1174 **D.** Heatmap showing the normalized regulon activity score of top

1175 transcription factors corresponding to different anatomical structures of
1176 E9.5 brain.
1177 **E.** Spatial visualization of the indicated regulon activity representing different
1178 anatomical structures of E9.5 brain. Scale bar, 500 μm.
1179 **F.** Gene regulatory network of transcription factors (EMX1/2) representing
1180 telencephalon (EMX1/2), diencephalon (TCF7L2 and DBX1), midbrain
1181 (EN1/2), and mid-hindbrain (BARHL1 and MSX3) of E9.5 brain as
1182 visualized by Cytoscape. Selected target genes related to neuronal
1183 development was shown.
1184 **G.** Unsupervised spatially-constrained clustering of mouse embryonic brain
1185 from E9.5, E12.5, E13.5, E15.5 and E16.5 based on regulon activity
1186 identified anatomical structures of the developing brain. MZ: mantle zone;
1187 VZ: ventricular zone; Pall, pallium; Spall, subpallium; Th, thalamus, Pth,
1188 prethalamus; Hy, hypothalamus; Mb-Hb, mammillary body - hindbrain.
1189 Scale bars, 500 μm.
1190 **H.** Heatmaps showing the normalized regulon activity score of top
1191 transcription factors corresponding to mouse embryonic diencephalon
1192 (top) or pallium (bottom) development.
1193 **I.** Upper left: schematic representation of the secondary organizer centers in
1194 the early embryo brain. Bottom: Spatial scatter plots showing single DNB
1195 that captured the transcripts for the indicated morphogens at the ISO,
1196 ANR, ZLI, RP, and FP at E9.5 (bottom left) and E12.5 (bottom right)
1197 embryos. Plots were superimposed with E9.5 or E12.5 brain structures.
1198 ISO, isthmus organizer; ANR, anterior neural ridge; ZLI, zona limitans
1199 intrathalamica; RP, roof plate; FP, floor plate. Scale bars, 500 μm.
1200
1201 **Figure 4. Cell type diversification during neocortex development.**
1202 **A.** Unsupervised spatially-constrained clustering of the forebrain from E15.5
1203 embryo identified anatomical structures (bin 20 resolution). Bins are
1204 colored by their annotated structures. CP-C, cortical plate - caudal; CP-R,
1205 cortical plate - rostral; MarZ, marginal zone; MPall, medial pallium; VPall,
1206 ventral pallium; CSPall, central subpallium; PaSe, paraseptal subpallium;
1207 StrV, ventricular zone of subpallium; ChP, choroid plexus. Scale bar, 500
1208 μm.

1209 **B.** Left: spatial visualization of the indicated cell type proportion score for the
1210 E15.5 forebrain. Right: dotplot showing the cell type composition at
1211 different anatomical structures of the E15.5 forebrain. Ap. Prog, apical
1212 progenitor; Int. prog., intermediate progenitor; Imm. neu., immature
1213 neurons; Mig. Neu. migrating neuron; SCPN, subcerebral projection
1214 neurons; DL. CPN, deeper layer callosal projection neuron; UL. CPN,
1215 upper layer callosal projection neuron; CThPN, corticothalamic projection
1216 neuron; IN, Interneuron. CR, Cajal-Retzius cell. EC, endothelial cell.
1217 VLMC, vascular and leptomeningeal cell. Scale bar, 500 μm.
1218 **C.** RNA velocity streamline plots visualize the developmental trajectory of the
1219 forebrain. Bins are colored by their annotated structures, as in **panel A**.
1220 Scale bar, 500 μm.
1221 **D.** Vector field pseudotime analysis of tangential migration of interneuron
1222 neurons (upper) and radial migration of cortical neuron (bottom). Scale
1223 bar, 500 μm.
1224 **E.** Gene expression heatmap of 680 top PCA genes in a pseudo-temporal
1225 order of tangential migration (upper) and radial migration path (bottom),
1226 genes with highest PCA loading as well as the DEG identified by
1227 unsupervised spatially-constrained clustering were shown in the figure.
1228 **F.** Dotplot showing the cell type composition dynamic for the mouse
1229 embryonic cortex at E11.5, E12.5, E13.5, 15.5, and E16.5.
1230
1231 **Figure 5. Association of MOSTA profiles with human developmental**
1232 **disorders.**
1233 **A.** Heatmap showing the normalized expression level of 729 genes selected
1234 from the Deciphering Developmental Disorders database in six
1235 representative anatomical structures (brain, bone, muscle, heart, liver and
1236 lung) in embryos from E9.5 to E16.5.
1237 **B.** Spatial visualization of expression of indicated genes related to the
1238 human developmental disorders (Robinow syndrome, brain-lung-thyroid
1239 syndrome and nemaline myopathy) in mouse embryos from E9.5 to E16.5.
1240 Disease- related structures are annotated in the figure.
1241 **C.** Heatmap showing the normalized expression level of 161 autism-related
1242 genes in six representative anatomical structures (brain, bone, muscle,

1243 heart, liver and lung) in mouse embryos from E9.5 to E16.5.
1244 **D.** Spatial visualization of specific genes associated with autism (*Dmpk*, *Tbr1*,
1245 and *Otx2*) in the embryo brain from E9.5 to E16.5. Disease-related
1246 structures are annotated in the figures.
1247
1248 **Figure S1. Size of stereo-seq chips and assessment of performance,**
1249 **related to Figure 1.**
1250 **A.** Stereo-seq chips of different sizes ranging from 50 mm^2 to 174.24 cm^2.
1251 **B.** Spatial visualization of the number of UMI captured by Stereo-seq from
1252 two adjacent mouse olfactory bulb coronal sections at bin 14 resolution.
1253 **C.** Unsupervised spatially-constrained clustering of the mouse olfactory bulb
1254 section (section 2) at bin 14 resolution.
1255 **D.** Pearson correlation coefficient (R^2 = 0.9666) of pseudo-bulk profiles from
1256 the two Stereo-seq experiments of mouse olfactory bulb.
1257 **E.** Spatial visualization of the indicated genes in the two independent Stereo-
1258 seq experiments for mouse olfactory bulb and reported HDST, Slide-
1259 seqV2 and ISH datasets (Lein et al., 2007; Stickels et al., 2021; Vickovic
1260 et al., 2019). Scale bars, 500 μm.
1261
1262 **Figure S2. Stereo-seq detects different anatomical structures in the**
1263 **adult mouse brain, related to Figure 1.**
1264 **A.** Heatmap showing the mean expression level of DEG between the
1265 indicated anatomical structures identified in **Figure 1F**.
1266 **B.** GO analysis of DEG between the indicated anatomical structures.
1267 Selected GO terms (Benjamini-Hochberg corrected *P* value) are shown.
1268 **C.** Spatial visualization of the expression of indicated genes representing
1269 different anatomical structures in a whole adult mouse brain coronal
1270 section analyzed by Stereo-seq at bin 50 resolution. Gene expression
1271 levels were quantified as $\log_2$ (transcripts per 10K UMI + 1), which applies
1272 to all similar plots.
1273
1274 **Figure S3. Spatially resolved transcriptomic atlas of mouse**
1275 **organogenesis, related to Figure 2.**
1276 **A.** Violin plot showing the number of transcripts (left) and genes (right)

1277 captured by Stereo-seq at different stages of embryonic development,
1278 related to **Figure 2A**.
1279 **B.** Top: overview of the sampled embryonic time points and sections. Middle
1280 and bottom: spatially-constrained unsupervised clustering of additional
1281 embryo sections across E9.5, E10.5, E11.5, E12.5, E13.5, E15.5, and
1282 E16.5 also identifies anatomical structures (annotation is shown below).
1283 Bins are colored according to different anatomical structures. Scale bar, 1
1284 mm.
1285 **C.** Hematoxylin and eosin staining of embryo sections adjacent to the
1286 corresponding Stereo-seq sections. Scale bars, 1 mm.
1287
1288 **Figure S4. DEG of mouse embryo anatomical structures**, **related to**
1289 **Figure 2**.
1290 Heatmap showing the normalized expression of DEGs for the indicated
1291 anatomical structures of the mouse embryo sections profiled by Stereo-seq in
1292 **Figure 2A**.
1293
1294 **Figure S5. Expression of selected markers for specific mouse embryo**
1295 **tissues, related to Figure 2.**
1296 Spatial visualization of the expression of DEGs enriched in the indicated
1297 tissues of the mouse embryo sections profiled by Stereo-seq in **Figure 2A**.
1298
1299 **Figure S6. Reanalysis of a mouse E10 embryo dataset generated by**
1300 **DBiT-seq, related to Figure 2.**
1301 **A.** Spatial heatmap indicating the number of UMI captured by Stereo-seq
1302 from an E10.5 embryo section (same as in **Figure 2A**) at bin 50 (left)
1303 compared to an E10 DBiT-seq dataset at the same resolution (right).
1304 Scale bar, 500 μm.
1305 **B.** Spatial visualization of the expression of the indicated genes in Stereo-
1306 seq (upper panels) and DBiT-seq (lower panels) mouse embryo datasets.
1307 Scale bars, 500 μm.
1308
1309 **Figure S7-S12. | Hotspot identified spatial gene expression modules in**
1310 **E9.5-E15.5 mouse embryo sections, related to Figure 2**.

1311 **A.** Heatmap showing the genes with significant spatial autocorrelation
1312 (2,082, 1,916, 3,062, 2,831, 2,074, 2,480 genes, FDR < 0.05) grouped
1313 into 28, 28, 33, 30, 24 and 23 gene modules based on pairwise spatial
1314 correlations of gene expression in the same embryo sections of **Figure**
1315 **2A** from E9.5 to E15.5, respectively. Selected genes and GO terms
1316 related to representative modules are highlighted on the right side.
1317 **B.** Heatmap showing the Pearson correlation of module score for each
1318 spatial autocorrelation module and the expression of sets of specific
1319 genes for each cell type from a reported dataset (Cao et al., 2019).
1320 **C.** Spatial visualization of gene modules related to the indicated anatomical
1321 structures. Scale bar, 1 mm.
1322
1323 **Figure S13. Hotspot identified spatial gene expression modules in an**
1324 **E16.5 mouse embryo sections, related to Figure 2.**
1325 **A.** Heatmap showing the Pearson correlation of module score for each
1326 spatial autocorrelation module and the expression of sets of specific
1327 genes for each cell type from a reported dataset (Cao et al., 2019).
1328 **B.** Spatial visualization of gene modules related to the indicated anatomical
1329 structures. Scale bar, 1 mm.
1330
1331 **Figure S14-S19. | Hotspot identified spatial regulatory modules in E10.5-**
1332 **E16.5 mouse embryo sections, related to Figure 3.**
1333 **A.** Heatmap showing the regulons with significant spatial autocorrelation
1334 (553, 554, 500, 380, 467 and 480 regulons, FDR < 0.05) grouped into 26,
1335 31, 25, 20, 28 and 27 regulon modules based on pairwise spatial
1336 correlations of regulon activity in the same embryo sections of **Figure 2A**
1337 from E10.5 to E16.5, respectively. Selected regulons related to
1338 representative modules and their corresponding GO terms are shown.
1339 **B.** Spatial visualization of the indicated regulon modules and their
1340 representative regulon for different anatomical structures. Scale bar, 1
1341 mm.
1342
1343 **Figure S20. Stereo-seq reconstructs the spatiotemporal gene regulatory**
1344 **network of the developing mouse brain, related to Figure 3.**

1345 **A.** Spatial visualization of the expression of the indicated genes representing
1346 neuroepithelium (left) and early neuroblasts in the E9.5 (right) brain.
1347 **B.** Spatial visualization of the indicated regulon activity in early neuroblasts
1348 of the E9.5 brain.
1349 **C.** Spatial visualization of the indicated regulon activity representing different
1350 anatomical structure of the E9.5 brain.
1351 **D.** GO analysis of target genes for transcription factors corresponding to
1352 different anatomical structures of the E9.5 brain as in **Figure 3F**.
1353 **E.** Heatmap showing the normalized regulon activity of top transcription
1354 factors corresponding to the subpallium, midbrain, and hindbrain
1355 development of mouse brain.
1356 **F.** Spatial visualization of the indicated regulon activity for the subpallium
1357 (DLX5), midbrain (DMBX1) and hindbrain (HOXA2). Scale bars, 500 μm.
1358
1359 **Figure S21. Characterization of morphogens expressed by secondary**
1360 **organizer centers in the developing mouse brain, related to Figure 3.**
1361 **A** and **B**. Spatial visualization of the indicated modules representing
1362 secondary organizer centers of the E9.5 and E12.5 brain.
1363 **C** and **D**. Heatmap showing the Spearman's correlation of ligands enriched in
1364 the secondary organizes centers of the E9.5 and E12.5 brain.
1365 **E**. The spatial scatter plots showing single DNB that captured the transcripts
1366 of the indicated morphogens at the ISO, ANR, ZLI, RP, and FP organizer
1367 centers at E9.5 (bottom left) and E12.5 (bottom right) embryos. Plots
1368 were superimposed with E9.5 or E12.5 embryo structures. Scale bar, 500
1369 μm.
1370
1371 **Figure S22. Schematic representation of morphogens and regulons at**
1372 **the indicated organizer centers, related to Figure 3.**
1373
1374 **Figure S23. Stereo-seq reconstructs the spatiotemporal gene regulatory**
1375 **networks of the developing mouse skeleton, related to Figure 3.**
1376 **A.** Unsupervised spatially-constrained clustering of the developing mouse
1377 skeleton based on regulon activity.
1378 **B.** Heatmap showing the normalized regulon activity score of the top

1379 transcription factors enriched in the indicated anatomical structures
1380 during mouse embryonic skeleton development.
1381 **C.** Spatial visualization of the activity of the indicated regulons for
1382 chondrocytes (SOX9) and osteoblasts (SP7).
1383 **D.** Spatial visualization of the expression of the indicated genes representing
1384 the early (*Col9a3*) and late (*Col22a1*) stages of ossification. Scale bar,
1385 500 μm.
1386
1387 **Figure S24. Stereo-seq reconstructs the developing mouse forebrain,**
1388 **related to Figure 4.**
1389 **A.** Heatmap showing the normalized expression of DEGs for the indicated
1390 anatomical structures of the E15.5 forebrain in **Figure 4A**.
1391 **B.** Spatial visualization of indicated genes representing different anatomical
1392 structures of the E15.5 forebrain. Scale bar, 500 μm.
1393 **C.** Spatial visualization of gene enrichment score of MGE, POA, LGE and
1394 Str. Genes related to each structure are labeled on the right side. MGE,
1395 medial ganglionic eminence; POA, preoptic area; LGE, lateral ganglionic
1396 eminence; Str, striatum. Scale bar, 500 μm.
1397
1398 **Figure S25. Rostral-caudal patterning of the CP, related to Figure 4.**
1399 **A.** Manual dissection of the CP based on spatial coordinates. Scale bar, 500
1400 μm.
1401 **B.** Heatmap showing the normalized expression of genes with rostral-caudal
1402 gradient.
1403 **C.** Spatial visualization of module score (left) representing the aggregated
1404 expression level of CP (rostral) specific gene set and representative
1405 genes (right). Scale bar, 500 μm.
1406 **D.** Spatial visualization of module score (left) representing the aggregated
1407 expression level of CP (caudal) specific gene set and representative
1408 genes (right). Scale bar, 500 μm.
1409
1410 **Figure S26. Mapping cell-type localization across forebrain, related to**
1411 **Figure 4.**
1412 **A.** Spatial visualization of cell proportion score representing different cell

1413 types. Scale bar, 500 μm.

1414 **B.** Violin plot showing the number of spliced and unspliced transcripts.

1415 **C.** Spatial visualization of the expression of indicated genes related to
1416 tangential migration of interneurons. Scale bar, 500 μm.

1417 **Figure S27. Mapping cell-type localization across neocortex**
1418 **development, related to Figure 4.**

1419 **A.** Unsupervised spatially-constrained clustering of the cortex from E11.5,
1420 E12.5, E13.5, 15.5, and E16.5 of mouse embryo.

1421 **B.** Spatial visualization of the cell proportion score across different stages of
1422 the mouse neocortex.

1423 **C.** Spatial visualization of representative genes for VZ, SVZ, IZ, CP, MarZ
1424 and meninges across different stages of the mouse neocortex.

1425 **D.** Spatial visualization of the cell cycle score across different stages of the
1426 mouse neocortex.

1427

1428 **Figure S28. Spatial mapping of genes associated with human**
1429 **developmental disorders in different mouse embryo stages, related to**
1430 **Figure 5.**

1431 Heatmap showing the normalized expression level of 1,940 genes selected
1432 from the Deciphering Developmental Disorders database in the indicated
1433 organs of E9.5 to E16.5 embryos.

1434

1435 **Table S1. Gene modules for each embryonic stage, related to Figure 2.**

1436

1437 **Table S2. Regulon modules for each embryonic stage, related to Figure**
1438 **3.**

1439

1440 **Table S3. Expression of genes related to the rostral-caudal gradient in**
1441 **the cortical plate, and genes related to the pseudotime of neuronal**
1442 **migration, related to Figure 4.**

1443

1444 **Table S4. Expression of genes related to monogenic diseases and**
1445 **autism, related to Figure 5.**

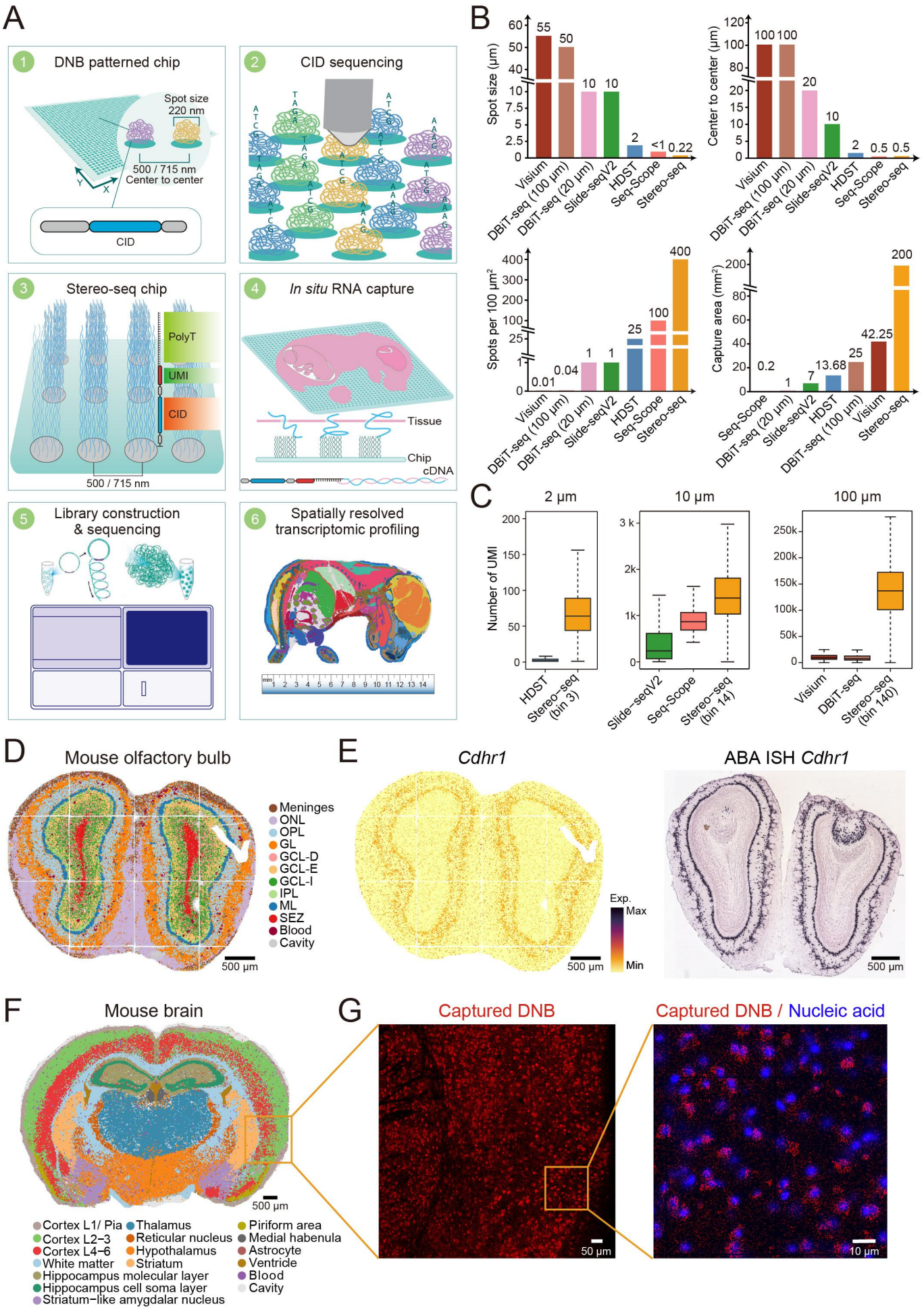
A
1 DNB patterned chip
Spot size 220 nm
500 / 715 nm Center to center
CID
2 CID sequencing
3 Stereo-seq chip
PolyT
UMI
CID
500 / 715 nm
4 In situ RNA capture
Tissue
Chip
cDNA
5 Library construction & sequencing
6 Spatially resolved transcriptomic profiling
B
Spot size (µm)
Center to center (µm)
Spots per 100 µm²
Capture area (mm²)
Visium
DBiT-seq (100 µm)
DBiT-seq (20 µm)
Slide-seqV2
HDST
Seq-Scope
Stereo-seq
C
2 µm
10 µm
100 µm
Number of UMI
HDST
Stereo-seq (bin 3)
Slide-seqV2
Seq-Scope
Stereo-seq (bin 14)
Visium
DBiT-seq
Stereo-seq (bin 140)
D
Mouse olfactory bulb
Meninges
ONL
OPL
GL
GCL-D
GCL-E
GCL-I
IPL
ML
SEZ
Blood
Cavity
500 µm
E
Cdhr1
ABA ISH Cdhr1
Exp.
Max
Min
500 µm
F
Mouse brain
500 µm
Cortex L1/ Pia
Cortex L2−3
Cortex L4−6
White matter
Hippocampus molecular layer
Hippocampus cell soma layer
Striatum−like amygdalar nucleus
Thalamus
Reticular nucleus
Hypothalamus
Striatum
Piriform area
Medial habenula
Astrocyte
Ventricle
Blood
Cavity
G
Captured DNB
Captured DNB / Nucleic acid
50 µm
10 µm

Figure 1

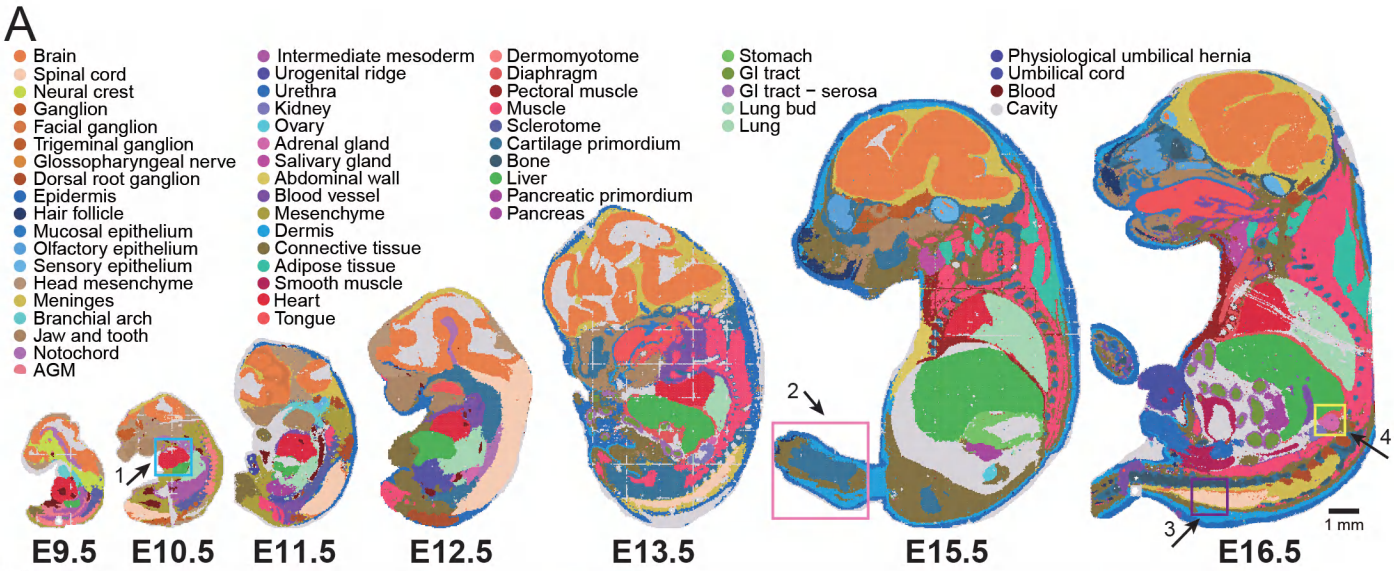
A
Brain
Spinal cord
Neural crest
Ganglion
Facial ganglion
Trigeminal ganglion
Glossopharyngeal nerve
Dorsal root ganglion
Epidermis
Hair follicle
Mucosal epithelium
Olfactory epithelium
Sensory epithelium
Head mesenchyme
Meninges
Branchial arch
Jaw and tooth
Notochord
AGM
Intermediate mesoderm
Urogenital ridge
Urethra
Kidney
Ovary
Adrenal gland
Salivary gland
Abdominal wall
Blood vessel
Mesenchyme
Dermis
Connective tissue
Adipose tissue
Smooth muscle
Heart
Tongue
Dermomyotome
Diaphragm
Pectoral muscle
Muscle
Sclerotome
Cartilage primordium
Bone
Liver
Pancreatic primordium
Pancreas
Stomach
GI tract
GI tract – serosa
Lung bud
Lung
Physiological umbilical hernia
Umbilical cord
Blood
Cavity
1
2
3
4
1 mm
E9.5
E10.5
E11.5
E12.5
E13.5
E15.5
E16.5

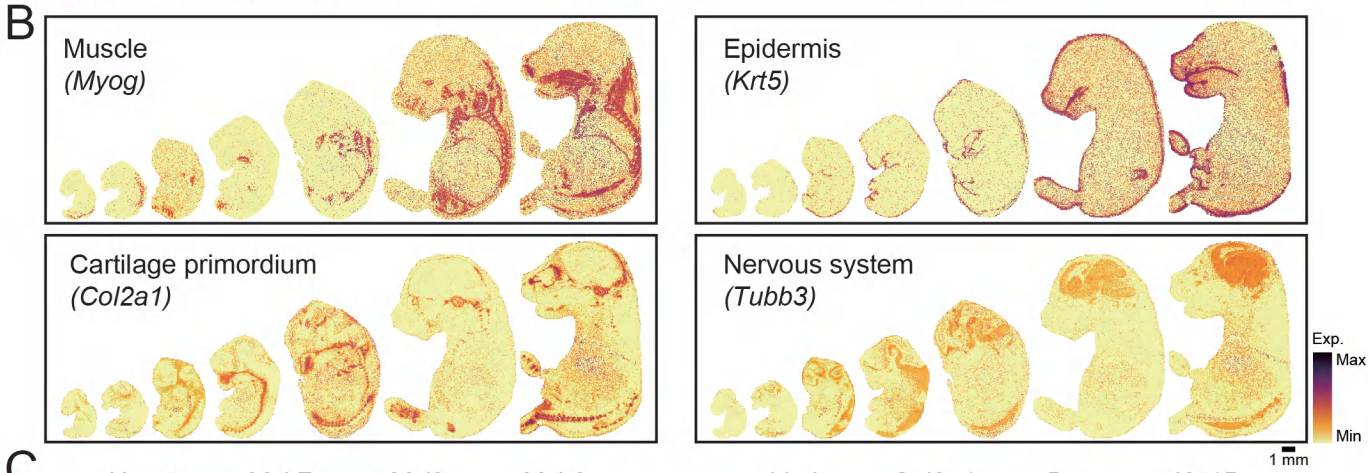
B
Muscle
(Myog)
Epidermis
(Krt5)
Cartilage primordium
(Col2a1)
Nervous system
(Tubb3)
Exp.
Max
Min
1 mm

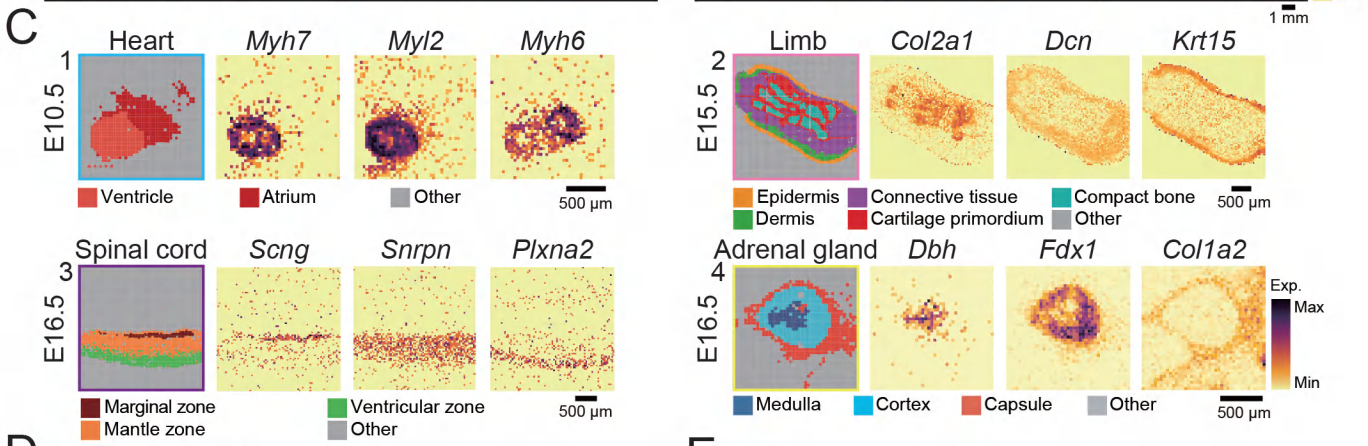
C
1
E10.5
Heart
Myh7
Myl2
Myh6
Ventricle
Atrium
Other
500 µm
2
E15.5
Limb
Col2a1
Dcn
Krt15
Epidermis
Connective tissue
Compact bone
Dermis
Cartilage primordium
Other
500 µm
3
E16.5
Spinal cord
Scng
Snrpn
Plxna2
Marginal zone
Mantle zone
Ventricular zone
Other
500 µm
4
E16.5
Adrenal gland
Dbh
Fdx1
Col1a2
Exp.
Max
Min
Medulla
Cortex
Capsule
Other
500 µm

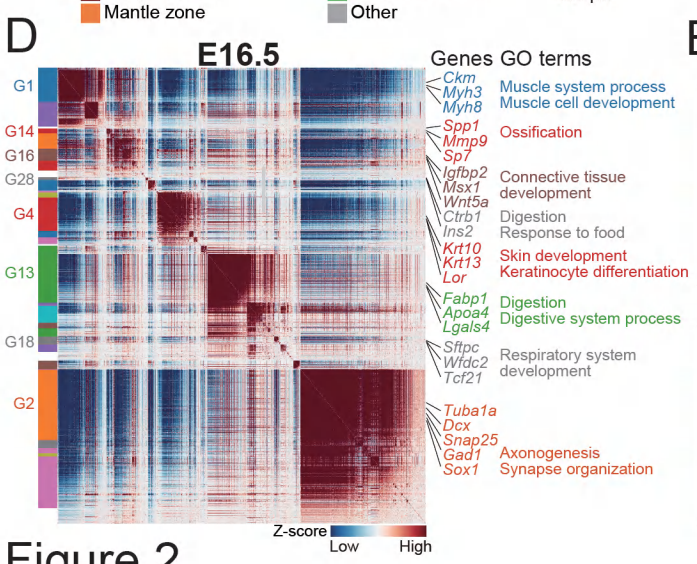
D
E16.5
G1
G14
G16
G28
G4
G13
G18
G2
Genes
GO terms
Ckm
Myh3
Myh8
Muscle system process
Muscle cell development
Spp1
Mmp9
Sp7
Ossification
Igfbp2
Msx1
Wnt5a
Connective tissue development
Ctrb1
Ins2
Digestion
Response to food
Krt10
Krt13
Lor
Skin development
Keratinocyte differentiation
Fabp1
Apoa4
Lgals4
Digestion
Digestive system process
Sftpc
Wfdc2
Tcf21
Respiratory system development
Tuba1a
Dcx
Snap25
Gad1
Sox1
Axonogenesis
Synapse organization
Z-score
Low
High

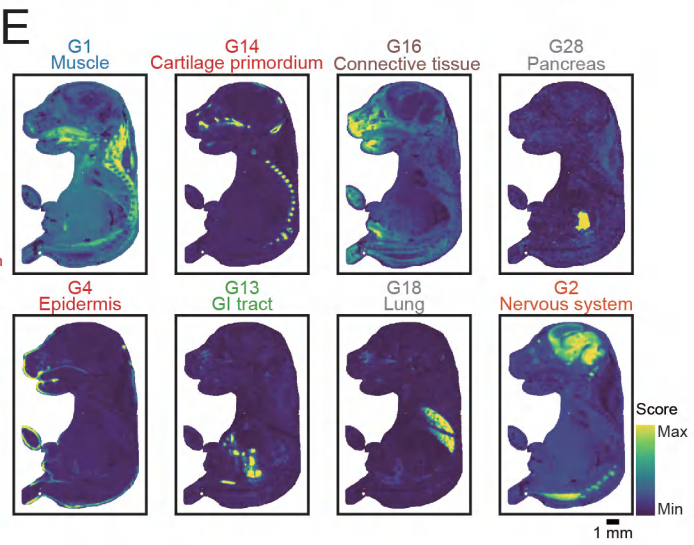
E
G1
Muscle
G14
Cartilage primordium
G16
Connective tissue
G28
Pancreas
G4
Epidermis
G13
GI tract
G18
Lung
G2
Nervous system
Score
Max
Min
1 mm

Figure 2

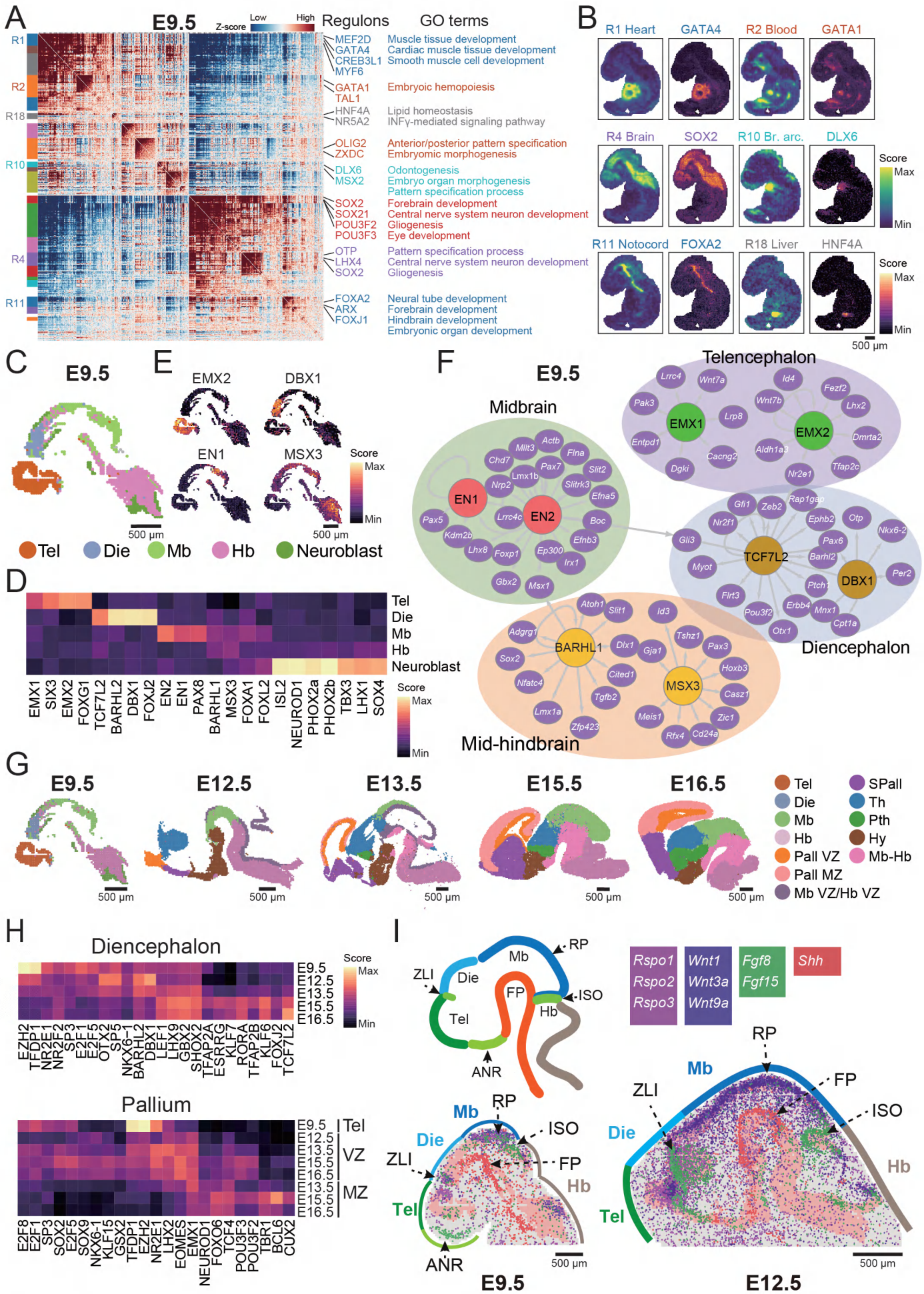
A
E9.5
Z-score
Low
High
Regulons
GO terms
R1
R2
R18
R10
R4
R11
MEF2D
GATA4
CREB3L1
MYF6
Muscle tissue development
Cardiac muscle tissue development
Smooth muscle cell development
GATA1
TAL1
Embryoic hemopoiesis
HNF4A
NR5A2
Lipid homeostasis
INFγ-mediated signaling pathway
OLIG2
ZXDC
Anterior/posterior pattern specification
Embryomic morphogenesis
DLX6
MSX2
Odontogenesis
Embryo organ morphogenesis
Pattern specification process
SOX2
SOX21
POU3F2
POU3F3
Forebrain development
Central nerve system neuron development
Gliogenesis
Eye development
OTP
LHX4
SOX2
Pattern specification process
Central nerve system neuron development
Gliogenesis
FOXA2
ARX
FOXJ1
Neural tube development
Forebrain development
Hindbrain development
Embryonic organ development
B
R1 Heart
GATA4
R2 Blood
GATA1
R4 Brain
SOX2
R10 Br. arc.
DLX6
R11 Notocord
FOXA2
R18 Liver
HNF4A
Score
Max
Min
500 µm
C
E9.5
500 µm
Tel
Die
Mb
Hb
Neuroblast
E
EMX2
DBX1
EN1
MSX3
Score
Max
Min
500 µm
D
Tel
Die
Mb
Hb
Neuroblast
EMX1
SIX3
EMX2
FOXG1
TCF7L2
BARHL2
DBX1
FOXJ2
EN2
EN1
PAX8
BARHL1
MSX3
FOXA1
FOXL2
ISL2
NEUROD1
PHOX2a
PHOX2b
TBX3
LHX1
SOX4
Score
Max
Min
F
E9.5
Telencephalon
Midbrain
EMX1
EMX2
EN1
EN2
TCF7L2
DBX1
BARHL1
MSX3
Diencephalon
Mid-hindbrain
G
E9.5
E12.5
E13.5
E15.5
E16.5
500 µm
Tel
Die
Mb
Hb
Pall VZ
Pall MZ
Mb VZ/Hb VZ
SPall
Th
Pth
Hy
Mb-Hb
H
Diencephalon
E9.5
E12.5
E13.5
E15.5
E16.5
Score
Max
Min
EZH2
TFDP1
NR2E1
NR2F2
SP3
E2F5
E2F1
OTX2
SP5
NKX6-1
BARHL2
DBX1
LEF1
LHX9
GBX2
SHOX2
TFAP2A
ESRRG
KLF7
RORA
TFAP2B
KLF6
FOXJ2
TCF7L2
Pallium
Tel
VZ
MZ
E2F8
E2F1
SP3
SOX2
E2F5
SOX9
NKX6-1
KLF15
GSX2
TFDP1
EZH2
NR2E1
LHX2
EOMES
EMX1
NEUROD1
FOXO6
TCF4
POU3F3
POU3F2
TBR1
BCL6
CUX2
I
RP
Mb
ZLI
Die
FP
ISO
Tel
Hb
ANR
Rspo1
Rspo2
Rspo3
Wnt1
Wnt3a
Wnt9a
Fgf8
Fgf15
Shh
500 µm
E9.5
E12.5

Figure 3

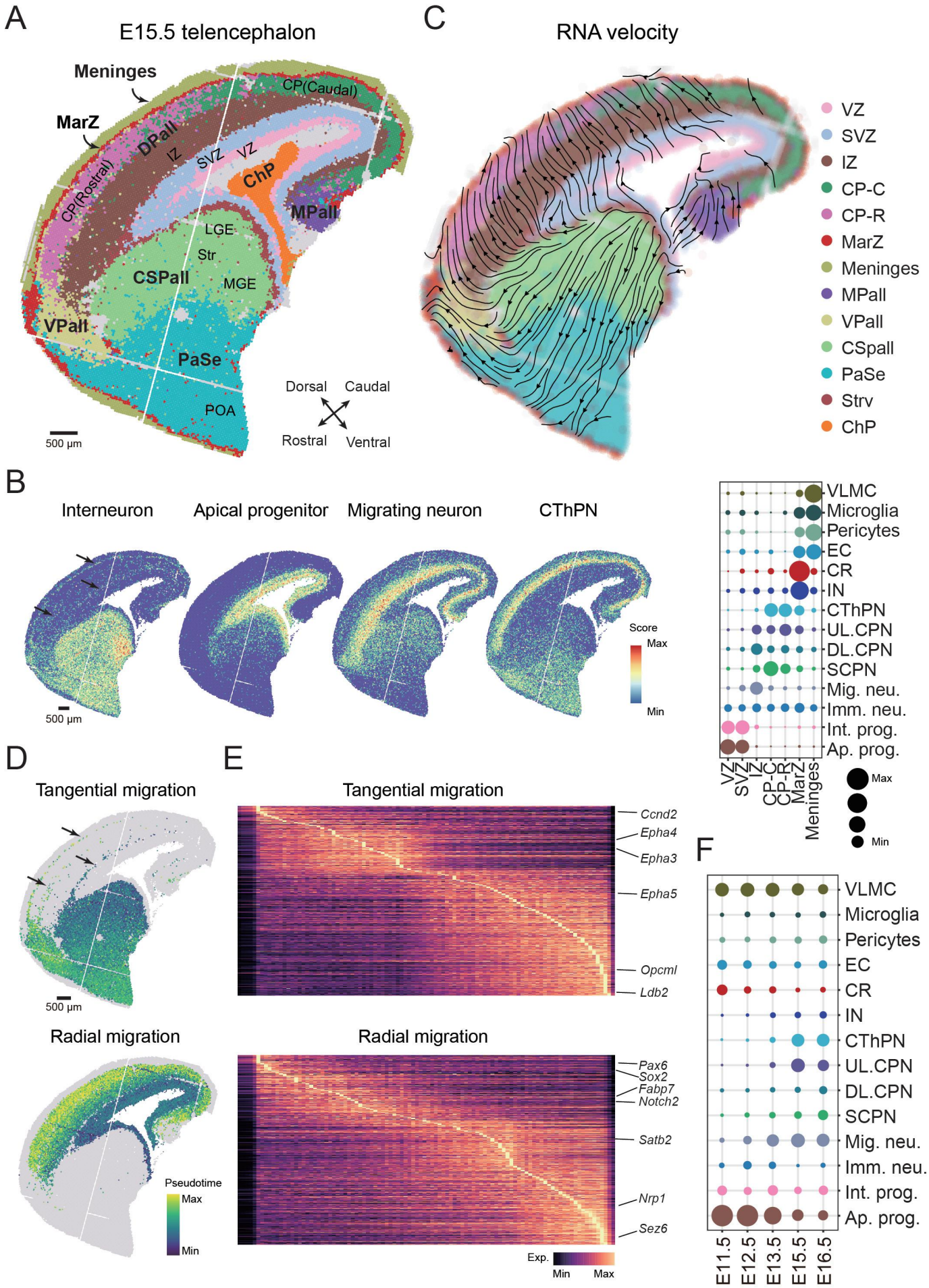
A
E15.5 telencephalon
Meninges
MarZ
CP(Caudal)
DPall
IZ
SVZ
VZ
ChP
CP(Rostral)
MPall
LGE
Str
CSPall
MGE
VPall
PaSe
POA
500 µm
Dorsal
Caudal
Rostral
Ventral
C
RNA velocity
VZ
SVZ
IZ
CP-C
CP-R
MarZ
Meninges
MPall
VPall
CSpall
PaSe
Strv
ChP
B
Interneuron
Apical progenitor
Migrating neuron
CThPN
Score
Max
Min
500 µm
VLMC
Microglia
Pericytes
EC
CR
IN
CThPN
UL.CPN
DL.CPN
SCPN
Mig. neu.
Imm. neu.
Int. prog.
Ap. prog.
VZ
SVZ
IZ
CP-C
CP-R
MarZ
Meninges
Max
Min
D
Tangential migration
500 µm
Radial migration
Pseudotime
Max
Min
E
Tangential migration
Ccnd2
Epha4
Epha3
Epha5
Opcml
Ldb2
Radial migration
Pax6
Sox2
Fabp7
Notch2
Satb2
Nrp1
Sez6
Exp.
Min
Max
F
VLMC
Microglia
Pericytes
EC
CR
IN
CThPN
UL.CPN
DL.CPN
SCPN
Mig. neu.
Imm. neu.
Int. prog.
Ap. prog.
E11.5
E12.5
E13.5
E15.5
E16.5

Figure 4

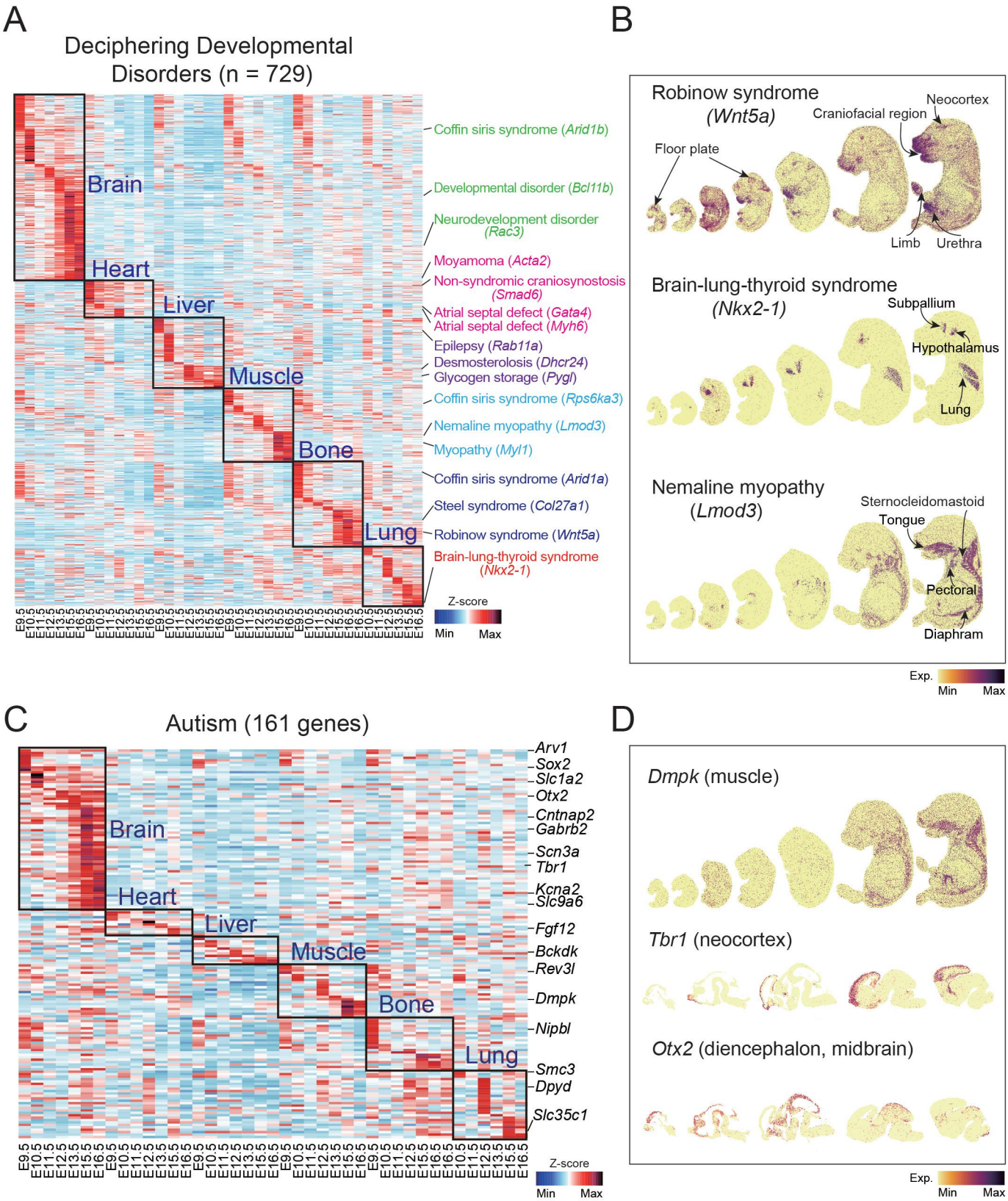
A
Deciphering Developmental Disorders (n = 729)
Brain
Heart
Liver
Muscle
Bone
Lung
Coffin siris syndrome (Arid1b)
Developmental disorder (Bcl11b)
Neurodevelopment disorder (Rac3)
Moyamoma (Acta2)
Non-syndromic craniosynostosis (Smad6)
Atrial septal defect (Gata4)
Atrial septal defect (Myh6)
Epilepsy (Rab11a)
Desmosterolosis (Dhcr24)
Glycogen storage (Pygl)
Coffin siris syndrome (Rps6ka3)
Nemaline myopathy (Lmod3)
Myopathy (Myl1)
Coffin siris syndrome (Arid1a)
Steel syndrome (Col27a1)
Robinow syndrome (Wnt5a)
Brain-lung-thyroid syndrome (Nkx2-1)
Z-score
Min
Max
B
Robinow syndrome (Wnt5a)
Neocortex
Craniofacial region
Floor plate
Limb
Urethra
Brain-lung-thyroid syndrome (Nkx2-1)
Subpallium
Hypothalamus
Lung
Nemaline myopathy (Lmod3)
Sternocleidomastoid
Tongue
Pectoral
Diaphram
Exp.
Min
Max
C
Autism (161 genes)
Arv1
Sox2
Slc1a2
Otx2
Cntnap2
Gabrb2
Scn3a
Tbr1
Kcna2
Slc9a6
Fgf12
Bckdk
Rev3l
Dmpk
Nipbl
Smc3
Dpyd
Slc35c1
Z-score
Min
Max
D
Dmpk (muscle)
Tbr1 (neocortex)
Otx2 (diencephalon, midbrain)
Exp.
Min
Max

Figure 5

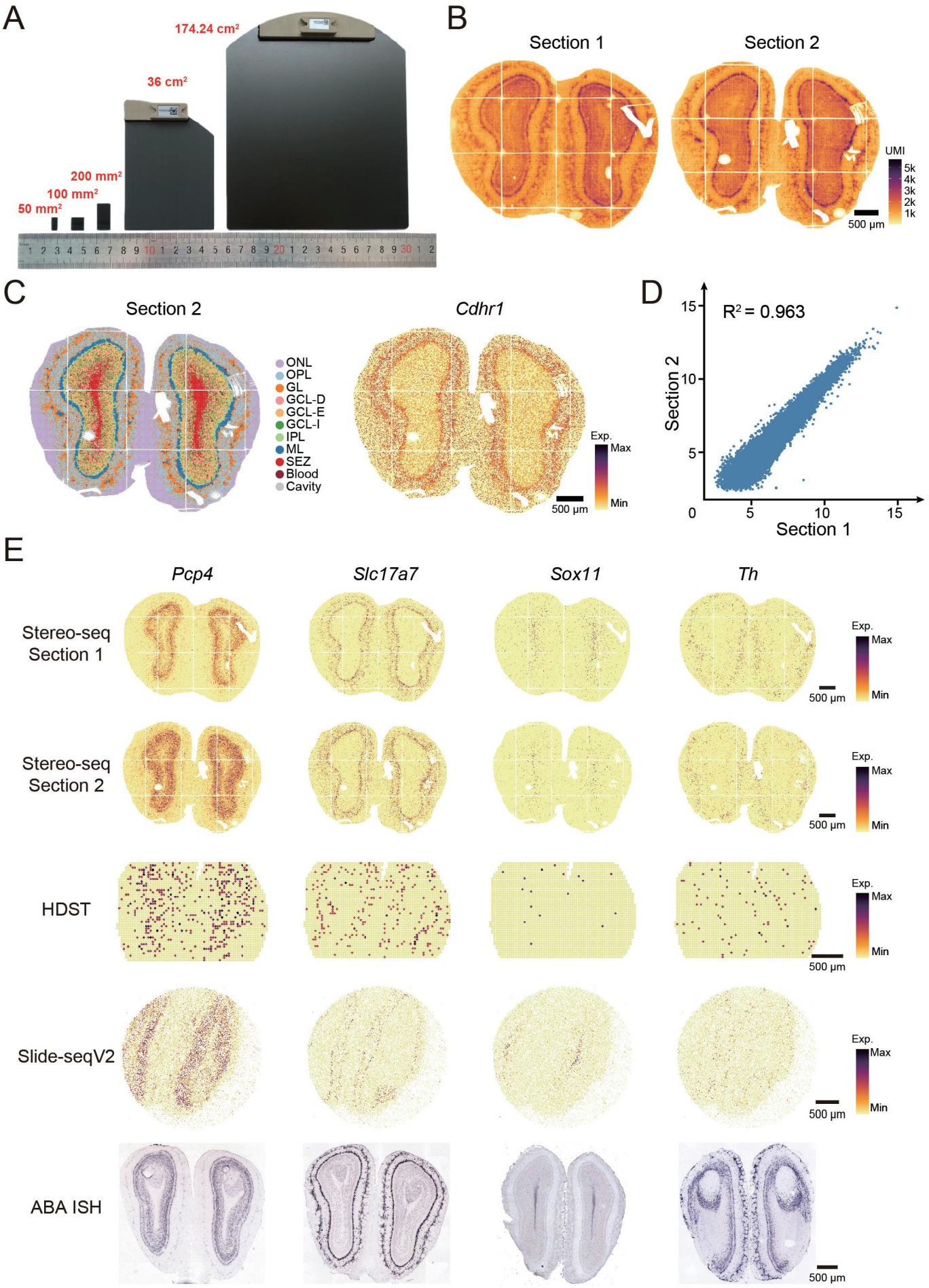
A
174.24 cm²
36 cm²
200 mm²
100 mm²
50 mm²
B
Section 1
Section 2
UMI
5k
4k
3k
2k
1k
500 μm
C
Section 2
ONL
OPL
GL
GCL-D
GCL-E
GCL-I
IPL
ML
SEZ
Blood
Cavity
Cdhr1
Exp.
Max
Min
500 μm
D
R² = 0.963
Section 2
Section 1
E
Pcp4
Slc17a7
Sox11
Th
Stereo-seq Section 1
Stereo-seq Section 2
HDST
Slide-seqV2
ABA ISH
Exp.
Max
Min
500 μm

Figure S1

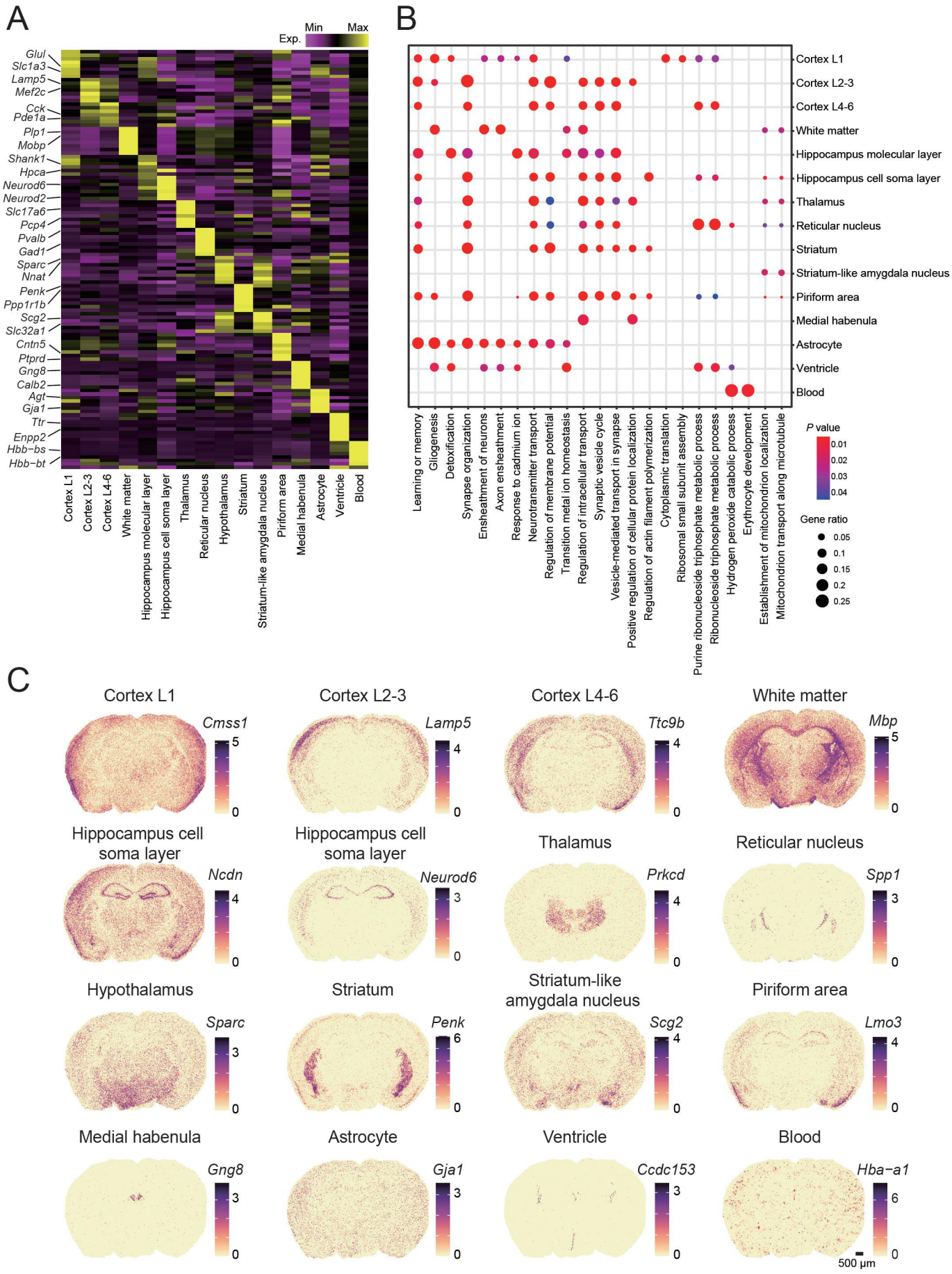
A
Min
Max
Exp.
Glul
Slc1a3
Lamp5
Mef2c
Cck
Pde1a
Plp1
Mobp
Shank1
Hpca
Neurod6
Neurod2
Slc17a6
Pcp4
Pvalb
Gad1
Sparc
Nnat
Penk
Ppp1r1b
Scg2
Slc32a1
Cntn5
Ptprd
Gng8
Calb2
Agt
Gja1
Ttr
Enpp2
Hbb-bs
Hbb-bt
Cortex L1
Cortex L2-3
Cortex L4-6
White matter
Hippocampus molecular layer
Hippocampus cell soma layer
Thalamus
Reticular nucleus
Hypothalamus
Striatum
Striatum-like amygdala nucleus
Piriform area
Medial habenula
Astrocyte
Ventricle
Blood
B
Learning or memory
Gliogenesis
Detoxification
Synapse organization
Ensheathment of neurons
Axon ensheathment
Response to cadmium ion
Neurotransmitter transport
Regulation of membrane potential
Transition metal ion homeostasis
Regulation of intracellular transport
Synaptic vesicle cycle
Vesicle-mediated transport in synapse
Positive regulation of cellular protein localization
Regulation of actin filament polymerization
Cytoplasmic translation
Ribosomal small subunit assembly
Purine ribonucleoside triphosphate metabolic process
Ribonucleoside triphosphate metabolic process
Hydrogen peroxide catabolic process
Erythrocyte development
Establishment of mitochondrion localization
Mitochondrion transport along microtubule
P value
0.01
0.02
0.03
0.04
Gene ratio
0.05
0.1
0.15
0.2
0.25
C
Cortex L1
Cmss1
Cortex L2-3
Lamp5
Cortex L4-6
Ttc9b
White matter
Mbp
Hippocampus cell soma layer
Ncdn
Hippocampus cell soma layer
Neurod6
Thalamus
Prkcd
Reticular nucleus
Spp1
Hypothalamus
Sparc
Striatum
Penk
Striatum-like amygdala nucleus
Scg2
Piriform area
Lmo3
Medial habenula
Gng8
Astrocyte
Gja1
Ventricle
Ccdc153
Blood
Hba-a1
500 μm

Figure S2

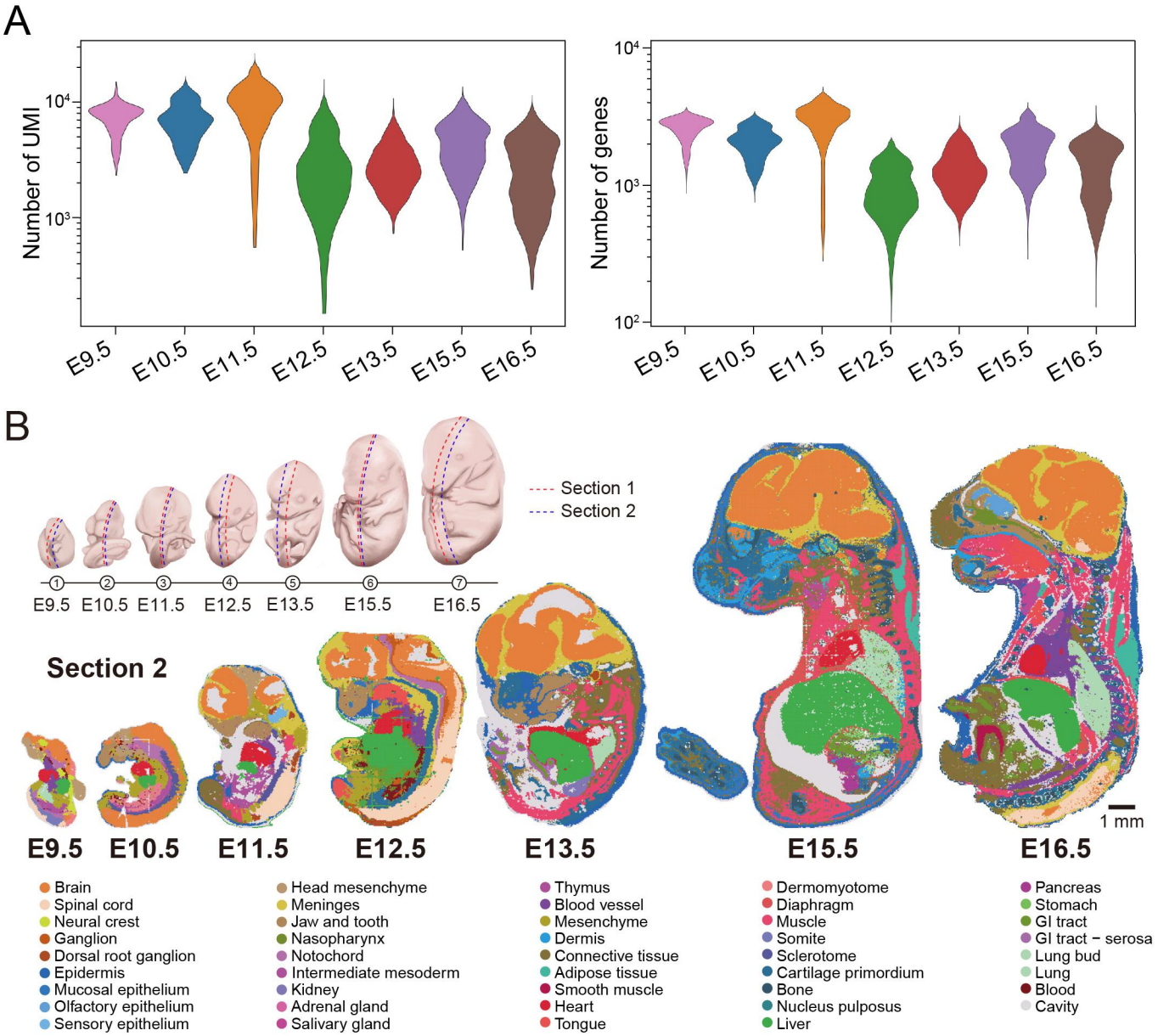
A
Number of UMI
Number of genes
E9.5
E10.5
E11.5
E12.5
E13.5
E15.5
E16.5
B
Section 1
Section 2
Section 2
1 mm
Brain
Spinal cord
Neural crest
Ganglion
Dorsal root ganglion
Epidermis
Mucosal epithelium
Olfactory epithelium
Sensory epithelium
Head mesenchyme
Meninges
Jaw and tooth
Nasopharynx
Notochord
Intermediate mesoderm
Kidney
Adrenal gland
Salivary gland
Thymus
Blood vessel
Mesenchyme
Dermis
Connective tissue
Adipose tissue
Smooth muscle
Heart
Tongue
Dermomyotome
Diaphragm
Muscle
Somite
Sclerotome
Cartilage primordium
Bone
Nucleus pulposus
Liver
Pancreas
Stomach
GI tract
GI tract – serosa
Lung bud
Lung
Blood
Cavity
C
Section 1
Section 2
1 mm

Figure S3

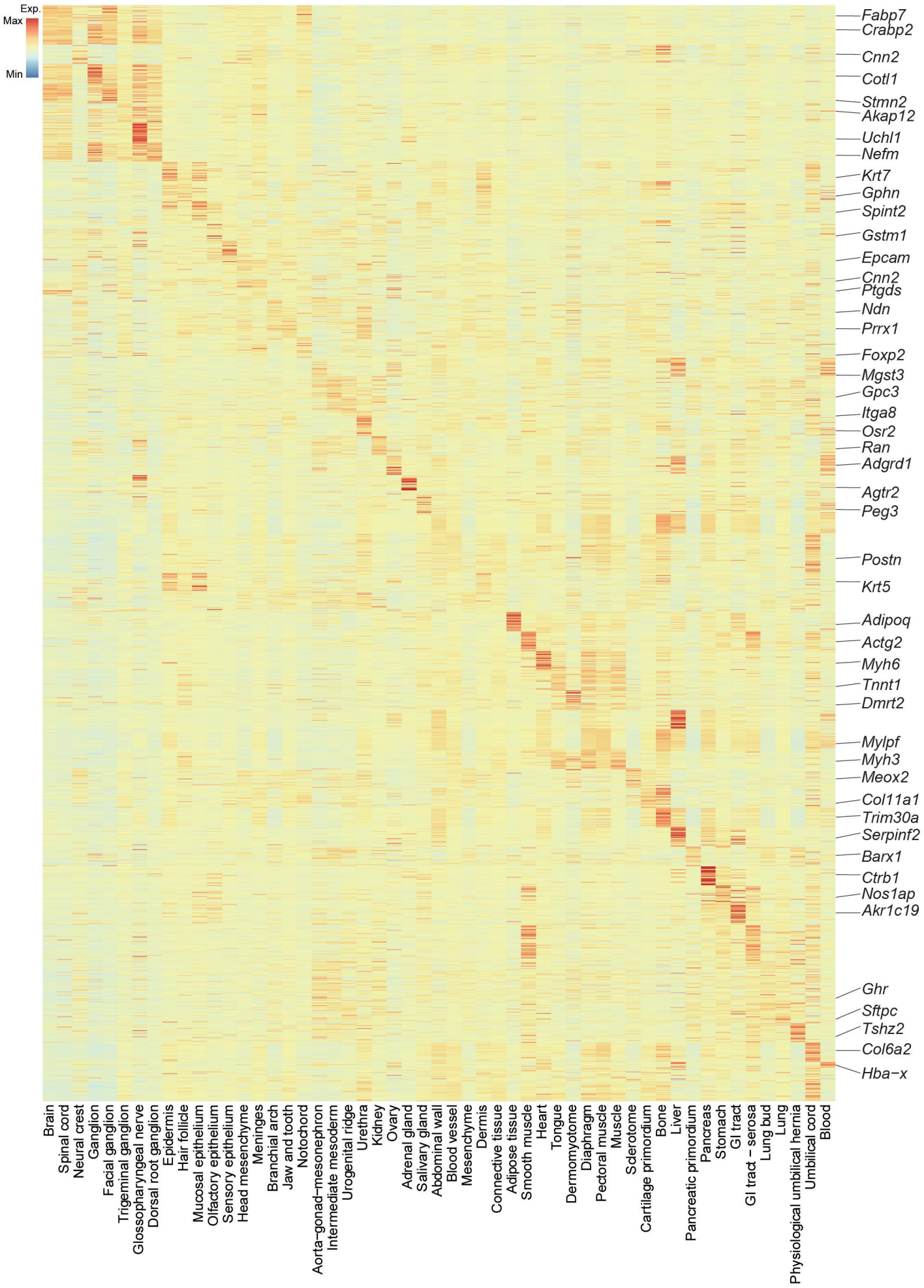
Exp.
Max
Min
Fabp7
Crabp2
Cnn2
Cotl1
Stmn2
Akap12
Uchl1
Nefm
Krt7
Gphn
Spint2
Gstm1
Epcam
Cnn2
Ptgds
Ndn
Prrx1
Foxp2
Mgst3
Gpc3
Itga8
Osr2
Ran
Adgrd1
Agtr2
Peg3
Postn
Krt5
Adipoq
Actg2
Myh6
Tnnt1
Dmrt2
Mylpf
Myh3
Meox2
Col11a1
Trim30a
Serpinf2
Barx1
Ctrb1
Nos1ap
Akr1c19
Ghr
Sftpc
Tshz2
Col6a2
Hba−x
Brain
Spinal cord
Neural crest
Ganglion
Facial ganglion
Trigeminal ganglion
Glossopharyngeal nerve
Dorsal root ganglion
Epidermis
Hair follicle
Mucosal epithelium
Olfactory epithelium
Sensory epithelium
Head mesenchyme
Meninges
Branchial arch
Jaw and tooth
Notochord
Aorta−gonad−mesonephron
Intermediate mesoderm
Urogenital ridge
Urethra
Kidney
Ovary
Adrenal gland
Salivary gland
Abdominal wall
Blood vessel
Mesenchyme
Dermis
Connective tissue
Adipose tissue
Smooth muscle
Heart
Tongue
Dermomyotome
Diaphragm
Pectoral muscle
Muscle
Sclerotome
Cartilage primordium
Bone
Liver
Pancreatic primordium
Pancreas
Stomach
GI tract
GI tract − serosa
Lung bud
Lung
Physiological umbilical hernia
Umbilical cord
Blood

Figure S4

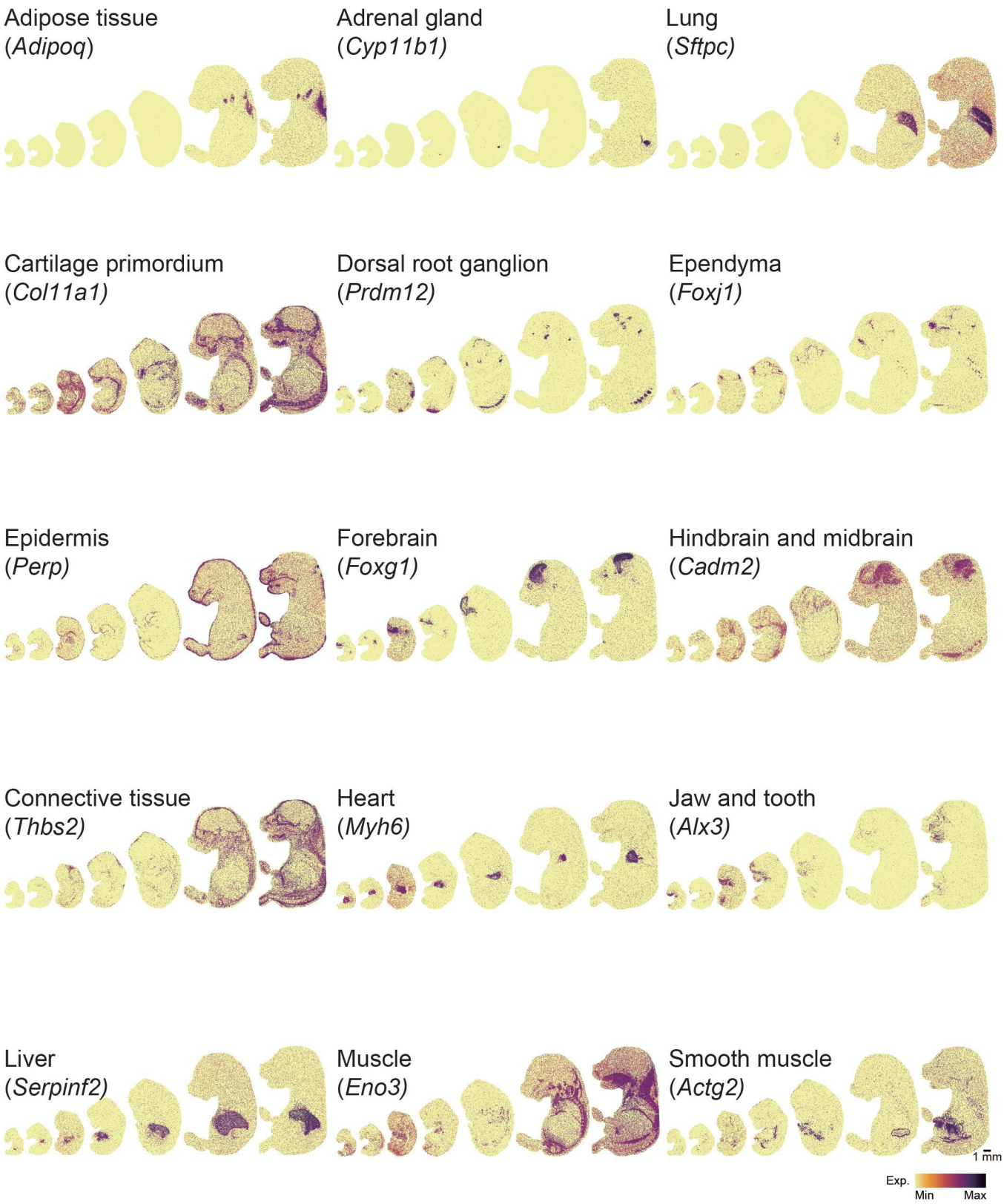
Adipose tissue
(Adipoq)
Adrenal gland
(Cyp11b1)
Lung
(Sftpc)
Cartilage primordium
(Col11a1)
Dorsal root ganglion
(Prdm12)
Ependyma
(Foxj1)
Epidermis
(Perp)
Forebrain
(Foxg1)
Hindbrain and midbrain
(Cadm2)
Connective tissue
(Thbs2)
Heart
(Myh6)
Jaw and tooth
(Alx3)
Liver
(Serpinf2)
Muscle
(Eno3)
Smooth muscle
(Actg2)
1 mm
Exp.
Min
Max

Figure S5

A

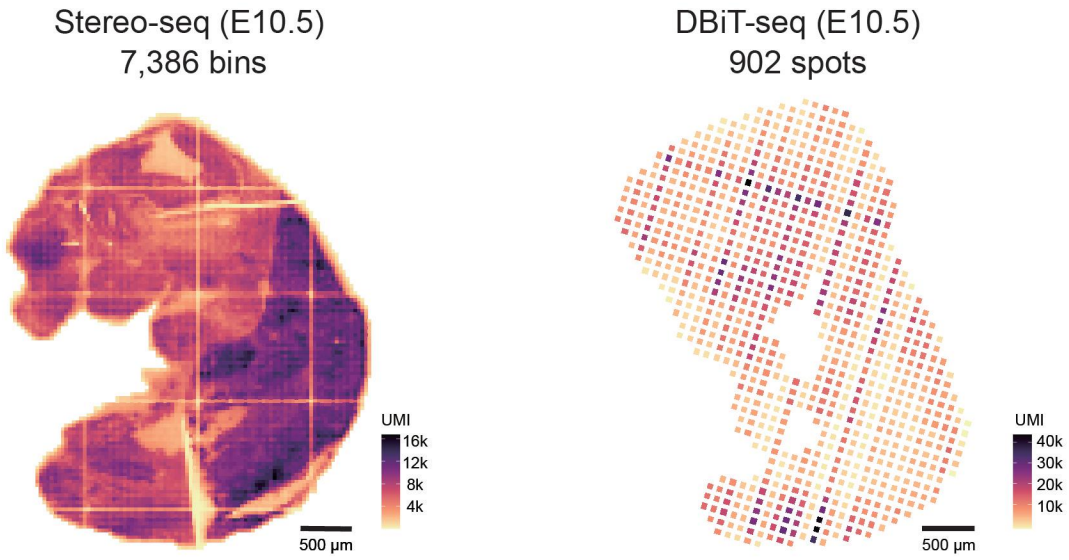
Stereo-seq (E10.5)
7,386 bins
UMI
16k
12k
8k
4k
500 µm
DBiT-seq (E10.5)
902 spots
UMI
40k
30k
20k
10k
500 µm

B

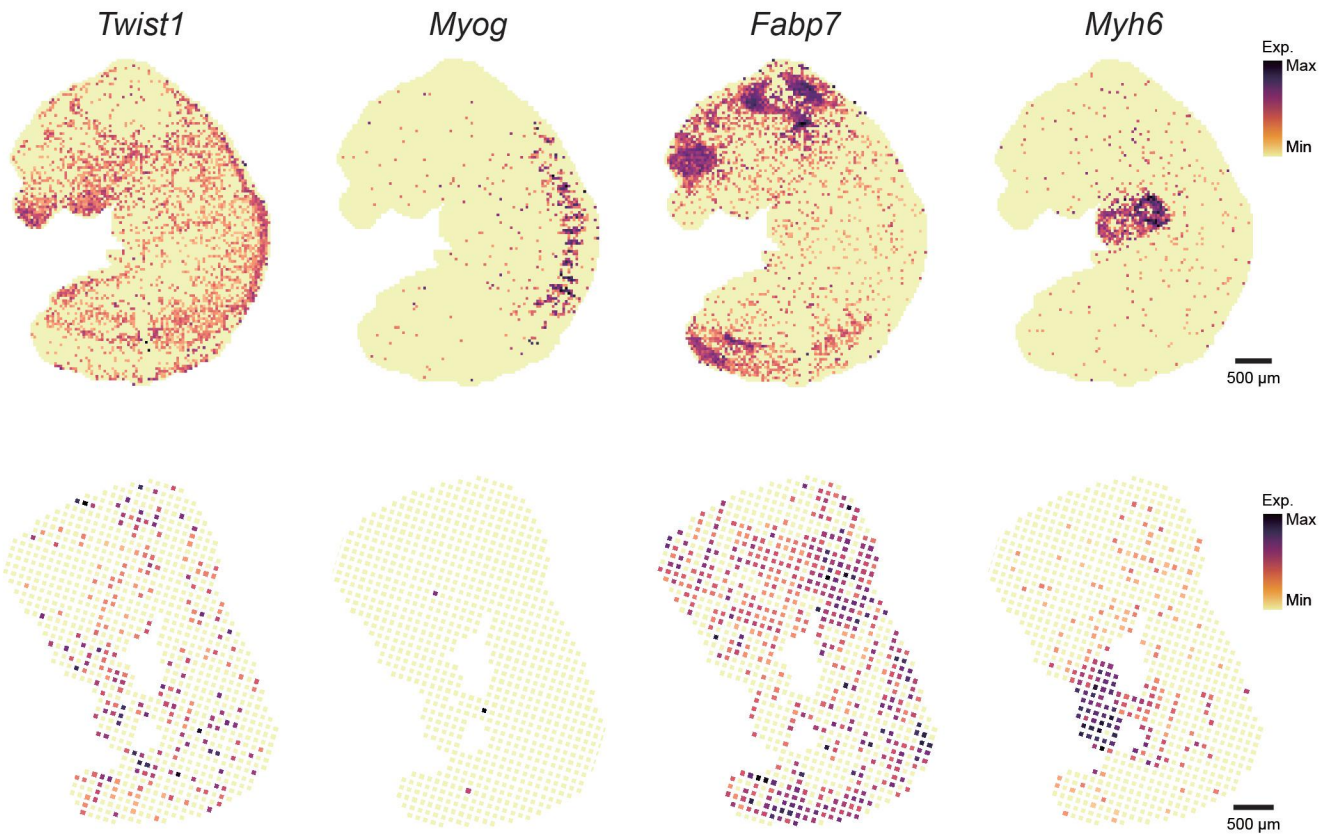
Twist1
Myog
Fabp7
Myh6
Exp.
Max
Min
500 µm
Exp.
Max
Min
500 µm

Figure S6

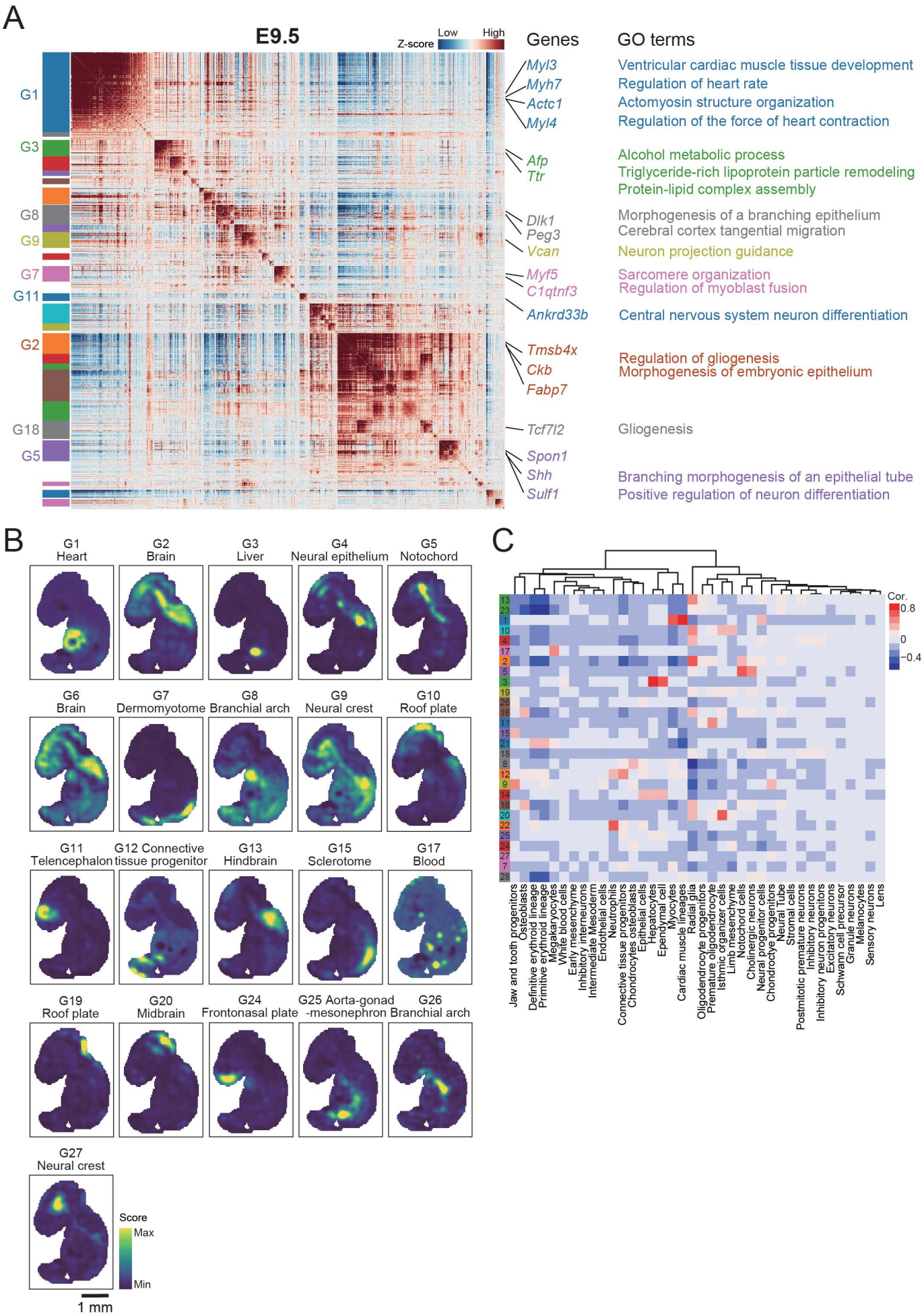
A
E9.5
Z-score
Low
High
Genes
GO terms
G1
G3
G8
G9
G7
G11
G2
G18
G5
Myl3
Myh7
Actc1
Myl4
Ventricular cardiac muscle tissue development
Regulation of heart rate
Actomyosin structure organization
Regulation of the force of heart contraction
Afp
Ttr
Alcohol metabolic process
Triglyceride-rich lipoprotein particle remodeling
Protein-lipid complex assembly
Dlk1
Peg3
Vcan
Morphogenesis of a branching epithelium
Cerebral cortex tangential migration
Neuron projection guidance
Myf5
C1qtnf3
Sarcomere organization
Regulation of myoblast fusion
Ankrd33b
Central nervous system neuron differentiation
Tmsb4x
Ckb
Fabp7
Regulation of gliogenesis
Morphogenesis of embryonic epithelium
Tcf7l2
Gliogenesis
Spon1
Shh
Sulf1
Branching morphogenesis of an epithelial tube
Positive regulation of neuron differentiation
B
G1 Heart
G2 Brain
G3 Liver
G4 Neural epithelium
G5 Notochord
G6 Brain
G7 Dermomyotome
G8 Branchial arch
G9 Neural crest
G10 Roof plate
G11 Telencephalon
G12 Connective tissue progenitor
G13 Hindbrain
G15 Sclerotome
G17 Blood
G19 Roof plate
G20 Midbrain
G24 Frontonasal plate
G25 Aorta-gonad -mesonephron
G26 Branchial arch
G27 Neural crest
Score
Max
Min
1 mm
C
Cor.
0.8
0
−0.4
Jaw and tooth progenitors
Osteoblasts
Definitive erythroid lineage
Primitive erythroid lineage
Megakaryocytes
White blood cells
Early mesenchyme
Inhibitory interneurons
Intermediate Mesoderm
Endothelial cells
Neutrophils
Connective tissue progenitors
Chondrocytes osteoblasts
Epithelial cells
Hepatocytes
Ependymal cell
Myocytes
Cardiac muscle lineages
Radial glia
Oligodendrocyte progenitors
Premature oligodendrocyte
Isthmic organizer cells
Limb mesenchyme
Notochord cells
Cholinergic neurons
Neural progenitor cells
Chondroctye progenitors
Neural Tube
Stromal cells
Postmitotic premature neurons
Inhibitory neurons
Inhibitory neuron progenitors
Excitatory neurons
Schwann cell precursor
Granule neurons
Melanocytes
Sensory neurons
Lens

Figure S7

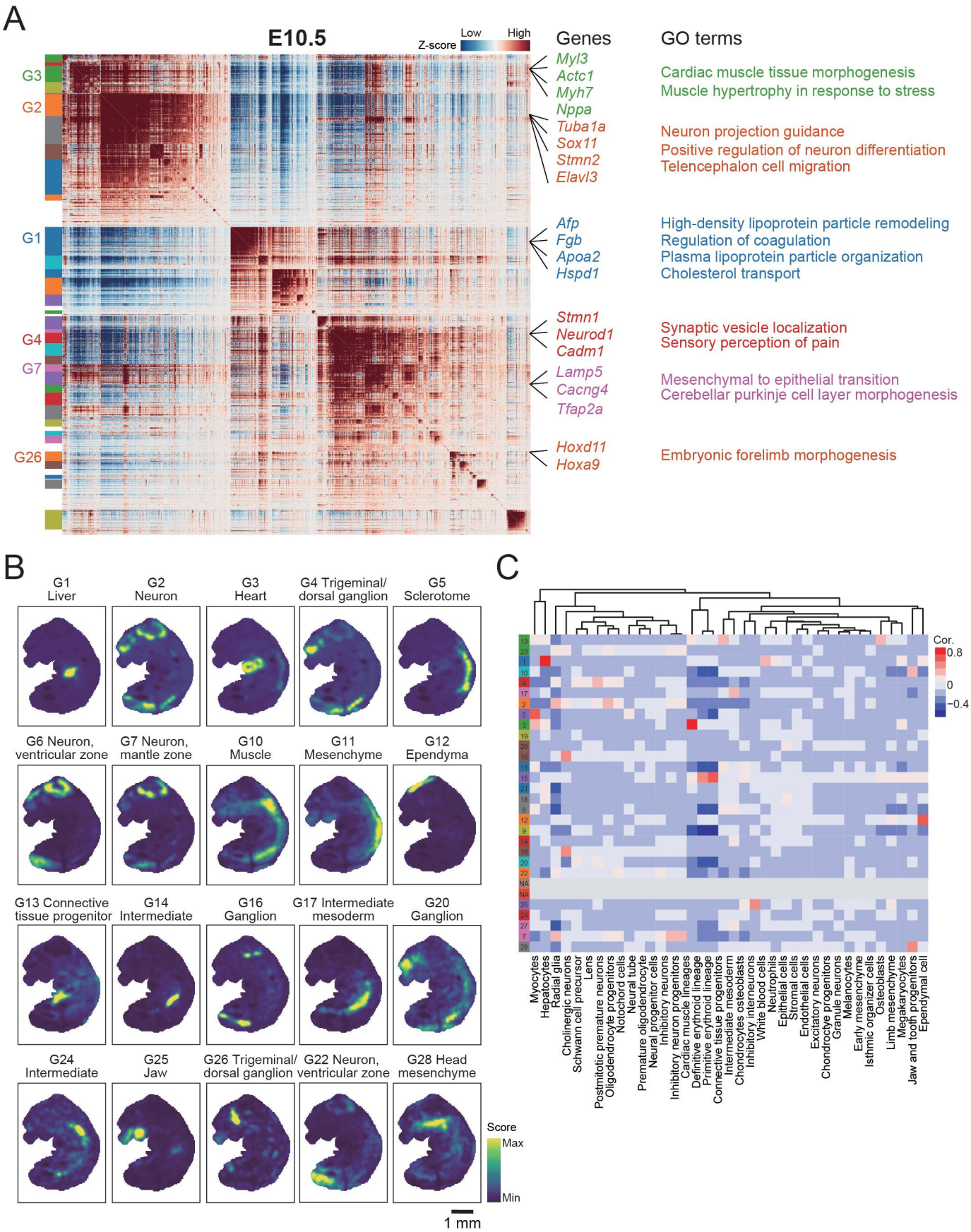
A
E10.5
Z-score
Low
High
Genes
GO terms
G3
G2
G1
G4
G7
G26
Myl3
Actc1
Myh7
Nppa
Tuba1a
Sox11
Stmn2
Elavl3
Afp
Fgb
Apoa2
Hspd1
Stmn1
Neurod1
Cadm1
Lamp5
Cacng4
Tfap2a
Hoxd11
Hoxa9
Cardiac muscle tissue morphogenesis
Muscle hypertrophy in response to stress
Neuron projection guidance
Positive regulation of neuron differentiation
Telencephalon cell migration
High-density lipoprotein particle remodeling
Regulation of coagulation
Plasma lipoprotein particle organization
Cholesterol transport
Synaptic vesicle localization
Sensory perception of pain
Mesenchymal to epithelial transition
Cerebellar purkinje cell layer morphogenesis
Embryonic forelimb morphogenesis
B
G1 Liver
G2 Neuron
G3 Heart
G4 Trigeminal/ dorsal ganglion
G5 Sclerotome
G6 Neuron, ventricular zone
G7 Neuron, mantle zone
G10 Muscle
G11 Mesenchyme
G12 Ependyma
G13 Connective tissue progenitor
G14 Intermediate
G16 Ganglion
G17 Intermediate mesoderm
G20 Ganglion
G24 Intermediate
G25 Jaw
G26 Trigeminal/ dorsal ganglion
G22 Neuron, ventricular zone
G28 Head mesenchyme
Score
Max
Min
1 mm
C
Cor.
0.8
0
−0.4
Myocytes
Hepatocytes
Radial glia
Cholinergic neurons
Schwann cell precursor
Lens
Postmitotic premature neurons
Oligodendrocyte progenitors
Notochord cells
Neural tube
Premature oligodendrocyte
Neural progenitor cells
Inhibitory neurons
Inhibitory neuron progenitors
Cardiac muscle lineages
Definitive erythroid lineage
Primitive erythroid lineage
Connective tissue progenitors
Intermediate mesoderm
Chondrocytes osteoblasts
Inhibitory interneurons
White blood cells
Neutrophils
Epithelial cells
Stromal cells
Endothelial cells
Excitatory neurons
Chondrocytes progenitors
Granule neurons
Melanocytes
Early mesenchyme
Isthmic organizer cells
Osteoblasts
Limb mesenchyme
Megakaryocytes
Jaw and tooth progenitors
Ependymal cell

Figure S8

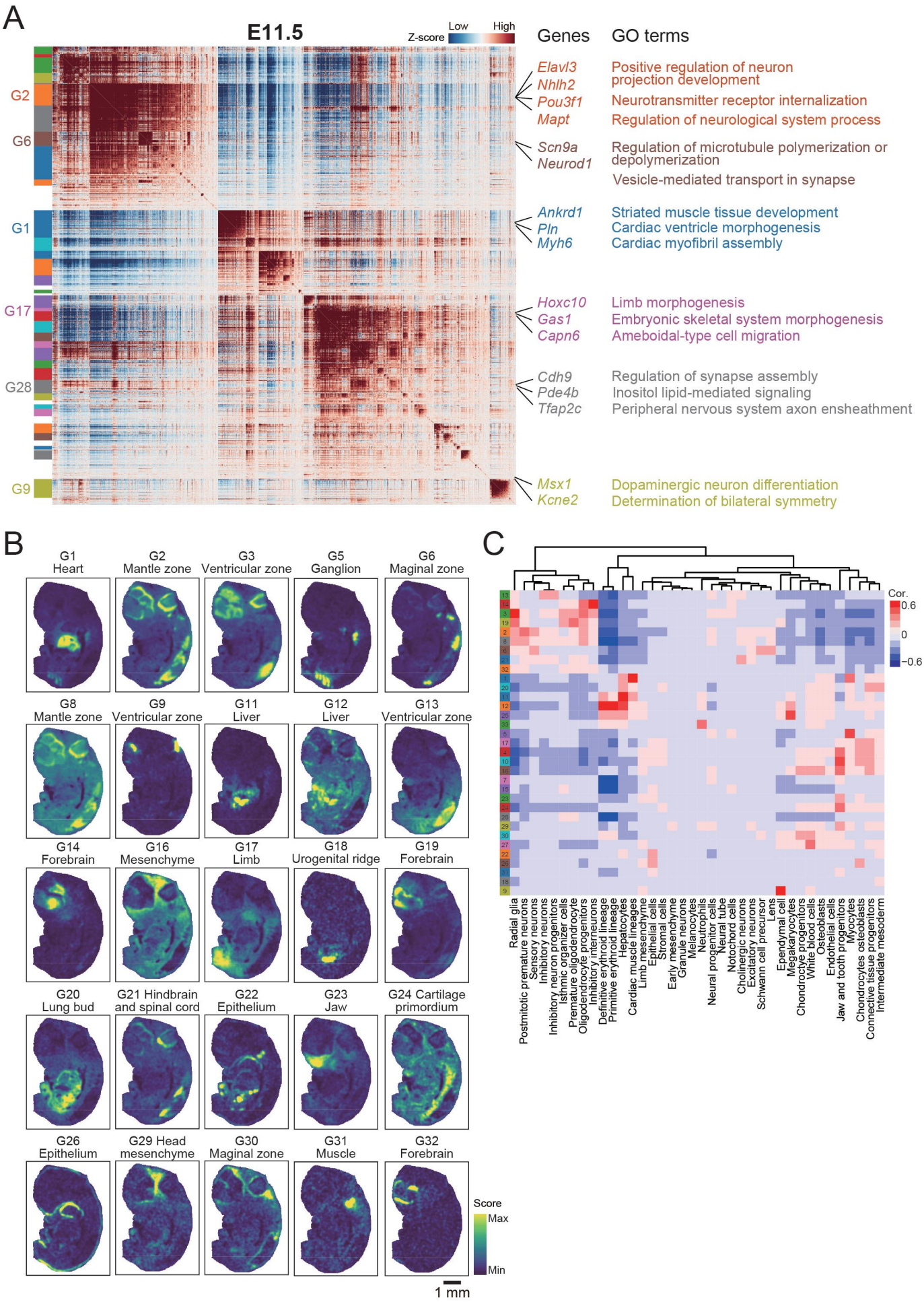
A
E11.5
Z-score
Low
High
Genes
GO terms
G2
G6
G1
G17
G28
G9
Elavl3
Nhlh2
Pou3f1
Mapt
Positive regulation of neuron projection development
Neurotransmitter receptor internalization
Regulation of neurological system process
Scn9a
Neurod1
Regulation of microtubule polymerization or depolymerization
Vesicle-mediated transport in synapse
Ankrd1
Pln
Myh6
Striated muscle tissue development
Cardiac ventricle morphogenesis
Cardiac myofibril assembly
Hoxc10
Gas1
Capn6
Limb morphogenesis
Embryonic skeletal system morphogenesis
Ameboidal-type cell migration
Cdh9
Pde4b
Tfap2c
Regulation of synapse assembly
Inositol lipid-mediated signaling
Peripheral nervous system axon ensheathment
Msx1
Kcne2
Dopaminergic neuron differentiation
Determination of bilateral symmetry
B
G1 Heart
G2 Mantle zone
G3 Ventricular zone
G5 Ganglion
G6 Maginal zone
G8 Mantle zone
G9 Ventricular zone
G11 Liver
G12 Liver
G13 Ventricular zone
G14 Forebrain
G16 Mesenchyme
G17 Limb
G18 Urogenital ridge
G19 Forebrain
G20 Lung bud
G21 Hindbrain and spinal cord
G22 Epithelium
G23 Jaw
G24 Cartilage primordium
G26 Epithelium
G29 Head mesenchyme
G30 Maginal zone
G31 Muscle
G32 Forebrain
Score
Max
Min
1 mm
C
Cor.
0.6
0
−0.6
Radial glia
Postmitotic premature neurons
Sensory neurons
Inhibitory neurons
Inhibitory neuron progenitors
Isthmic organizer cells
Premature oligodendrocyte
Oligodendrocyte progenitors
Inhibitory interneurons
Definitive erythroid lineage
Primitive erythroid lineage
Hepatocytes
Cardiac muscle lineages
Limb mesenchyme
Epithelial cells
Stromal cells
Early mesenchyme
Granule neurons
Melanocytes
Neutrophils
Neural progenitor cells
Neural tube
Notochord cells
Cholinergic neurons
Excitatory neurons
Schwann cell precursor
Lens
Ependymal cell
Megakaryocytes
Chondrocyte progenitors
White blood cells
Osteoblasts
Endothelial cells
Jaw and tooth progenitors
Myocytes
Chondrocytes osteoblasts
Connective tissue progenitors
Intermediate mesoderm

Figure S9

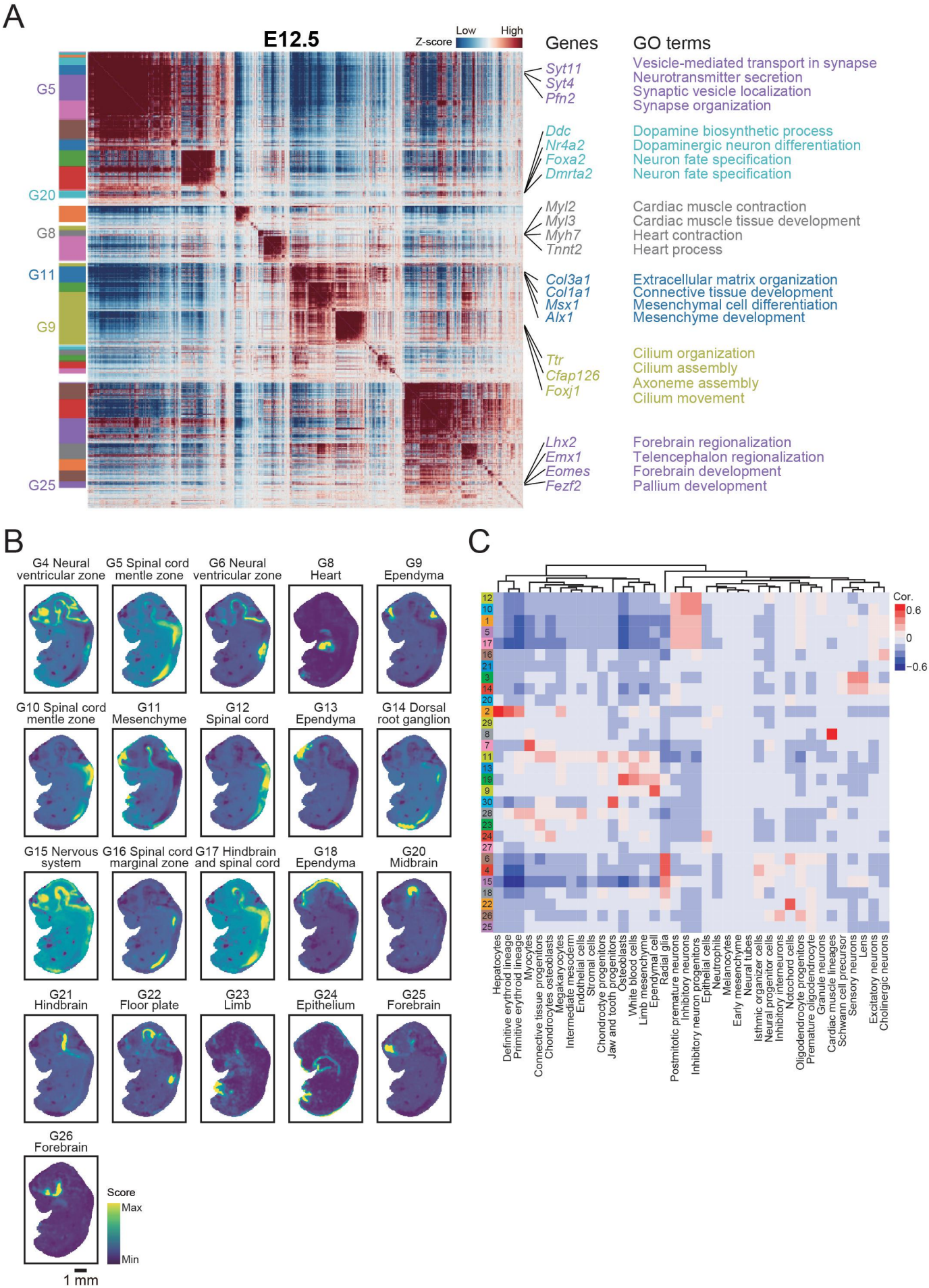
A
E12.5
Z-score
Low
High
Genes
GO terms
G5
G20
G8
G11
G9
G25
Syt11
Syt4
Pfn2
Vesicle-mediated transport in synapse
Neurotransmitter secretion
Synaptic vesicle localization
Synapse organization
Ddc
Nr4a2
Foxa2
Dmrta2
Dopamine biosynthetic process
Dopaminergic neuron differentiation
Neuron fate specification
Neuron fate specification
Myl2
Myl3
Myh7
Tnnt2
Cardiac muscle contraction
Cardiac muscle tissue development
Heart contraction
Heart process
Col3a1
Col1a1
Msx1
Alx1
Extracellular matrix organization
Connective tissue development
Mesenchymal cell differentiation
Mesenchyme development
Ttr
Cfap126
Foxj1
Cilium organization
Cilium assembly
Axoneme assembly
Cilium movement
Lhx2
Emx1
Eomes
Fezf2
Forebrain regionalization
Telencephalon regionalization
Forebrain development
Pallium development
B
G4 Neural ventricular zone
G5 Spinal cord mentle zone
G6 Neural ventricular zone
G8 Heart
G9 Ependyma
G10 Spinal cord mentle zone
G11 Mesenchyme
G12 Spinal cord
G13 Ependyma
G14 Dorsal root ganglion
G15 Nervous system
G16 Spinal cord marginal zone
G17 Hindbrain and spinal cord
G18 Ependyma
G20 Midbrain
G21 Hindbrain
G22 Floor plate
G23 Limb
G24 Epithelium
G25 Forebrain
G26 Forebrain
Score
Max
Min
1 mm
C
Cor.
0.6
0
−0.6
Hepatocytes
Definitive erythroid lineage
Primitive erythroid lineage
Myocytes
Connective tissue progenitors
Chondrocytes osteoblasts
Megakaryocytes
Intermediate mesoderm
Endothelial cells
Stromal cells
Chondroctye progenitors
Jaw and tooth progenitors
Osteoblasts
White blood cells
Limb mesenchyme
Ependymal cell
Radial glia
Postmitotic premature neurons
Inhibitory neurons
Inhibitory neuron progenitors
Epithelial cells
Neutrophils
Melanocytes
Early mesenchyme
Neural tubes
Isthmic organizer cells
Neural progenitor cells
Inhibitory interneurons
Notochord cells
Oligodendrocyte progenitors
Premature oligodendrocyte
Granule neurons
Cardiac muscle lineages
Schwann cell precursor
Sensory neurons
Lens
Excitatory neurons
Cholinergic neurons

Figure S10

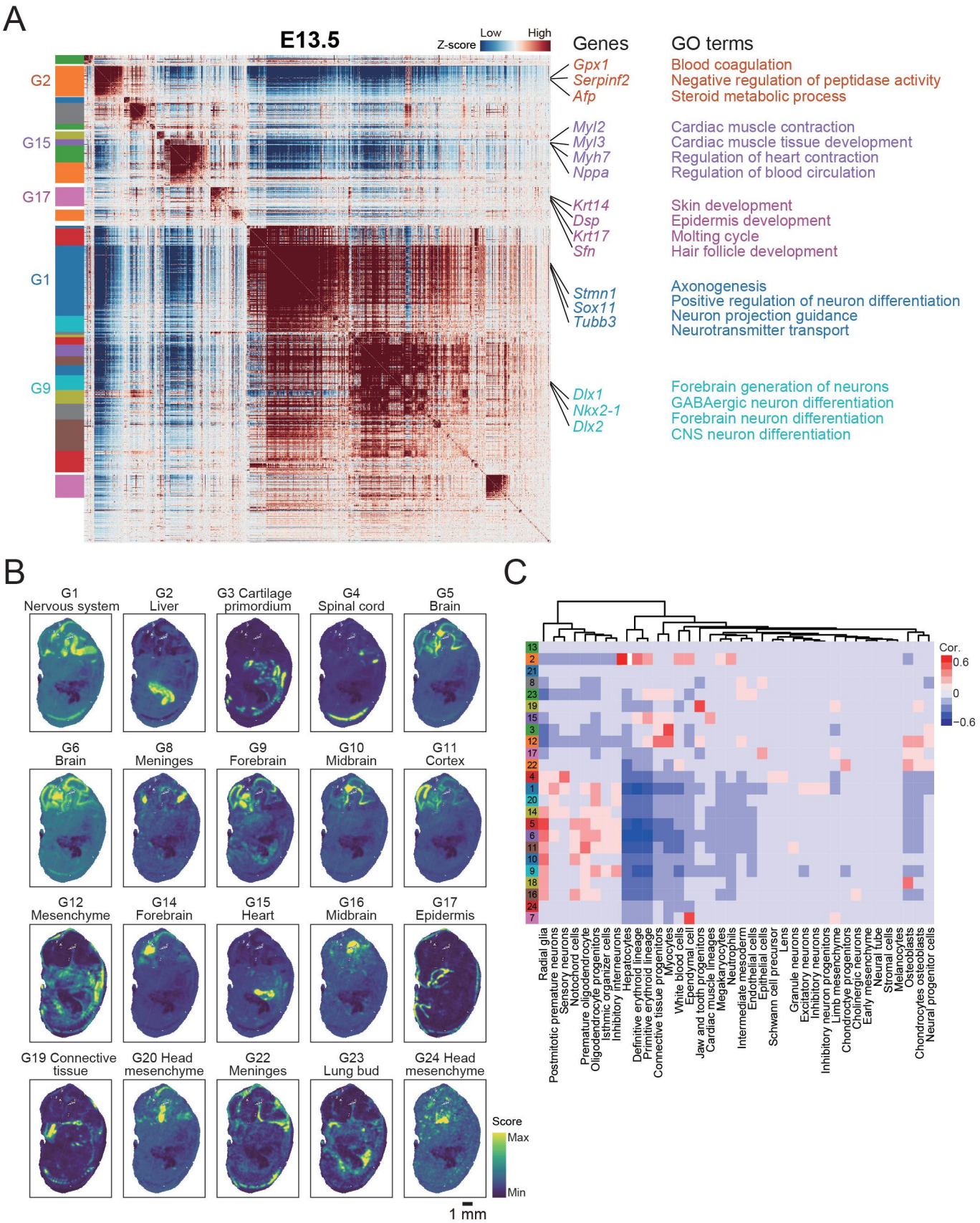
A
E13.5
Z-score
Low
High
Genes
GO terms
G2
G15
G17
G1
G9
Gpx1
Serpinf2
Afp
Blood coagulation
Negative regulation of peptidase activity
Steroid metabolic process
Myl2
Myl3
Myh7
Nppa
Cardiac muscle contraction
Cardiac muscle tissue development
Regulation of heart contraction
Regulation of blood circulation
Krt14
Dsp
Krt17
Sfn
Skin development
Epidermis development
Molting cycle
Hair follicle development
Stmn1
Sox11
Tubb3
Axonogenesis
Positive regulation of neuron differentiation
Neuron projection guidance
Neurotransmitter transport
Dlx1
Nkx2-1
Dlx2
Forebrain generation of neurons
GABAergic neuron differentiation
Forebrain neuron differentiation
CNS neuron differentiation
B
G1 Nervous system
G2 Liver
G3 Cartilage primordium
G4 Spinal cord
G5 Brain
G6 Brain
G8 Meninges
G9 Forebrain
G10 Midbrain
G11 Cortex
G12 Mesenchyme
G14 Forebrain
G15 Heart
G16 Midbrain
G17 Epidermis
G19 Connective tissue
G20 Head mesenchyme
G22 Meninges
G23 Lung bud
G24 Head mesenchyme
Score
Max
Min
1 mm
C
Cor.
0.6
0
−0.6
Radial glia
Postmitotic premature neurons
Sensory neurons
Notochord cells
Premature oligodendrocyte
Oligodendrocyte progenitors
Isthmic organizer cells
Inhibitory interneurons
Hepatocytes
Definitive erythroid lineage
Primitive erythroid lineage
Connective tissue progenitors
Myocytes
White blood cells
Ependymal cell
Jaw and tooth progenitors
Cardiac muscle lineages
Megakaryocytes
Neutrophils
Intermediate mesoderm
Endothelial cells
Epithelial cells
Schwann cell precursor
Lens
Granule neurons
Excitatory neurons
Inhibitory neurons
Inhibitory neuron progenitors
Limb mesenchyme
Chondrocyte progenitors
Cholinergic neurons
Early mesenchyme
Neural tube
Stromal cells
Melanocytes
Osteoblasts
Chondrocytes osteoblasts
Neural progenitor cells

Figure S11

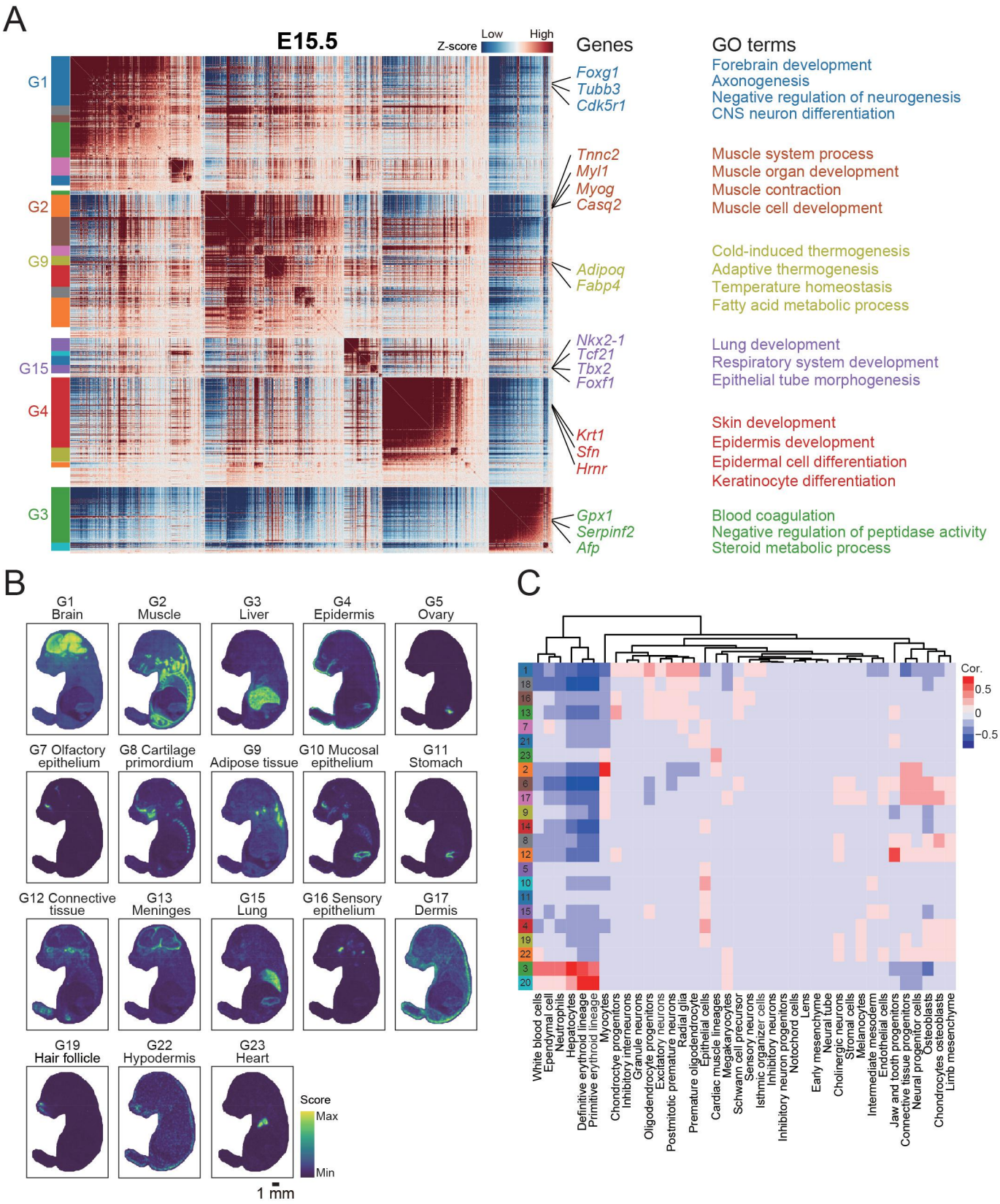
A
E15.5
Z-score
Low
High
Genes
GO terms
G1
G2
G9
G15
G4
G3
Foxg1
Tubb3
Cdk5r1
Tnnc2
Myl1
Myog
Casq2
Adipoq
Fabp4
Nkx2-1
Tcf21
Tbx2
Foxf1
Krt1
Sfn
Hrnr
Gpx1
Serpinf2
Afp
Forebrain development
Axonogenesis
Negative regulation of neurogenesis
CNS neuron differentiation
Muscle system process
Muscle organ development
Muscle contraction
Muscle cell development
Cold-induced thermogenesis
Adaptive thermogenesis
Temperature homeostasis
Fatty acid metabolic process
Lung development
Respiratory system development
Epithelial tube morphogenesis
Skin development
Epidermis development
Epidermal cell differentiation
Keratinocyte differentiation
Blood coagulation
Negative regulation of peptidase activity
Steroid metabolic process
B
G1 Brain
G2 Muscle
G3 Liver
G4 Epidermis
G5 Ovary
G7 Olfactory epithelium
G8 Cartilage primordium
G9 Adipose tissue
G10 Mucosal epithelium
G11 Stomach
G12 Connective tissue
G13 Meninges
G15 Lung
G16 Sensory epithelium
G17 Dermis
G19 Hair follicle
G22 Hypodermis
G23 Heart
Score
Max
Min
1 mm
C
Cor.
0.5
0
−0.5
White blood cells
Ependymal cell
Neutrophils
Hepatocytes
Definitive erythroid lineage
Primitive erythroid lineage
Myocytes
Chondroctye progenitors
Inhibitory interneurons
Granule neurons
Oligodendrocyte progenitors
Excitatory neurons
Postmitotic premature neurons
Radial glia
Premature oligodendrocyte
Epithelial cells
Cardiac muscle lineages
Megakaryocytes
Schwann cell precursor
Sensory neurons
Isthmic organizer cells
Inhibitory neurons
Inhibitory neuron progenitors
Notochord cells
Lens
Early mesenchyme
Neural tube
Cholinergic neurons
Stromal cells
Melanocytes
Intermediate mesoderm
Endothelial cells
Jaw and tooth progenitors
Connective tissue progenitors
Neural progenitor cells
Osteoblasts
Chondrocytes osteoblasts
Limb mesenchyme

Figure S12

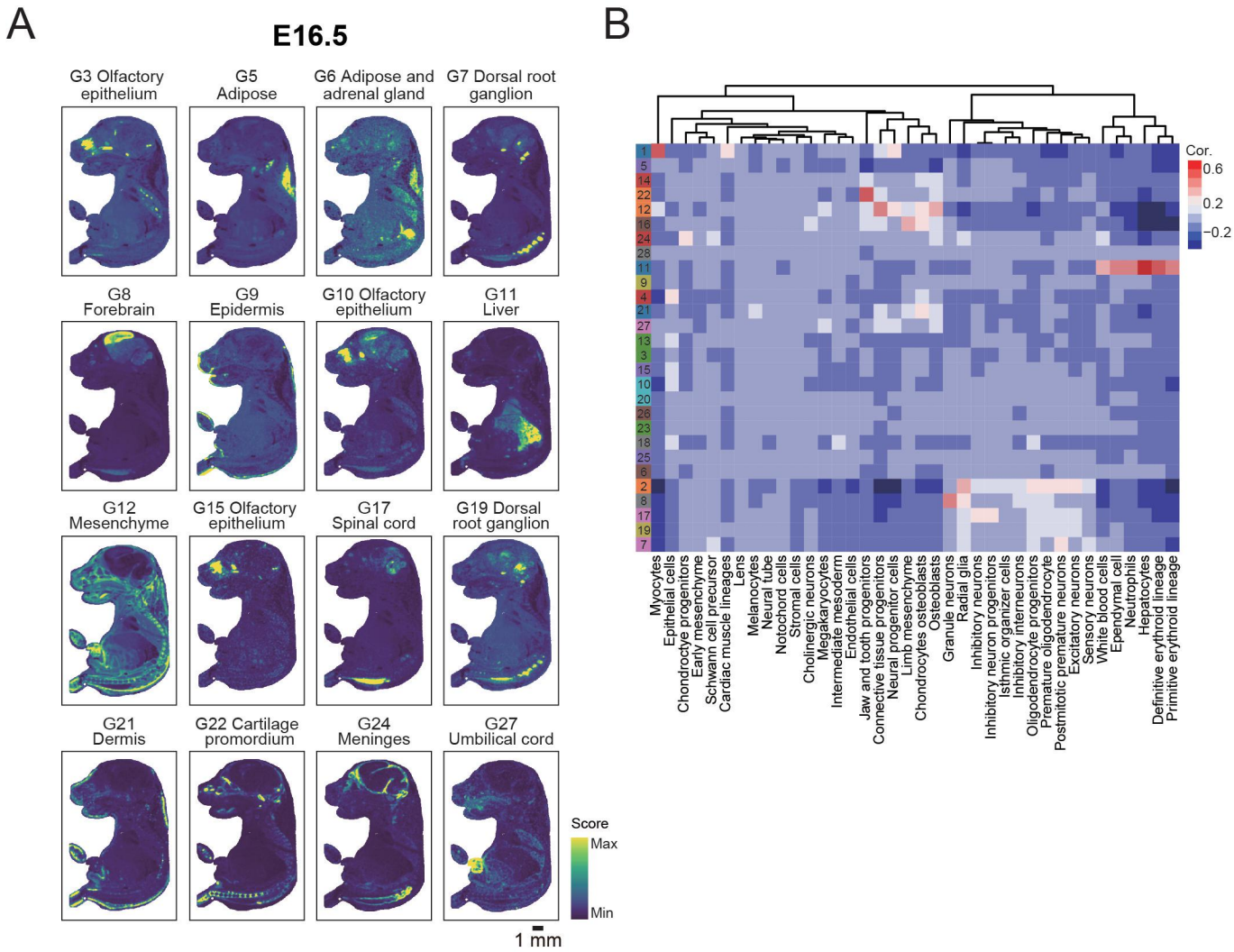
A
E16.5
G3 Olfactory epithelium
G5 Adipose
G6 Adipose and adrenal gland
G7 Dorsal root ganglion
G8 Forebrain
G9 Epidermis
G10 Olfactory epithelium
G11 Liver
G12 Mesenchyme
G15 Olfactory epithelium
G17 Spinal cord
G19 Dorsal root ganglion
G21 Dermis
G22 Cartilage promordium
G24 Meninges
G27 Umbilical cord
Score
Max
Min
1 mm
B
Cor.
0.6
0.2
−0.2
Myocytes
Epithelial cells
Chondroctye progenitors
Early mesenchyme
Schwann cell precursor
Cardiac muscle lineages
Lens
Melanocytes
Neural tube
Notochord cells
Stromal cells
Cholinergic neurons
Megakaryocytes
Intermediate mesoderm
Endothelial cells
Jaw and tooth progenitors
Connective tissue progenitors
Neural progenitor cells
Limb mesenchyme
Chondrocytes osteoblasts
Osteoblasts
Granule neurons
Radial glia
Inhibitory neurons
Inhibitory neuron progenitors
Isthmic organizer cells
Inhibitory interneurons
Oligodendrocyte progenitors
Premature oligodendrocyte
Postmitotic premature neurons
Excitatory neurons
Sensory neurons
White blood cells
Ependymal cell
Neutrophils
Hepatocytes
Definitive erythroid lineage
Primitive erythroid lineage

Figure S13

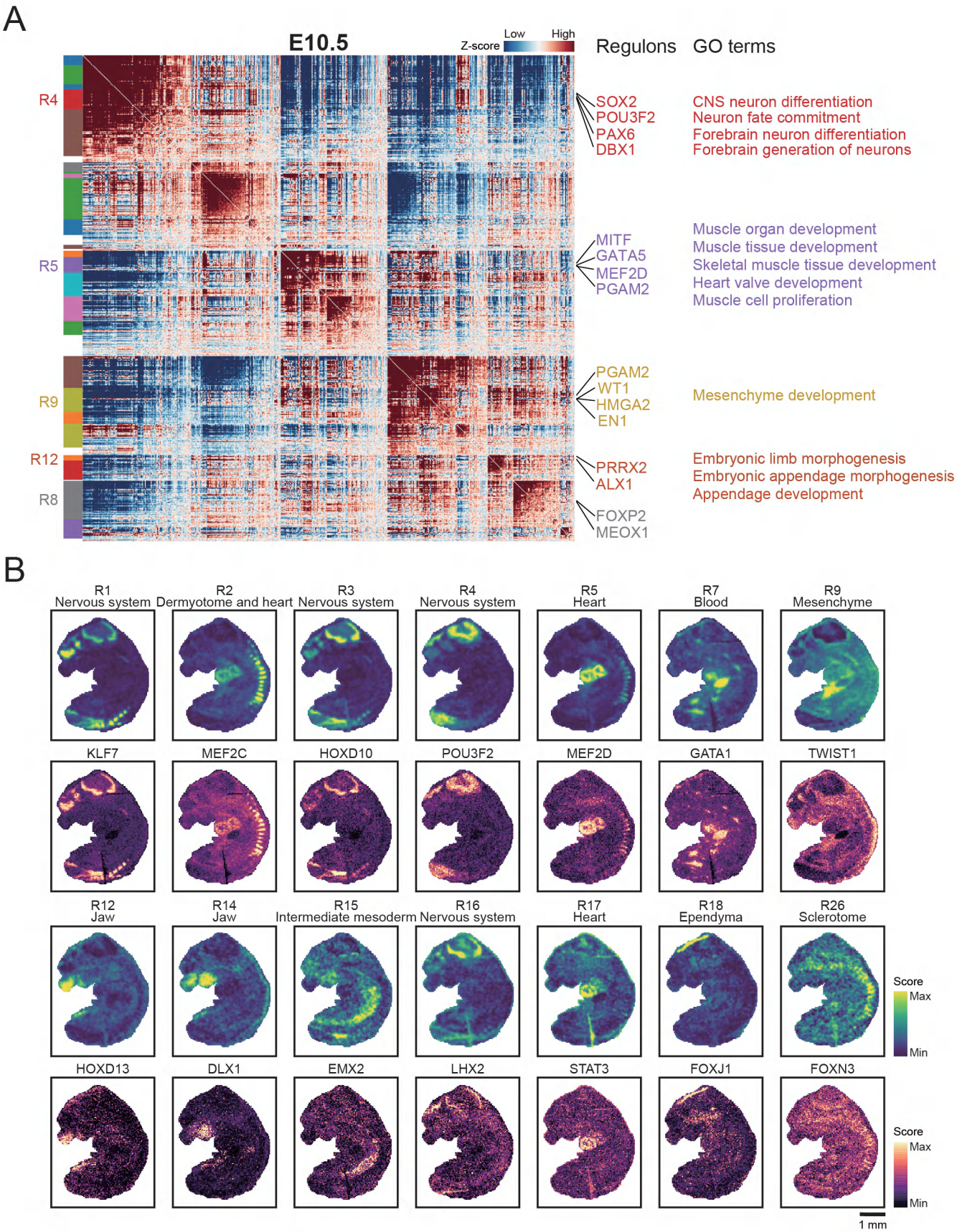
A
E10.5
Z-score
Low
High
Regulons
GO terms
R4
SOX2
POU3F2
PAX6
DBX1
CNS neuron differentiation
Neuron fate commitment
Forebrain neuron differentiation
Forebrain generation of neurons
R5
MITF
GATA5
MEF2D
PGAM2
Muscle organ development
Muscle tissue development
Skeletal muscle tissue development
Heart valve development
Muscle cell proliferation
R9
PGAM2
WT1
HMGA2
EN1
Mesenchyme development
R12
PRRX2
ALX1
Embryonic limb morphogenesis
Embryonic appendage morphogenesis
Appendage development
R8
FOXP2
MEOX1
B
R1 Nervous system
R2 Dermyotome and heart
R3 Nervous system
R4 Nervous system
R5 Heart
R7 Blood
R9 Mesenchyme
KLF7
MEF2C
HOXD10
POU3F2
MEF2D
GATA1
TWIST1
R12 Jaw
R14 Jaw
R15 Intermediate mesoderm
R16 Nervous system
R17 Heart
R18 Ependyma
R26 Sclerotome
Score
Max
Min
HOXD13
DLX1
EMX2
LHX2
STAT3
FOXJ1
FOXN3
Score
Max
Min
1 mm

Figure S14

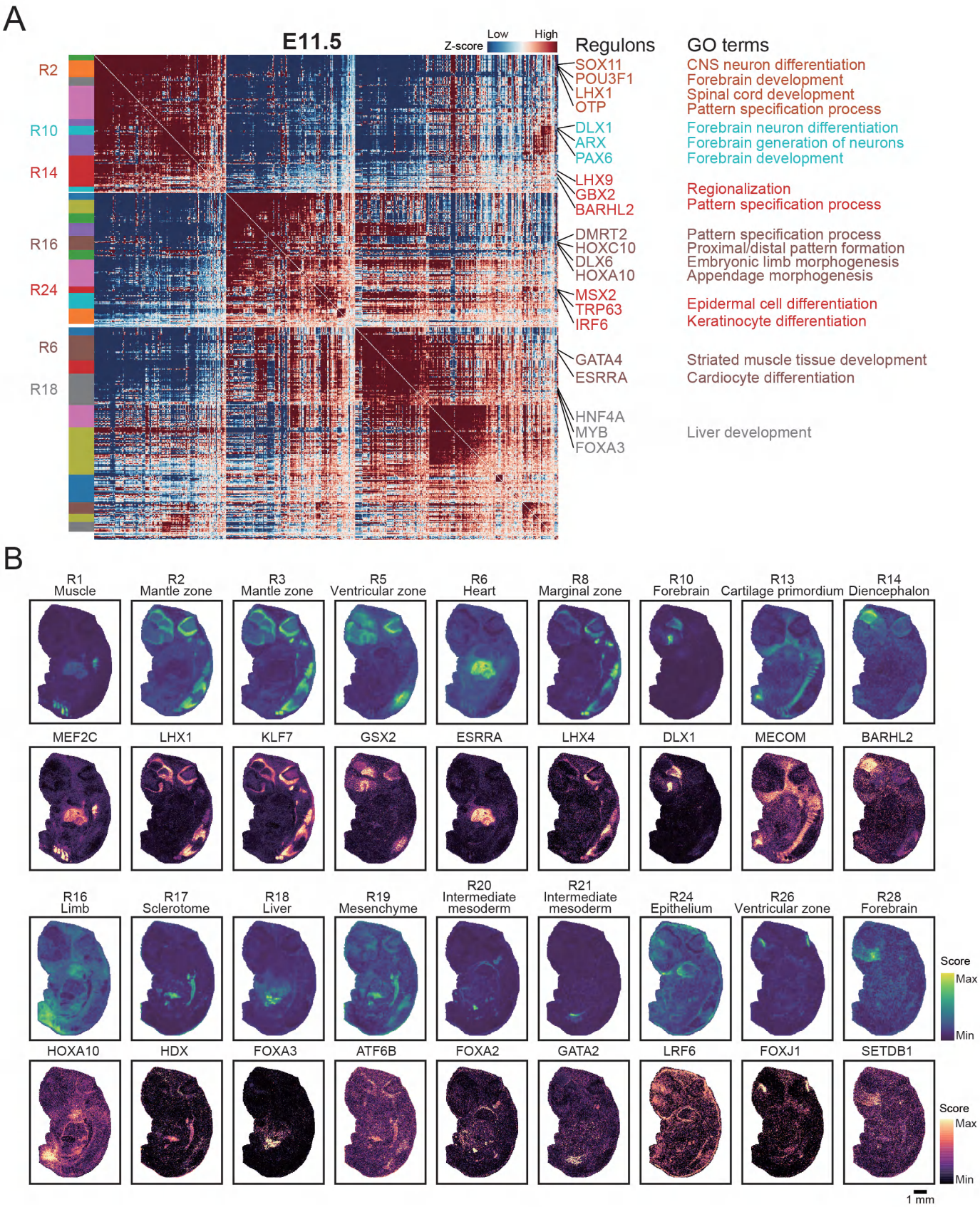
A
E11.5
Z-score
Low
High
R2
R10
R14
R16
R24
R6
R18
Regulons
SOX11
POU3F1
LHX1
OTP
DLX1
ARX
PAX6
LHX9
GBX2
BARHL2
DMRT2
HOXC10
DLX6
HOXA10
MSX2
TRP63
IRF6
GATA4
ESRRA
HNF4A
MYB
FOXA3
GO terms
CNS neuron differentiation
Forebrain development
Spinal cord development
Pattern specification process
Forebrain neuron differentiation
Forebrain generation of neurons
Forebrain development
Regionalization
Pattern specification process
Pattern specification process
Proximal/distal pattern formation
Embryonic limb morphogenesis
Appendage morphogenesis
Epidermal cell differentiation
Keratinocyte differentiation
Striated muscle tissue development
Cardiocyte differentiation
Liver development
B
R1 Muscle
R2 Mantle zone
R3 Mantle zone
R5 Ventricular zone
R6 Heart
R8 Marginal zone
R10 Forebrain
R13 Cartilage primordium
R14 Diencephalon
MEF2C
LHX1
KLF7
GSX2
ESRRA
LHX4
DLX1
MECOM
BARHL2
R16 Limb
R17 Sclerotome
R18 Liver
R19 Mesenchyme
R20 Intermediate mesoderm
R21 Intermediate mesoderm
R24 Epithelium
R26 Ventricular zone
R28 Forebrain
Score
Max
Min
HOXA10
HDX
FOXA3
ATF6B
FOXA2
GATA2
LRF6
FOXJ1
SETDB1
Score
Max
Min
1 mm

Figure S15

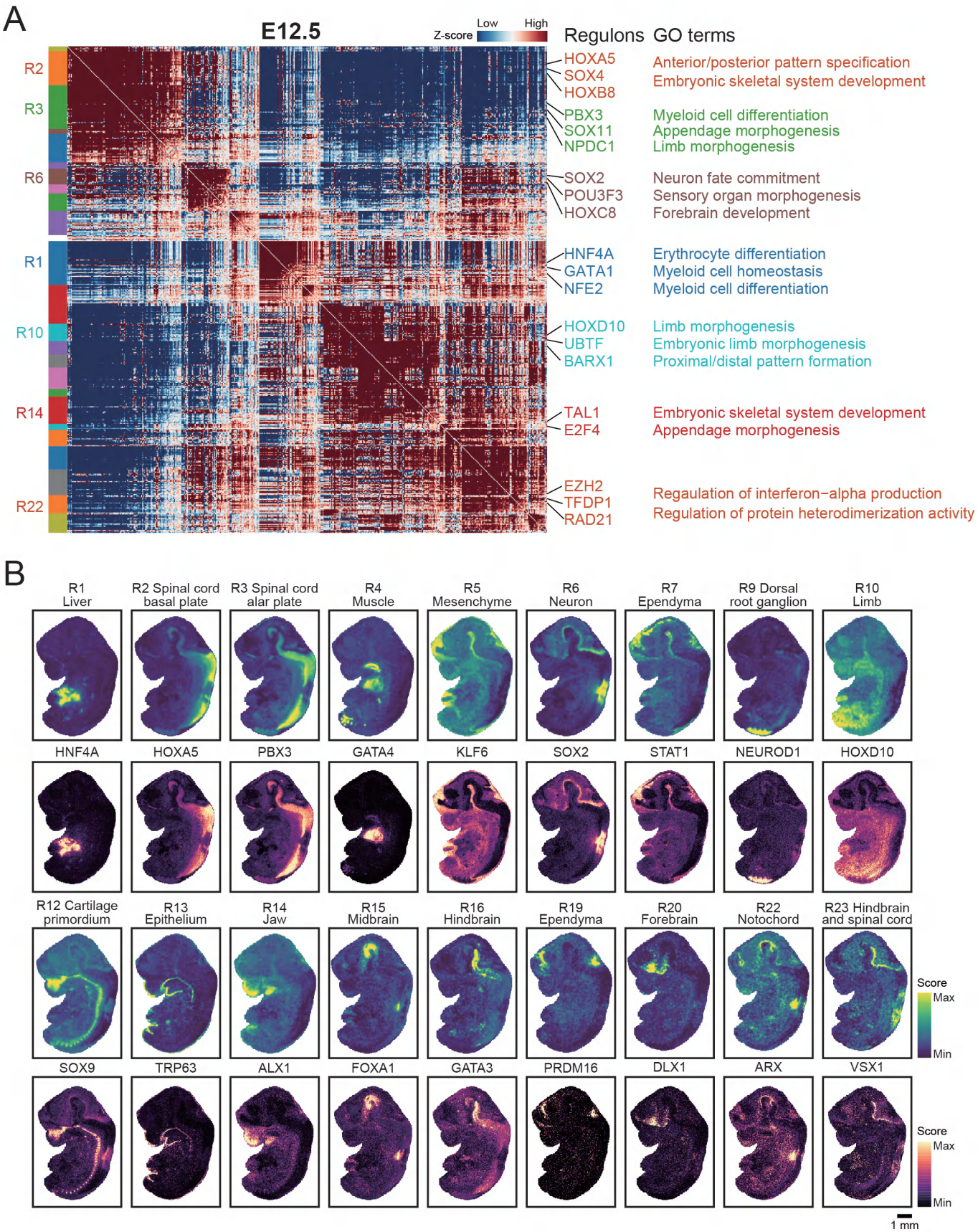
A
E12.5
Z-score
Low
High
Regulons
GO terms
R2
R3
R6
R1
R10
R14
R22
HOXA5
SOX4
HOXB8
Anterior/posterior pattern specification
Embryonic skeletal system development
PBX3
SOX11
NPDC1
Myeloid cell differentiation
Appendage morphogenesis
Limb morphogenesis
SOX2
POU3F3
HOXC8
Neuron fate commitment
Sensory organ morphogenesis
Forebrain development
HNF4A
GATA1
NFE2
Erythrocyte differentiation
Myeloid cell homeostasis
Myeloid cell differentiation
HOXD10
UBTF
BARX1
Limb morphogenesis
Embryonic limb morphogenesis
Proximal/distal pattern formation
TAL1
E2F4
Embryonic skeletal system development
Appendage morphogenesis
EZH2
TFDP1
RAD21
Regaulation of interferon−alpha production
Regulation of protein heterodimerization activity
B
R1 Liver
R2 Spinal cord basal plate
R3 Spinal cord alar plate
R4 Muscle
R5 Mesenchyme
R6 Neuron
R7 Ependyma
R9 Dorsal root ganglion
R10 Limb
HNF4A
HOXA5
PBX3
GATA4
KLF6
SOX2
STAT1
NEUROD1
HOXD10
R12 Cartilage primordium
R13 Epithelium
R14 Jaw
R15 Midbrain
R16 Hindbrain
R19 Ependyma
R20 Forebrain
R22 Notochord
R23 Hindbrain and spinal cord
Score
Max
Min
SOX9
TRP63
ALX1
FOXA1
GATA3
PRDM16
DLX1
ARX
VSX1
Score
Max
Min
1 mm

Figure S16

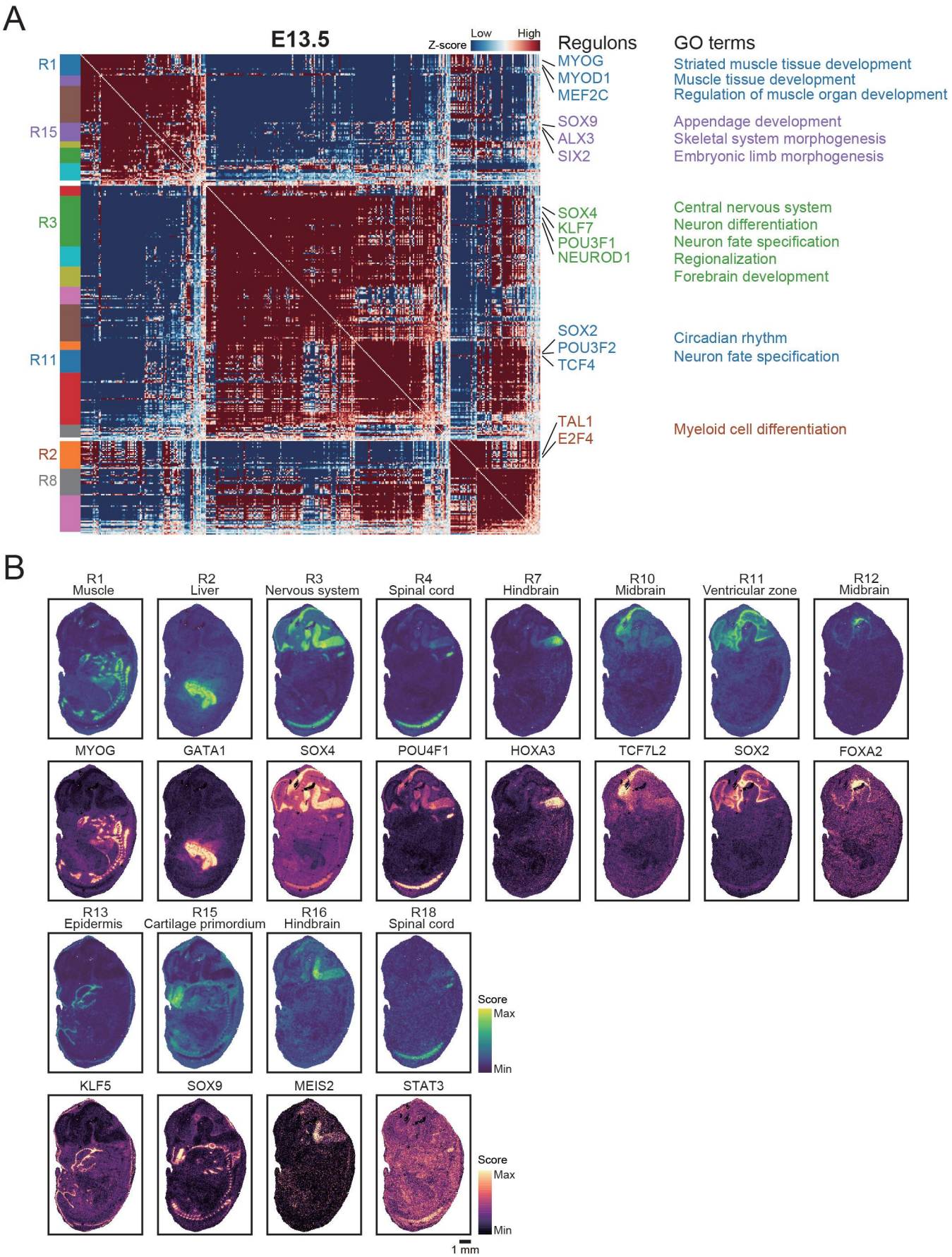
A
E13.5
Z-score
Low
High
R1
R15
R3
R11
R2
R8
Regulons
MYOG
MYOD1
MEF2C
SOX9
ALX3
SIX2
SOX4
KLF7
POU3F1
NEUROD1
SOX2
POU3F2
TCF4
TAL1
E2F4
GO terms
Striated muscle tissue development
Muscle tissue development
Regulation of muscle organ development
Appendage development
Skeletal system morphogenesis
Embryonic limb morphogenesis
Central nervous system
Neuron differentiation
Neuron fate specification
Regionalization
Forebrain development
Circadian rhythm
Neuron fate specification
Myeloid cell differentiation
B
R1 Muscle
R2 Liver
R3 Nervous system
R4 Spinal cord
R7 Hindbrain
R10 Midbrain
R11 Ventricular zone
R12 Midbrain
MYOG
GATA1
SOX4
POU4F1
HOXA3
TCF7L2
SOX2
FOXA2
R13 Epidermis
R15 Cartilage primordium
R16 Hindbrain
R18 Spinal cord
Score
Max
Min
KLF5
SOX9
MEIS2
STAT3
Score
Max
Min
1 mm

Figure S17

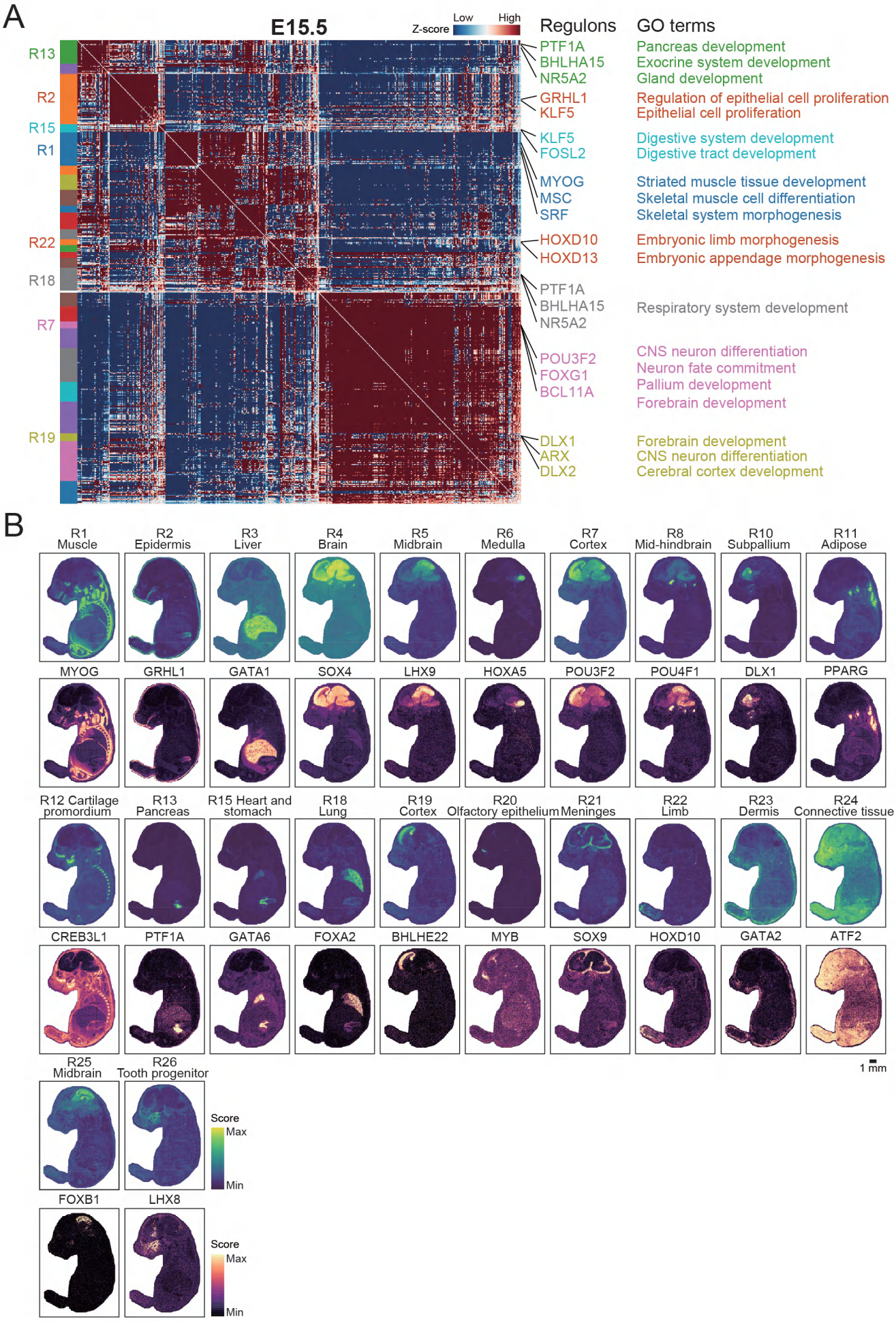
A
E15.5
Z-score
Low
High
Regulons
GO terms
R13
R2
R15
R1
R22
R18
R7
R19
PTF1A
BHLHA15
NR5A2
Pancreas development
Exocrine system development
Gland development
GRHL1
KLF5
Regulation of epithelial cell proliferation
Epithelial cell proliferation
KLF5
FOSL2
Digestive system development
Digestive tract development
MYOG
MSC
SRF
Striated muscle tissue development
Skeletal muscle cell differentiation
Skeletal system morphogenesis
HOXD10
HOXD13
Embryonic limb morphogenesis
Embryonic appendage morphogenesis
PTF1A
BHLHA15
NR5A2
Respiratory system development
POU3F2
FOXG1
BCL11A
CNS neuron differentiation
Neuron fate commitment
Pallium development
Forebrain development
DLX1
ARX
DLX2
Forebrain development
CNS neuron differentiation
Cerebral cortex development
B
R1 Muscle
R2 Epidermis
R3 Liver
R4 Brain
R5 Midbrain
R6 Medulla
R7 Cortex
R8 Mid-hindbrain
R10 Subpallium
R11 Adipose
MYOG
GRHL1
GATA1
SOX4
LHX9
HOXA5
POU3F2
POU4F1
DLX1
PPARG
R12 Cartilage promordium
R13 Pancreas
R15 Heart and stomach
R18 Lung
R19 Cortex
R20 Olfactory epithelium
R21 Meninges
R22 Limb
R23 Dermis
R24 Connective tissue
CREB3L1
PTF1A
GATA6
FOXA2
BHLHE22
MYB
SOX9
HOXD10
GATA2
ATF2
1 mm
R25 Midbrain
R26 Tooth progenitor
Score
Max
Min
FOXB1
LHX8
Score
Max
Min

Figure S18

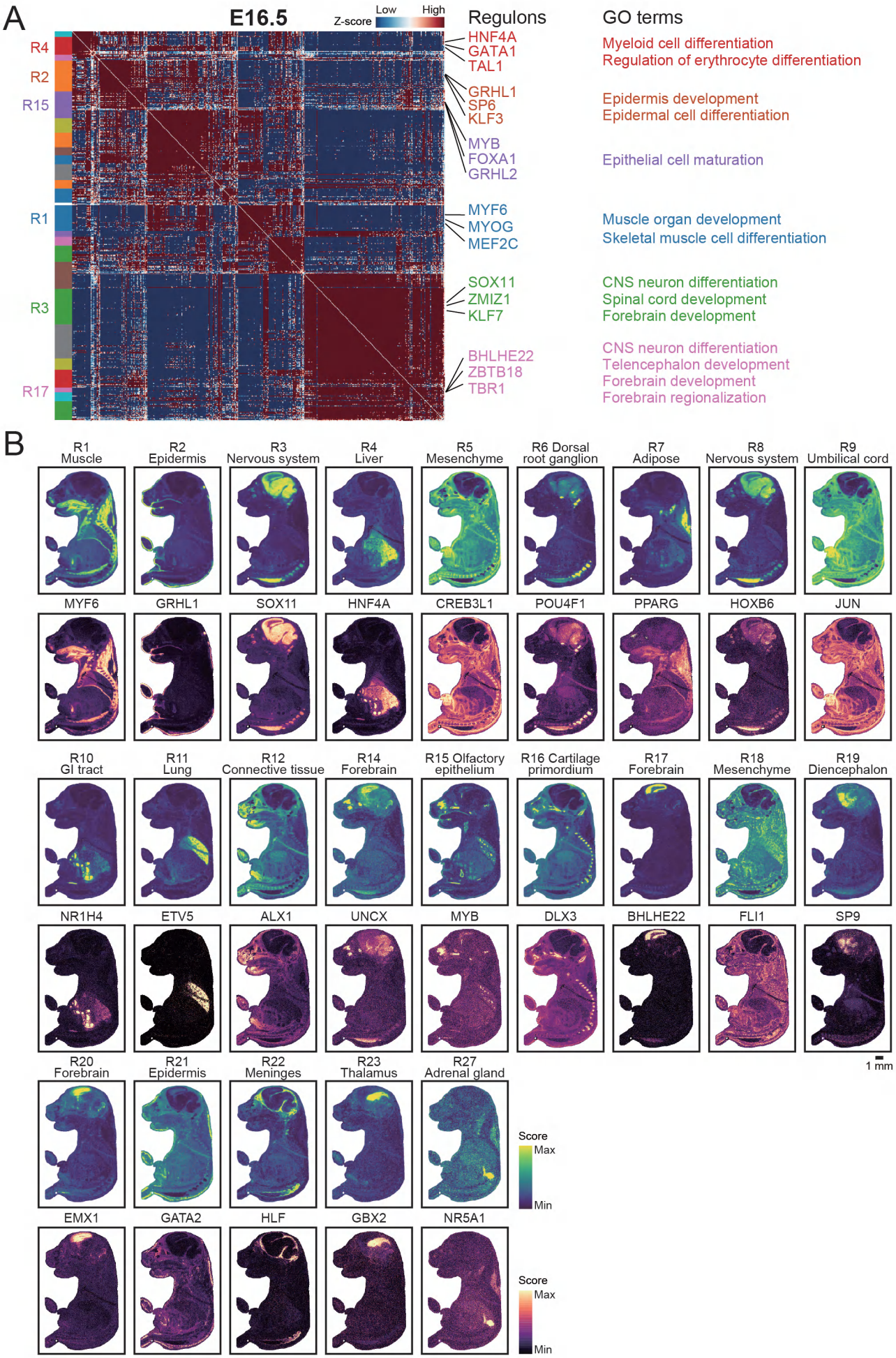
A
E16.5
Z-score
Low
High
Regulons
GO terms
R4
R2
R15
R1
R3
R17
HNF4A
GATA1
TAL1
GRHL1
SP6
KLF3
MYB
FOXA1
GRHL2
MYF6
MYOG
MEF2C
SOX11
ZMIZ1
KLF7
BHLHE22
ZBTB18
TBR1
Myeloid cell differentiation
Regulation of erythrocyte differentiation
Epidermis development
Epidermal cell differentiation
Epithelial cell maturation
Muscle organ development
Skeletal muscle cell differentiation
CNS neuron differentiation
Spinal cord development
Forebrain development
CNS neuron differentiation
Telencephalon development
Forebrain development
Forebrain regionalization
B
R1 Muscle
R2 Epidermis
R3 Nervous system
R4 Liver
R5 Mesenchyme
R6 Dorsal root ganglion
R7 Adipose
R8 Nervous system
R9 Umbilical cord
MYF6
GRHL1
SOX11
HNF4A
CREB3L1
POU4F1
PPARG
HOXB6
JUN
R10 GI tract
R11 Lung
R12 Connective tissue
R14 Forebrain
R15 Olfactory epithelium
R16 Cartilage primordium
R17 Forebrain
R18 Mesenchyme
R19 Diencephalon
NR1H4
ETV5
ALX1
UNCX
MYB
DLX3
BHLHE22
FLI1
SP9
1 mm
R20 Forebrain
R21 Epidermis
R22 Meninges
R23 Thalamus
R27 Adrenal gland
Score
Max
Min
EMX1
GATA2
HLF
GBX2
NR5A1
Score
Max
Min

Figure S19

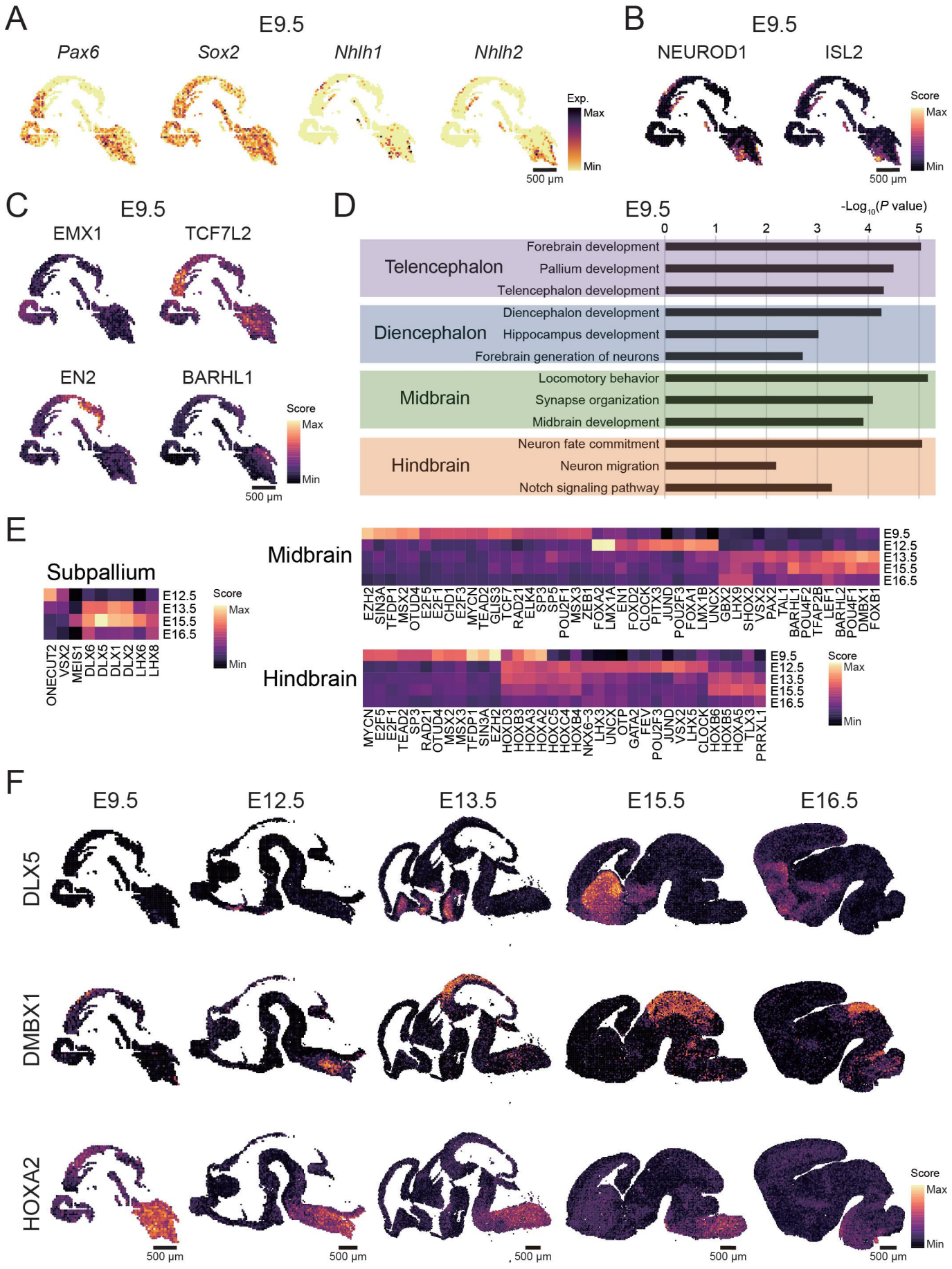
A
E9.5
Pax6
Sox2
Nhlh1
Nhlh2
Exp.
Max
Min
500 μm
B
E9.5
NEUROD1
ISL2
Score
Max
Min
500 μm
C
E9.5
EMX1
TCF7L2
EN2
BARHL1
Score
Max
Min
500 μm
D
E9.5
-Log10(P value)
0
1
2
3
4
5
Telencephalon
Forebrain development
Pallium development
Telencephalon development
Diencephalon
Diencephalon development
Hippocampus development
Forebrain generation of neurons
Midbrain
Locomotory behavior
Synapse organization
Midbrain development
Hindbrain
Neuron fate commitment
Neuron migration
Notch signaling pathway
E
Subpallium
E12.5
E13.5
E15.5
E16.5
ONECUT2
VSX2
MEIS1
DLX6
DLX5
DLX1
DLX2
LHX6
LHX8
Score
Max
Min
Midbrain
E9.5
E12.5
E13.5
E15.5
E16.5
EZH2
SIN3A
TFDP1
MSX2
OTUD4
E2F5
E2F1
CHD1
E2F3
MYCN
TEAD2
GLIS3
TCF7
RAD21
ELK4
SP3
SP5
POU2F1
MSX3
ZEB1
FOXA2
LMX1A
EN1
FOXD2
CLOCK
PITX3
JUND
POU2F3
FOXA1
LMX1B
UNCX
GBX2
LHX9
SHOX2
VSX2
PAX2
TAL1
BARHL1
POU4F2
TFAP2B
LEF1
BARHL2
POU4F1
DMBX1
FOXB1
Hindbrain
E9.5
E12.5
E13.5
E15.5
E16.5
MYCN
E2F5
E2F1
TEAD2
SP3
RAD21
OTUD4
MSX2
MSX3
TFDP1
SIN3A
EZH2
HOXD3
HOXB3
HOXA3
HOXA2
HOXC5
HOXC4
HOXB4
NKX6-3
LHX3
UNCX
OTP
GATA2
FEV
POU2F3
JUND
VSX2
LHX5
CLOCK
HOXB6
HOXB5
HOXA5
TLX3
PRRXL1
Score
Max
Min
F
E9.5
E12.5
E13.5
E15.5
E16.5
DLX5
DMBX1
HOXA2
Score
Max
Min
500 μm
500 μm
500 μm
500 μm
500 μm

Figure S20

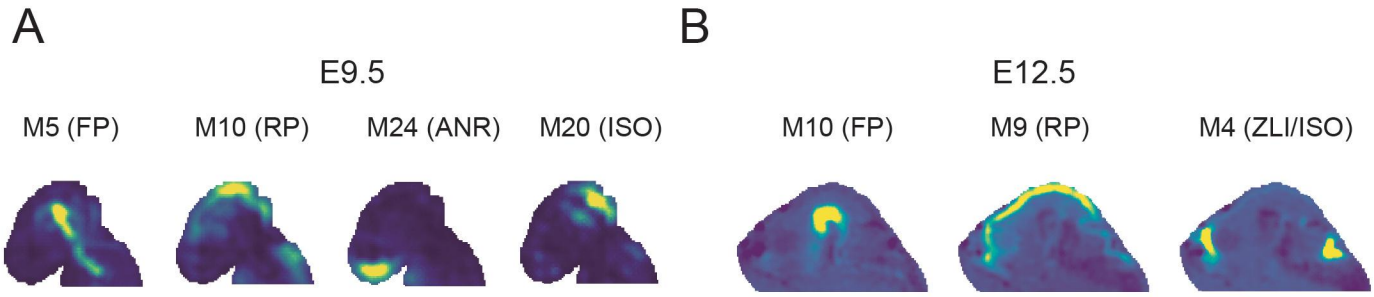
A
E9.5
M5 (FP)
M10 (RP)
M24 (ANR)
M20 (ISO)
B
E12.5
M10 (FP)
M9 (RP)
M4 (ZLI/ISO)

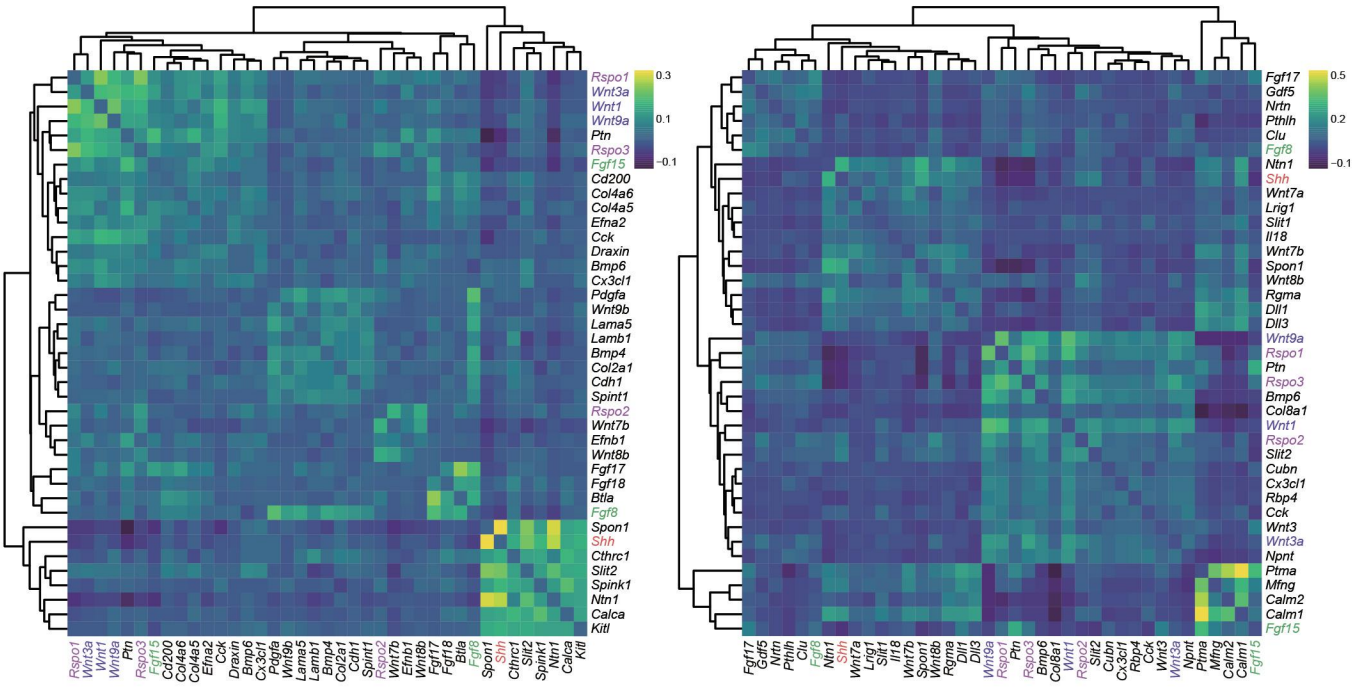
C
Ligand expression correlation
E9.5
D
Ligand expression correlation
E12.5

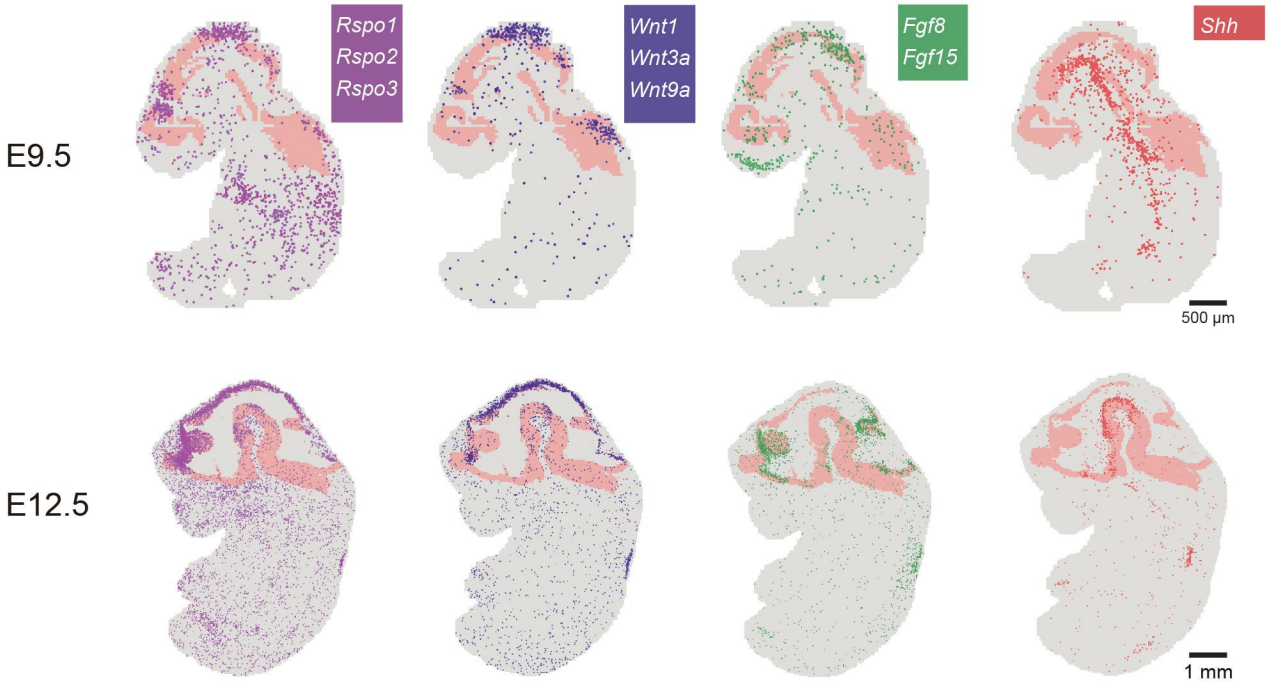
E
E9.5
E12.5
Rspo1
Rspo2
Rspo3
Wnt1
Wnt3a
Wnt9a
Fgf8
Fgf15
Shh
500 µm
1 mm

Figure S21

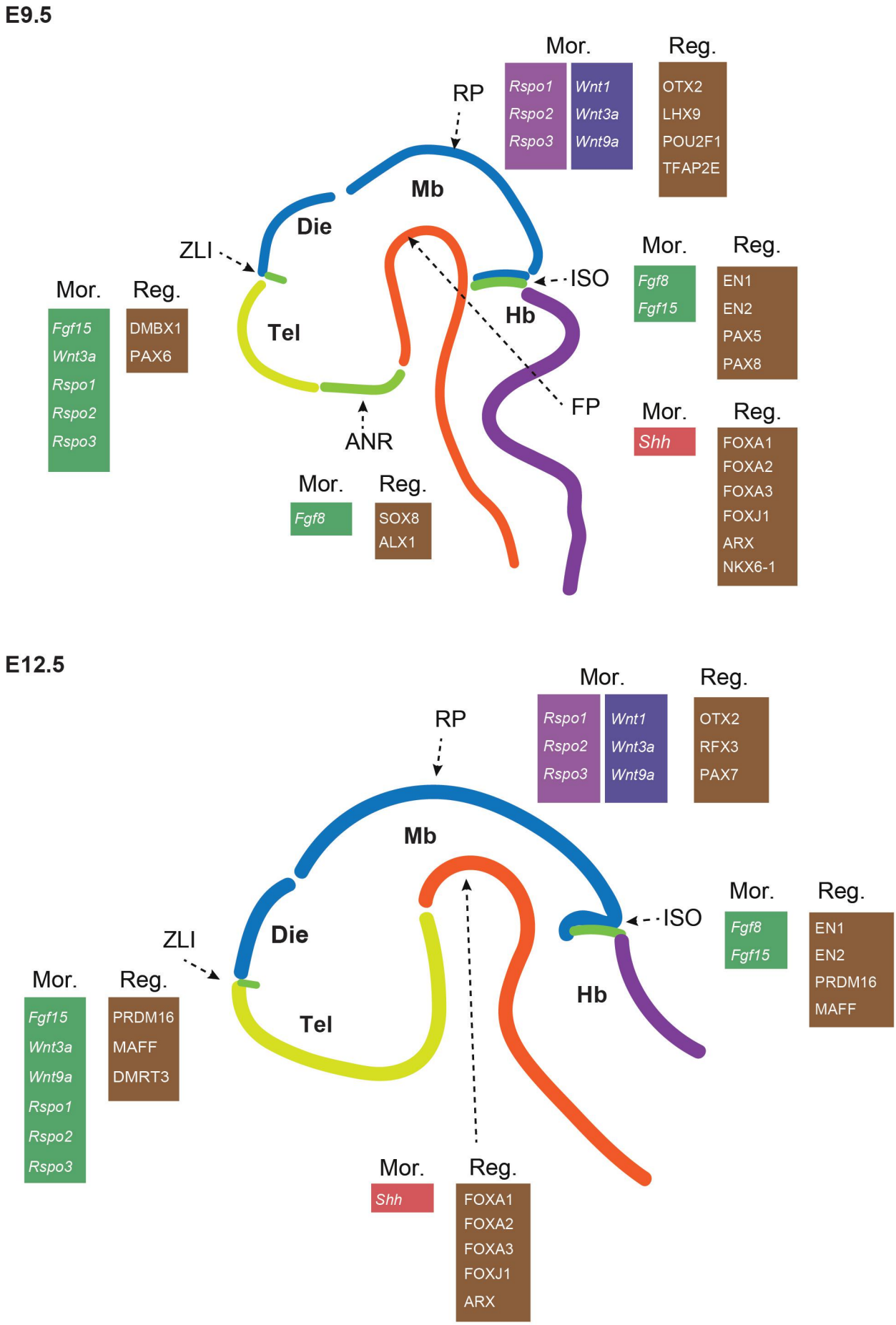
E9.5
Mor.
Reg.
RP
Rspo1
Rspo2
Rspo3
Wnt1
Wnt3a
Wnt9a
OTX2
LHX9
POU2F1
TFAP2E
Mb
Die
ZLI
ISO
Mor.
Reg.
Fgf8
Fgf15
EN1
EN2
PAX5
PAX8
Mor.
Reg.
Fgf15
Wnt3a
Rspo1
Rspo2
Rspo3
DMBX1
PAX6
Tel
Hb
FP
Mor.
Reg.
Shh
FOXA1
FOXA2
FOXA3
FOXJ1
ARX
NKX6-1
ANR
Mor.
Reg.
Fgf8
SOX8
ALX1
E12.5
Mor.
Reg.
RP
Rspo1
Rspo2
Rspo3
Wnt1
Wnt3a
Wnt9a
OTX2
RFX3
PAX7
Mb
Mor.
Reg.
ISO
Fgf8
Fgf15
EN1
EN2
PRDM16
MAFF
ZLI
Die
Mor.
Reg.
Fgf15
Wnt3a
Wnt9a
Rspo1
Rspo2
Rspo3
PRDM16
MAFF
DMRT3
Tel
Hb
Mor.
Reg.
Shh
FOXA1
FOXA2
FOXA3
FOXJ1
ARX

Figure S22

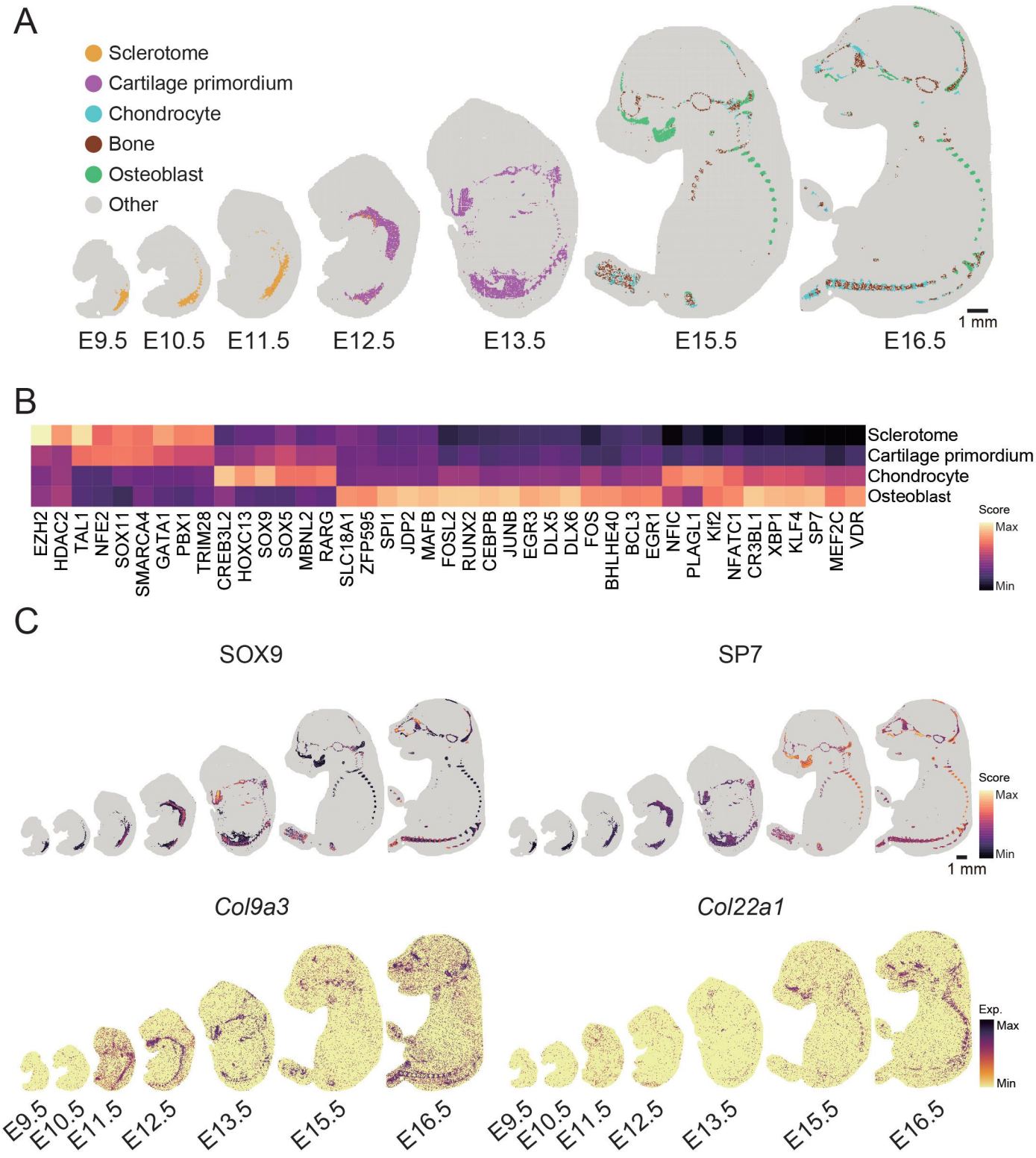
A
Sclerotome
Cartilage primordium
Chondrocyte
Bone
Osteoblast
Other
E9.5
E10.5
E11.5
E12.5
E13.5
E15.5
E16.5
1 mm
B
Sclerotome
Cartilage primordium
Chondrocyte
Osteoblast
EZH2
HDAC2
TAL1
NFE2
SOX11
SMARCA4
GATA1
PBX1
TRIM28
CREB3L2
HOXC13
SOX9
SOX5
MBNL2
RARG
SLC18A1
ZFP595
SPI1
JDP2
MAFB
FOSL2
RUNX2
CEBPB
JUNB
EGR3
DLX5
DLX6
FOS
BHLHE40
BCL3
EGR1
NFIC
PLAGL1
Klf2
NFATC1
CR3BL1
XBP1
KLF4
SP7
MEF2C
VDR
Score
Max
Min
C
SOX9
SP7
Score
Max
Min
1 mm
Col9a3
Col22a1
Exp.
Max
Min
E9.5
E10.5
E11.5
E12.5
E13.5
E15.5
E16.5
E9.5
E10.5
E11.5
E12.5
E13.5
E15.5
E16.5

Figure S23

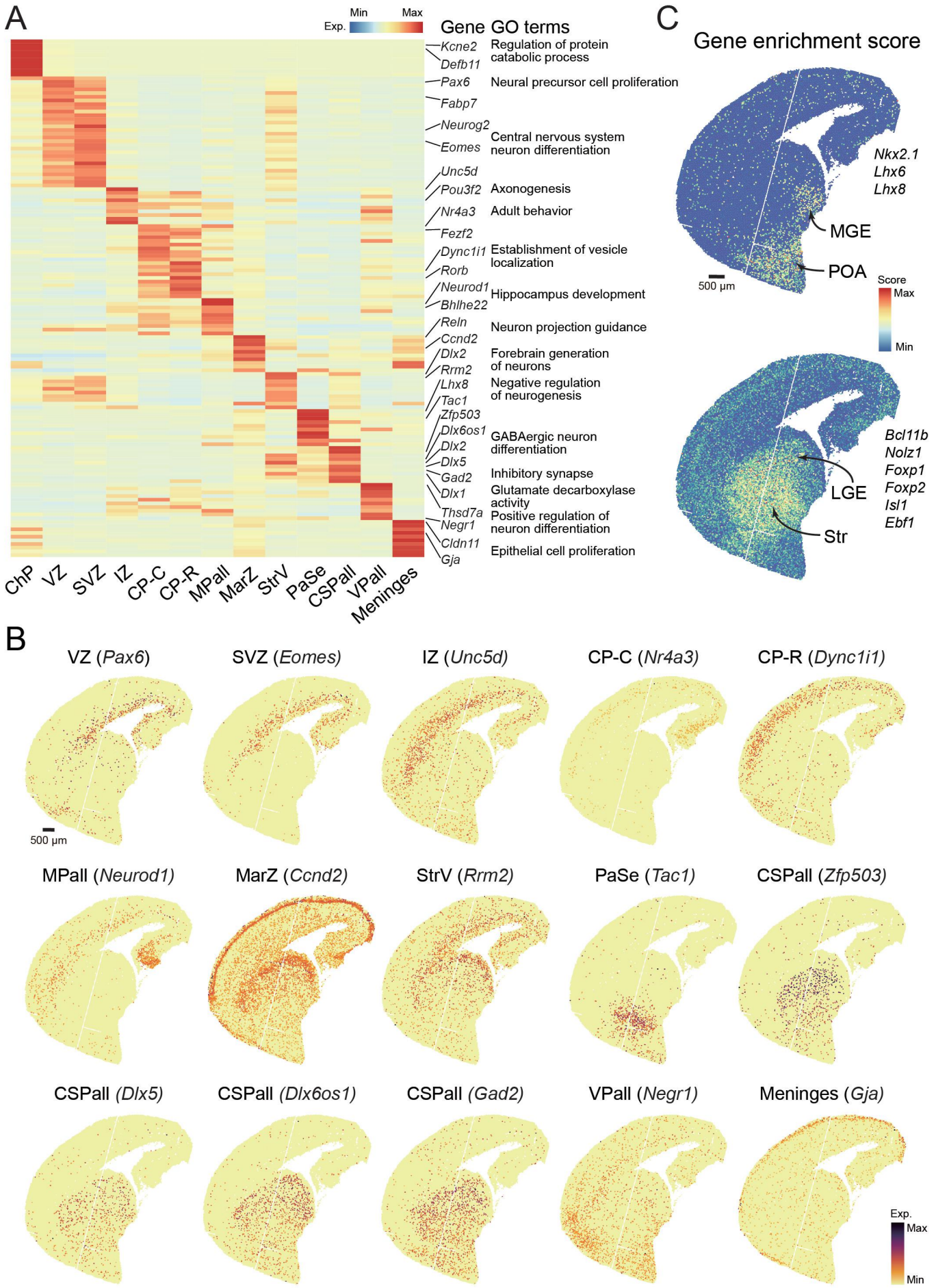
A
Min
Max
Exp.
Gene GO terms
Kcne2
Defb11
Regulation of protein catabolic process
Pax6
Fabp7
Neural precursor cell proliferation
Neurog2
Eomes
Central nervous system neuron differentiation
Unc5d
Pou3f2
Axonogenesis
Nr4a3
Fezf2
Adult behavior
Dync1i1
Rorb
Establishment of vesicle localization
Neurod1
Bhlhe22
Hippocampus development
Reln
Ccnd2
Neuron projection guidance
Dlx2
Rrm2
Forebrain generation of neurons
Lhx8
Tac1
Negative regulation of neurogenesis
Zfp503
Dlx6os1
Dlx2
Dlx5
GABAergic neuron differentiation
Gad2
Inhibitory synapse
Dlx1
Glutamate decarboxylase activity
Thsd7a
Negr1
Positive regulation of neuron differentiation
Cldn11
Gja
Epithelial cell proliferation
ChP
VZ
SVZ
IZ
CP-C
CP-R
MPall
MarZ
StrV
PaSe
CSPall
VPall
Meninges
C
Gene enrichment score
Nkx2.1
Lhx6
Lhx8
MGE
POA
500 µm
Score
Max
Min
Bcl11b
Nolz1
Foxp1
Foxp2
Isl1
Ebf1
LGE
Str
B
VZ (Pax6)
SVZ (Eomes)
IZ (Unc5d)
CP-C (Nr4a3)
CP-R (Dync1i1)
500 µm
MPall (Neurod1)
MarZ (Ccnd2)
StrV (Rrm2)
PaSe (Tac1)
CSPall (Zfp503)
CSPall (Dlx5)
CSPall (Dlx6os1)
CSPall (Gad2)
VPall (Negr1)
Meninges (Gja)
Exp.
Max
Min

Figure S24

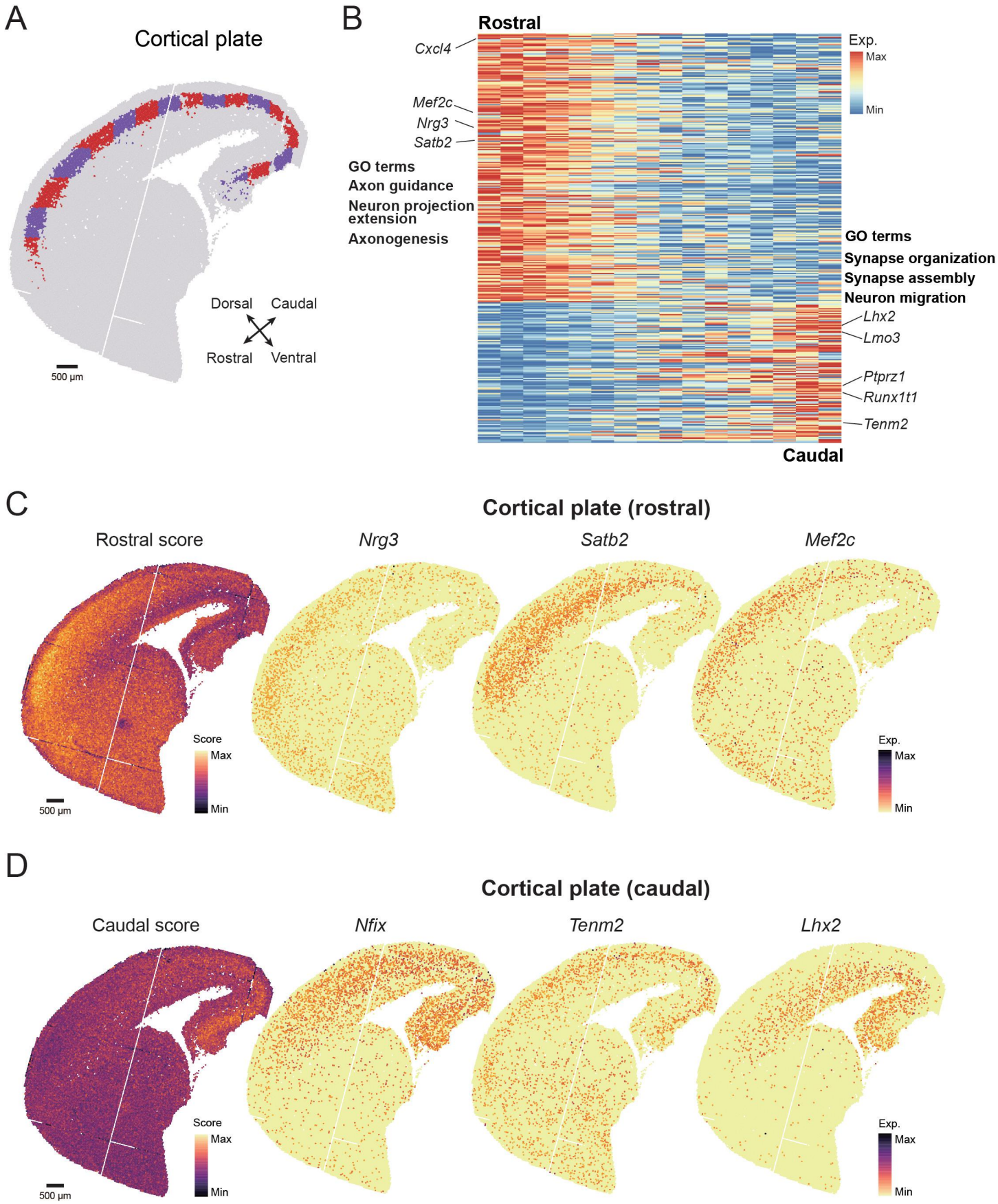
A
Cortical plate
Dorsal
Caudal
Rostral
Ventral
500 µm
B
Rostral
Cxcl4
Mef2c
Nrg3
Satb2
GO terms
Axon guidance
Neuron projection extension
Axonogenesis
Exp.
Max
Min
GO terms
Synapse organization
Synapse assembly
Neuron migration
Lhx2
Lmo3
Ptprz1
Runx1t1
Tenm2
Caudal
C
Cortical plate (rostral)
Rostral score
Nrg3
Satb2
Mef2c
Score
Max
Min
Exp.
Max
Min
500 µm
D
Cortical plate (caudal)
Caudal score
Nfix
Tenm2
Lhx2
Score
Max
Min
Exp.
Max
Min
500 µm

Figure S25

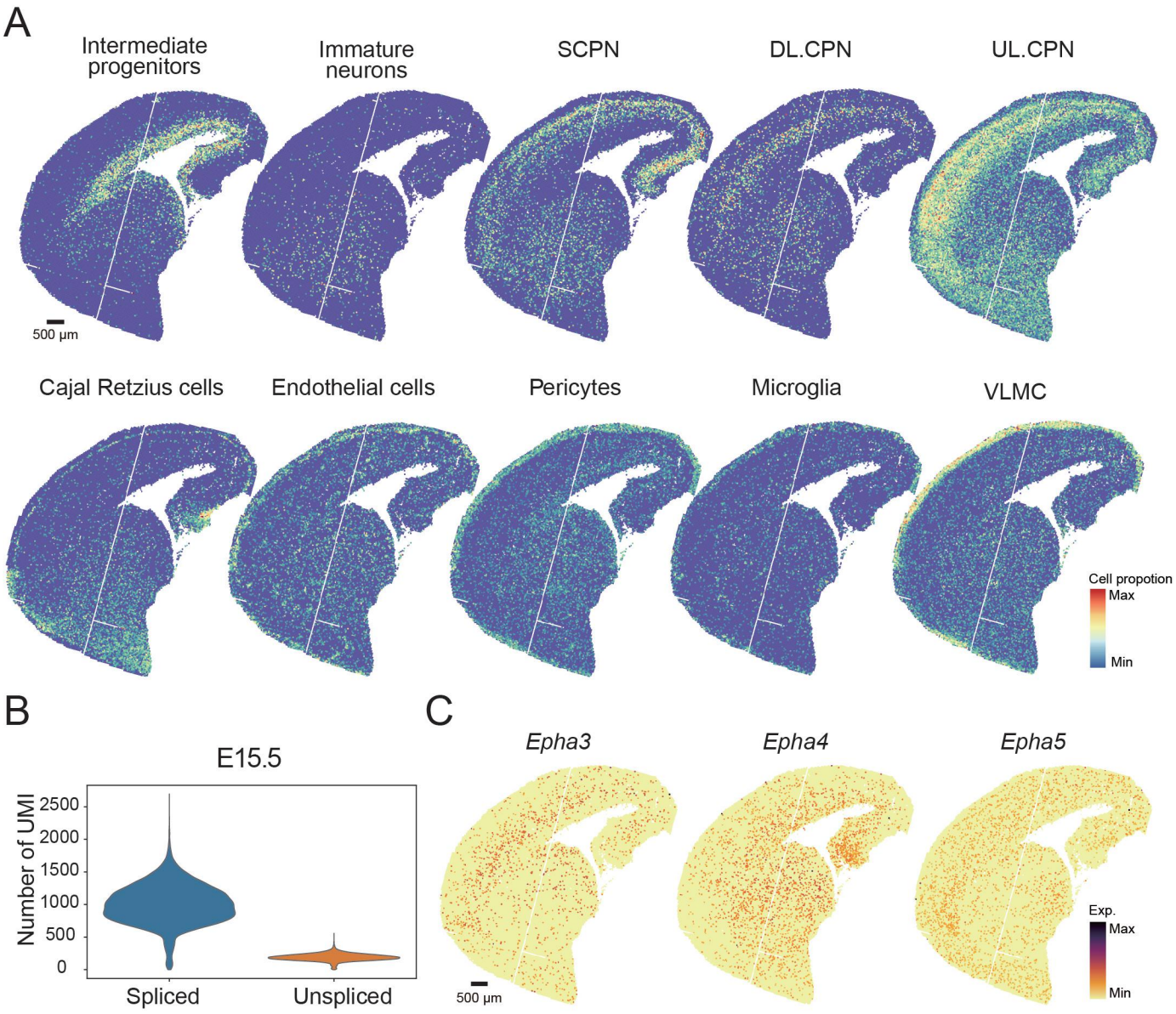
A
Intermediate progenitors
Immature neurons
SCPN
DL.CPN
UL.CPN
500 µm
Cajal Retzius cells
Endothelial cells
Pericytes
Microglia
VLMC
Cell propotion
Max
Min
B
E15.5
Number of UMI
2500
2000
1500
1000
500
0
Spliced
Unspliced
C
Epha3
Epha4
Epha5
500 µm
Exp.
Max
Min

Figure S26

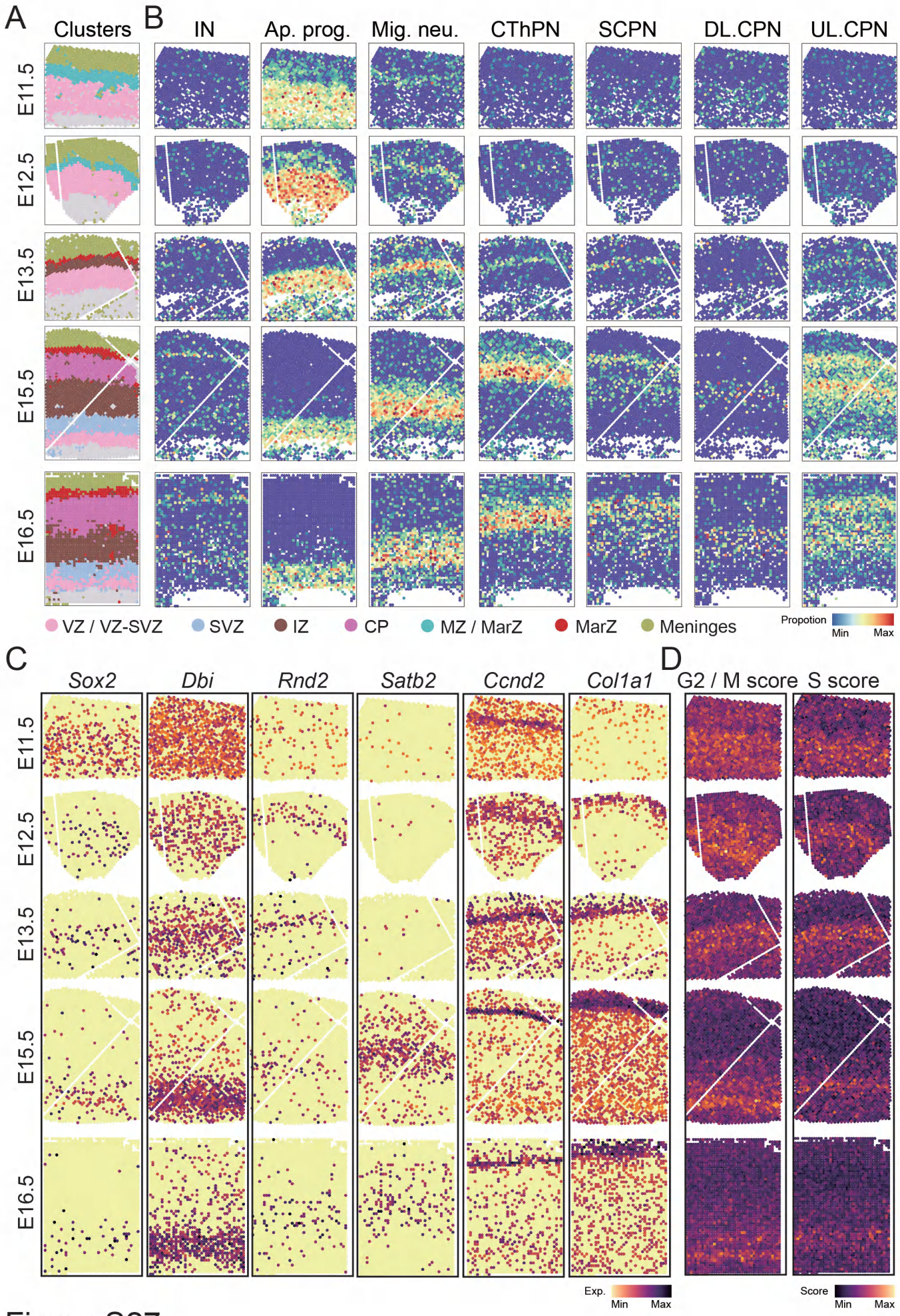
A
Clusters
B
IN
Ap. prog.
Mig. neu.
CThPN
SCPN
DL.CPN
UL.CPN
E11.5
E12.5
E13.5
E15.5
E16.5
VZ / VZ-SVZ
SVZ
IZ
CP
MZ / MarZ
MarZ
Meninges
Propotion
Min
Max
C
Sox2
Dbi
Rnd2
Satb2
Ccnd2
Col1a1
D
G2 / M score
S score
Exp.
Min
Max
Score
Min
Max

Figure S27

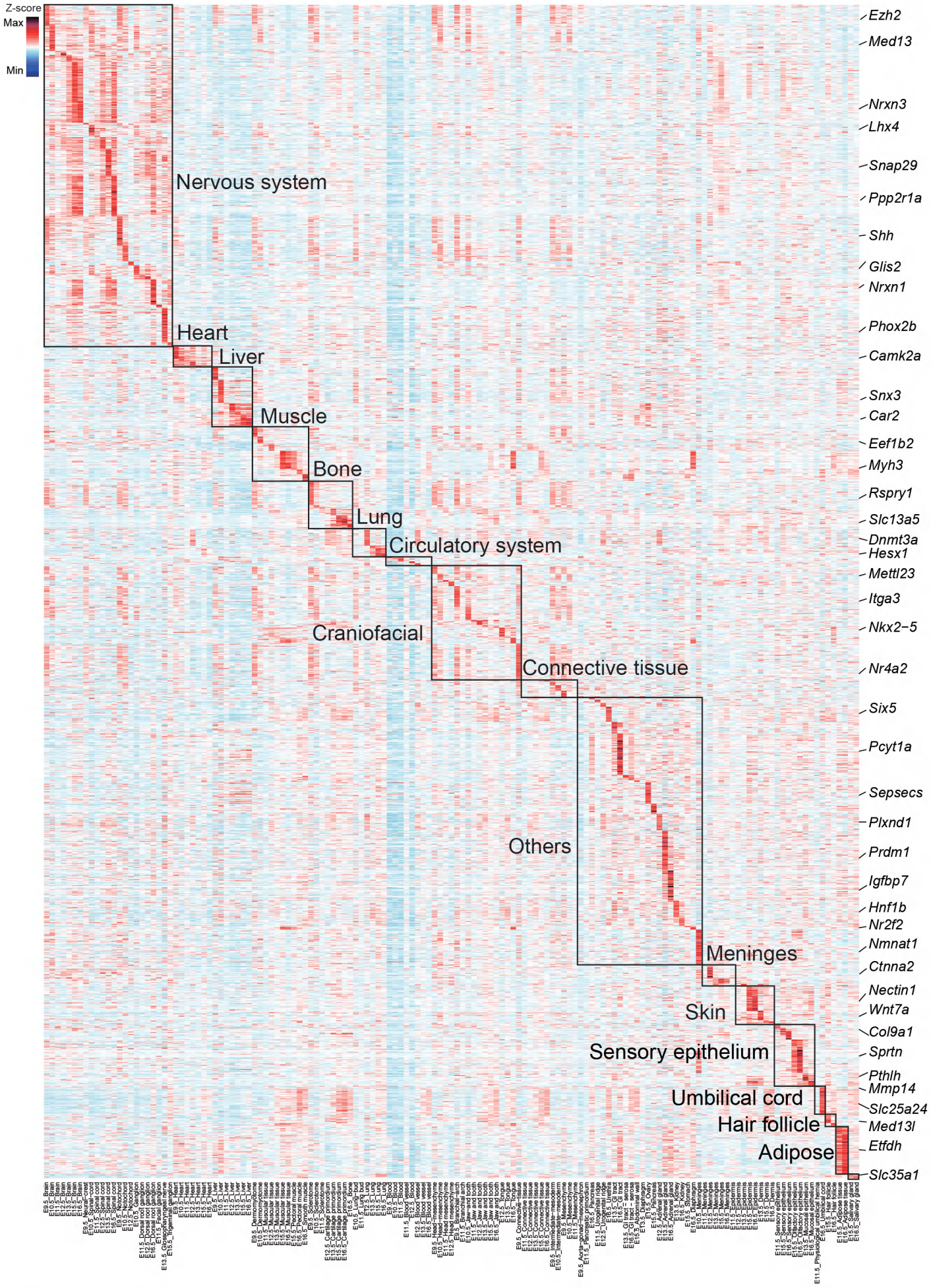
Z-score
Max
Min
Nervous system
Heart
Liver
Muscle
Bone
Lung
Circulatory system
Craniofacial
Connective tissue
Others
Meninges
Skin
Sensory epithelium
Umbilical cord
Hair follicle
Adipose
Ezh2
Med13
Nrxn3
Lhx4
Snap29
Ppp2r1a
Shh
Glis2
Nrxn1
Phox2b
Camk2a
Snx3
Car2
Eef1b2
Myh3
Rspry1
Slc13a5
Dnmt3a
Hesx1
Mettl23
Itga3
Nkx2−5
Nr4a2
Six5
Pcyt1a
Sepsecs
Plxnd1
Prdm1
Igfbp7
Hnf1b
Nr2f2
Nmnat1
Ctnna2
Nectin1
Wnt7a
Col9a1
Sprtn
Pthlh
Mmp14
Slc25a24
Med13l
Etfdh
Slc35a1

Figure S28